DESIGN OF STRUCTURAL VIBRATION CONTROL USING SMART MATERIALS AND DEVICES FOR EARTHQUAKE-RESISTANT AND RESILIENT BUILDINGS

A Thesis
Submitted to the Graduate Faculty
of the
North Dakota State University
of Agriculture and Applied Science

By

Mohsen Azimi

In Partial Fulfillment of the Requirements
for the Degree of
MASTER OF SCIENCE

Major Department:
Civil and Environmental Engineering

May 2017

Fargo, North Dakota

North Dakota State University
Graduate School

Title

DESIGN OF STRUCTURAL VIBRATION CONTROL USING SMART MATERIALS AND DEVICES FOR EARTHQUAKE-RESISTANT AND RESILIENT BUILDINGS

By

Mohsen Azimi

The Supervisory Committee certifies that this ***disquisition*** complies with North Dakota State University's regulations and meets the accepted standards for the degree of

MASTER OF SCIENCE

SUPERVISORY COMMITTEE:

Dr. Zhibin Lin
Chair

Dr. Mijia Yang

Dr. Annie Tangpong

Approved:

9/21/2017
Date

Xuefeng Chu
Department Chair

ABSTRACT

Major earthquakes in recent years have highlighted the big concern of modern seismic design concept for the resilience of buildings. The overall goals of this thesis aim to design structural vibration control using smart materials and devices and to elucidate the factors determining their robustness, feasibility, and adaptability for earthquake-resistant and resilient buildings.

The study mainly includes a) integrated wavelet-based vibration control with damage detection; b) shape memory alloy to eliminate the residual deformations; c) a mass damper for highly irregular tall buildings; and d) soil-structure interaction effects on the buildings. The robustness, feasibility, and adaptability of these proposed studies for earthquake-resistant and resilient buildings are evaluated using various performance measures.

The findings of the study reveal that the structural vibration control strategies could advance the current-of-art knowledge in seismic risk mitigation as well as high system adaptability.

ACKNOWLEDGEMENTS

I would like to thank Dr. Zhibin Lin, Dr. Mijia Yang, Dr. Annie Tangpong, Dr. Fei Yan, and Hong Pan for their support during my studies.

DEDICATION

This work is dedicated to my family especially to my father, Ghader Azimi, and mother, Ghamar Kazemi. I also respectfully dedicate it to my dearest, Maral. Finally, it is as well dedicated to my advisor, my team members, and my professors who supported me during the program.

TABLE OF CONTENTS

LIST OF TABLES

LIST OF FIGURES

LIST OF ABBREVIATIONS

LRQ.....Linear Quadratic Regulator.

FLC .....Fuzzy Logic Control.

PSO .....Particle Swarm Optimization.

SMA.....Shape Memory Alloy.

LIST OF SYMBOLS

A .....State Matrix.

B .....State-space input matrix.

C.....Damping matrix.

G.....Gain matrix.

K.....Stiffness matrix.

M .....Mass matrix.

u.....Input vector.

V.....Velocity vector.

PI.....Performance index.

Q.....Weight matrix.

R.....Weight matrix.

Z .....State vector.

γ .....Damper location matrix.

1. INTRODUCTION

1.1. Overview

Civil infrastructures are mainly subjected to different types of loads that may generate severe vibration in structure. Great efforts have been made to build structures which can resist wind and earthquake loads. Since the 1970s, the application of smart structure technology has become attractive in order to enhance the reliability of structures to withstand seismic and wind loads. These new approaches save costs by implementing devices to retrofit existing structure and meet the safety and serviceability requirements. Nowadays this concept is practically applied to critical civil structures, such as hospitals, power plants, bridges, and tall buildings to provide safety and serviceability against potential extreme winds or earthquakes.

1.2. Basic principles for seismic response control

There are three basic methods to reduce dyanmic response of a structure: reducing the ground motion by shifting the primary frequencies, increasing damping in the structure, or avoiding resonance state. By using base-isolation systems, the energy and motion cannot transfer to the structure. Application of these systems are practical to some type of structures and therefore, control devices are developed to apply a control force, to utilize the energy absorption, or to avoid resonance.

For seismic response control of systems, adding damping to a large-scale structure is more practical than changing mass and stiffness. Numerous force-generating devices are required to generate the restoring force, but with much less effort, a control system can add damping to the system. Passive control systems employ passive energy dissipation devices, to produce the control force. The properties of these devices are not adjustable to the environmental changes and therefore they are less adaptable to different load patterns.

Emerging passive damping systems to suppress the vibration of structures have a long history, and they were used in automobiles, aircraft, and civil engineering industries. Semi-active systems are also less adaptive, compared to active systems, because of its passive base which limits generating force. However, both semi-active and hybrid systems utilize advantages and avoid disadvantages of active and passive systems, and therefore are popular and more researches are currently undergoing to develop and implement this type of systems in real-scale structures.

Developing the control devices to large-scale structures is a challenging task, and it is the main reason that the modern technology for controlling vibrations in mechanical engineering industry is mature. Along with the developments in theoretical researches, numerous practical application of control systems has been used in civil structures [1] to mitigate the response of structure against wind and earthquake loads.

Studies on structural control basically focus on these topics: modeling the control systems and developing the algorithms, developing the controlling devices, application of smart materials, reliability of methods, full-scale implementation, and finally developing design specifications. The primary objective of motion based design approach is the satisfaction of motion instead of strength. Along with developing knowledge and technology, the structural motion control is an emerging discipline with a broad application. To obtain both economic and sustainable design, the optimal design should satisfy the motion and strength limits. This goal can be achieved by means of smart material and devices. The main loads in every building are dead loads and lateral dynamic wind or earthquake loads. Both Earthquake and wind can be dominant according to the site and the building configuration. For example, for a steel building higher than 100 m, in a seismic region, the wind load can be dominant.

1.3. Objectives

The main objectives of this study can be summarized as:

- Exploring an integrated technique for damage detection with semi-active control for base-isolated buildings.
- Using shape memory alloys to eliminate the residual deformations of base-isolators.
- Exploring a tuned mass damper system to reduce the torsional vibration of tall and irregular buildings.
- Investigating the performance of semi-actively controlled irregular multi-story building using multiple MR dampers and considering the soil-structure effects.

1.4. Thesis organization

The thesis is organized in 9 chapters. Chapter 2 is the literature review, and it discusses the current challenges with the seismic vibration control of structures. Two types of structures are also addressed in this thesis, base-isolated and irregular multi-story buildings. Chapter 3 presents the methods that are used in this study to control structures. In chapter 4, basic steps for dynamic structures with controllers are demonstrated and performance metrics are used for assessment. In chapter 5 and 6, base-isolated buildings are investigated. In chapter 5, a damage detection method with semi-active control is explored using MR damper in the base level. The residual deformations of the base-isolators are reduced using shape memory alloys (SMAs) in chapter 6. Exploration of tuned mass damper systems are carried out for highly irregular buildings in chapter 7, and the performance of semi-actively controlled high-rise irregular buildings is studied in chapter 8 with considering soil-structure interaction. The summary and conclusion of the study is presented in the end of the thesis in chapter 9.

2. LITERATURE REVIEW

2.1. Introduction

Buildings are vulnerable to severe vibration when subjected to extreme hazard events, such as earthquakes and winds. A typical building design is to prevent collapse in terms of expected deformation demands to structural components in the event of earthquakes [2]. Practicing engineers have long recognized that structural response of buildings to strong ground motion due to earthquakes or other extreme events frequently results in inelastic behavior [3]. There is, however, very limited and small inherent damping of conventional building materials and structural components to allow dissipating such considerable dynamic energy [4]. As a result, the buildings usually have to behave with substantial damage and possibly permanent deformation. Currently major earthquakes, such as Sichuan earthquake in China (2008), Christchurch earthquake in New Zealand (2011), Chile earthquake (2010) and Great Sendai earthquake in Japan (2011) confirm this big concern of modern seismic design concept for resilience of buildings and bridges [5-10].

Research on innovative designs and materials for new and existing buildings has demonstrated their enhanced seismic performance [11, 12]. These design approaches mainly include: a) using base isolation concepts or devices to control and reduce the demand [13, 14], b) using shape memory alloy (SMA) [15, 16], expansion concrete [17] or post-tensioning active confinement [18] to minimize or eliminate permanent deformation, and c) using jacketing [19] through passive confinement to increase ductility capacity. Considering that in performance-based engineering, it is required that a building structure achieves multiple performance levels under small, moderate, and strong earthquakes [20], these methods and techniques, however,

cannot provide sufficient adaptability and may even lead to uneconomic design in order to accommodate different performance levels [21, 22].

2.2. Semi-active control system

Alternatively, increasing efforts in recent years have been directed to the development and implementation of control systems for higher seismic performance and enhanced resilience of buildings [23]. A control system usually refers to control algorithms (e.g., active control, semi-active control, hybrid control, and passive control [24]) and the corresponding controlling devices (e.g., semi-control hydraulic dampers, active-control piezoelectric actuators [25]). Among various control algorithms, semi-active control systems exhibit their attractive characteristics, including less power, higher reliability, and particularly higher adaptability for earthquake events, as compared to their counterparts [26, 27]. As a result, semi-active control systems and the associated devices have played an important role in structural vibration controls and mitigations.

The full-scale semi-active control system was first implemented to the Kajima Shizuoka Building in 1998, in Shizuoka, Japan [28]. Two semi-active hydraulic dampers were installed at the 1st to 4th stories, while linear quadratic regulator (LQR) was used as a controlling algorithm to adjust damping forces. After that, there are many cases worldwide with a high variety in use of semi-active control systems and hydraulic dampers [29, 30]. Kurino et al. [31] studied semi-active and passive control systems with dampers under different levels of earthquakes. The dampers in their systems were controlled by the Maxwell's model to allow generating two maximum and minimum damping forces for accommodating different levels of seismic response. In this method, the damper can be adjusted to either its high or low state damping, that may use simpler algorithms, but does not generate continuous damping. Note that semi-active hydraulic

damper systems in those studies were mainly driven by on-off bi-mode to switch valves for controlling damping forces to structures [32].

Other researchers [33] applied optimization techniques into their studies to achieve reduction in maximum response with minimum cost. Cundumi and Suárez [33] proposed a variable semi-active damping device, consisting of two fixed-orifice viscous fluid dampers. The developed damper was mounted to the frame by one end while the other side was a moving end along a connected collar. The position of the moving end was driven using an actuator with a modified LQR algorithm, by which a performance index in the state vector was minimized to control the structural vibration. Similarly, Kazemi Bidokhti et al. [34] investigated seismic performance of three- and ten-story buildings strengthened by semi-active hydraulic dampers on their V-bracing members. The genetic algorithm was selected in their study for optimizing the dampers, in which the input parameters were displacement, velocity and acceleration of each story, and the output was the damping required for the devices. Their results revealed that the proposed control system was efficient in seismic risk mitigation by considerable reduction in structural displacements, velocities and accelerations. One challenge of such controlling algorithm in its actual implementation, however, was computational capability and time consumption for data processing and optimization of the input variables and yielding damping coefficients instantaneously. Shih et al. [35] have recently proposed a semi-active hydraulic damper as an active interaction control device. The dampers in their study were placed between story levels and the substructure was simulated as a single degree of freedom system with damping and stiffness. These dampers and algorithms are still under development and are gaining more attention because of their superior compatible characteristics [36, 37].

2.3. Tuned mass dampers (TMDs)

Passive energy dissipation systems dissipate a portion of the imposed energy, and mitigate the structural response, and therefore, increase the safety, by means of mechanical devices [39-41]. Examples of such systems include tuned mass dampers (TMDs), tuned liquid dampers (TLDs), friction dampers, viscous-elastic dampers, and viscous fluid dampers. These systems do not require an external power source, sensors, or computation center. The main reason for using these systems is introducing larger damping.

Passive tuned mass dampers (TMD) is one of the attractive mass vibration absorbers for reducing the structural responses that consists of a mass, spring, and a dashpot. TMDs have been employed in a large number of structures around the word [42]. TMDs counteract the movement of the floor when they are stretched or compressed. Although TMDs are theoretically high-performance devices, application of passive TMD systems are limited to the narrow frequency band and need to be tuned according to the main structure. Therefore, they cannot be effective for such structures with closely spaced natural frequencies [43].

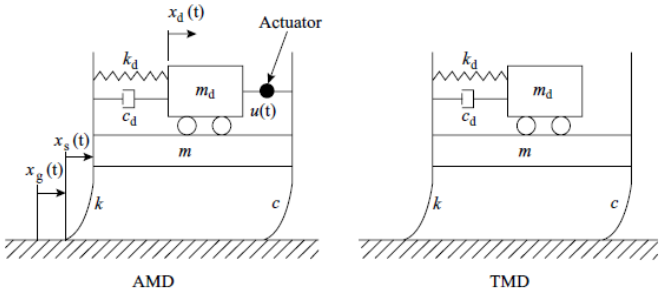

Figure 2-1. Active mass damper (AMD) and tuned mass damper (TMD) [12].

One of the variables in tuning a TMD is the mass ratio (μ), that is usually within the range of 1-10% [43]. Using the mass ration, μ, researchers used different optimal designs; the formulation for a classic TMD design is described by Den Hartog [44], which assumes that the natural frequency and mass of the controlled structure are known. However, the estimated

natural frequency and mass can differ from the real ones due to estimation errors. Those effects will result in a suboptimal TMD tuning or even a mistuning, and thereby a loss of damping in the controlled structure [45].

Active TMD and active mass driver (AMD) do not have the limitations of passive TMDs, however, they are highly unreliable since they rely on the external large power source, as well as, a good estimation of dynamic properties of the system [46]. A small error is processing the signals, may destabilize the structure during an earthquake [12]. These drawbacks are considerably solved by introducing semi-active TMDs (SATMD). SATMDs are adaptable during an earthquake; the most common types of SATMDs are those with adjustable damping or stiffness. Serval studies investigated the variation of damping of SATMD on the overall performance

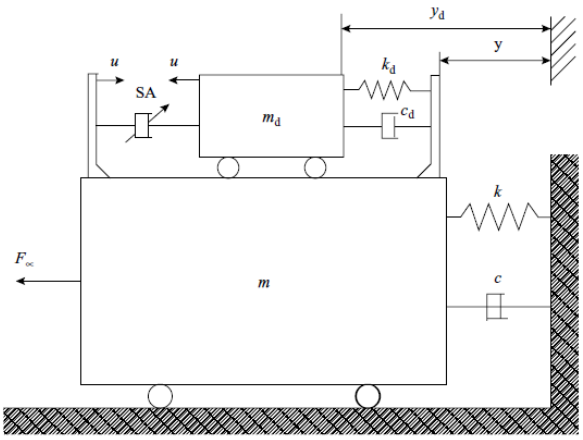

Figure 2-2. Semi-active TMD system [12].

MR damper and TMD have been combined to form both hybrid and semi-active control strategies. The conventional MR-TMD consists of mass, spring and MR damper, assembled to form a semi-active unit, not many studies exist on the subject. A new semi-active control device combining classic TMD and MR damper was proposed by Lin, et al. [47], it was observed that MR-TMD can improve the efficiency of TMD.

An experimental investigation on a cable vibration control using MR-TMD damper was conducted by Cai, et al. [48], the vibrations in the cable were absorbed by both the TMD component and the MR damper component and significant vibration reduction efficiency was achieved. Weber, et al. [49] presented a new adaptive TMD whose stiffness and damping can be tuned in real time to the controlled structure frequencies, and this can be achieved by replacing the traditional oil damper in the TMD by MR damper.

Kang, et al. [50] investigated the efficiency of MR-TMD for wind excitation mitigation on a 76 story benchmark building. The results show that the performance of MR-TMD is better than TMD for wind excitation control of a tall building. A new combination of MR damper and TMD was applied on bridge harmonic vibration control [51]. The results show that the proposed MR-TMD concept outperforms the TMD in all studied cases significantly. Kaveh, et al. [52] introduced an optimization algorithm to control an MR-TMD device to increase its performance. The results showed better performance of the optimized algorithm controller in reducing the structural vibration responses. Any of those systems need control algorithms that use the control devices optimally. Designing and developing an optimal and adaptive controller have remained as a big challenge for researchers.

2.4. Seismic base-isolation systems

The main purpose of seismic performance-based design of structures is to reduce the damage and injuries risks under earthquake dynamic loads. One of the effective and economic methods for achieving this goal is using seismic base-isolation devices as one of the reliable methods for protecting both structural and nonstructural components. Figure 2-1 shows different types of base-isolation systems that are popular in the seismic design of the building.

Main dynamic effects of base isolation on the super structure includes: (1) increasing the natural period of the structure, and (2) decreasing acceleration responses, as well as inter-story displacements. As the period of structure shifts, the displacement in the base level will also increases [1]; however, reducing the structural responses in superstructure can mitigate the structural and nonstructural damages. In the base-isolated structures, the fundamental frequency is reduced, and the first mode of vibration is considerably separated from the others; therefore, the superstructure can be reasonably assumed to remain linear, therefore the potential damages can be initiated from the base level.

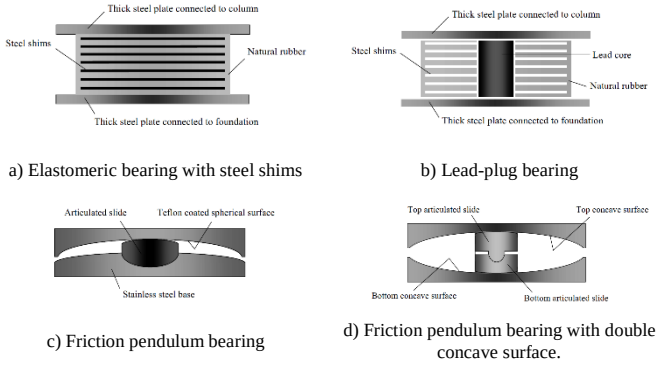

a) Elastomeric bearing with steel shims

b) Lead-plug bearing

c) Friction pendulum bearing

d) Friction pendulum bearing with double concave surface.

Figure 2-3. Different types of base-isolation systems [12].

Near-field earthquakes with long-duration pulse impose significant relative displacements in the base-isolations that may exceed beyond the design allowable displacement [53]. Designing base-isolated structure for near-field earthquakes may require larger base-isolators which increases cost of the construction, significantly, that is in contradiction with the aforementioned goals of seismic design of base-isolated structures. In addition, engineers have learned from the historic earthquakes, such as the 1994 Northridge, that a survived structure may have been collapsed if it was located elsewhere [54].

The Eigensystem realization algorithm (ERA) has been widely applied for model identification in civil engineering [55-58]. These algorithms also show great potential to damage

detection. Fraraccio [55] uses this method to analysis a base excited four-story steel frame model. The result shows that the ERA algorithm are robust against different input. Siringoringo [56] used Natural Excitation Technique (NExT) and ERA algorithm to locate and quantify the damage of double clamped bolted joint plate. The result shows a great identification performance which the Modal Assurance Coherence (MAC) are all big than 90%. Caicedo et al. [57] analysis the IASC-ASCE Benchmark modal use the NExT and ERA methods. Different damage sceneries show that it is difficult to detect a small stiffness lose which smaller than the modelling errors.

One method to alleviate the side effects of such design, is using hybrid systems of base-isolation with semi-active devices, such as magnetorheological (MR) dampers, that have been proposed by researchers [58, 91]. Since semi-active control devices do not input energy to the system and only absorb the energy with low power and great adaptability, in addition to fail-safe mechanism, they received significant attention compared to active and passive devices in the recent decades.

Any of those mentioned systems need practically viable control algorithms that utilize control devices with their full capacities and minimum energy cost. Since the nature of earthquakes are unknown, designing and developing an optimal and adaptive controller have been remained as a big challenge for researchers. For instance, an isolation system may be perfectly designed for near-field earthquakes, but may not perform very well for far-field earthquake, and vice versa.

Therefore, adaptive control algorithms can be more efficient when the dynamic parameters of a base-isolated structure or the ground motion characteristics change [21]. For the cases with less adaptability, because of uncertainties in seismic ground motion characteristics

and structural dynamic properties, it is necessary to study existence of damage in the isolation system and in the superstructure which the majority of the previous studies have not addressed this issue explicitly. While considerable efforts have been made to study system identification and damage detection [21, 22, 59], fewer studies have been conducted on vibration control of damaged structures [21, 59], particularly, vibration control of damaged structures by means of online damage detection techniques and using advanced intelligent algorithms [26, 101].

Based on the previous studies by Amini and his co-workers in the literature [26, 101], this study explores the control algorithm integrated with a damage detection technique in order to identify the damaged structure before an earthquake, and consider the cumulative damage in the base-isolation system. Identical to [26, 56, 57], the NExT and ERA methods are used for system identification purpose, and the accumulated damage of the base isolation system is considered along with the pre-earthquake damages as the input variables of the fuzzy logic controller (FLC). Then, the control force is determined by using the designed FLC for calculating the command voltage.

Adaptability of the proposed method was improved using wavelet transform which is a powerful tool to break down the earthquake signal into the basic functions that can be located both in time and frequency domains simultaneously [60, 61]. Therefore, the dominant frequency of ground motion was determined in time domain and compared to the primary natural frequency of the building to avoid resonance phenomena. The efficacy of the proposed method is studied for undamaged and damaged five-story base-isolated building that is augmented by a semi-active MR-damper at the base level. Nine performance indices, as well as dissipated energy are considered to compare the performance of each method under different earthquake excitations.

The major concern with the design of passive base-isolation systems is that the design parameters are not always optimized for different earthquake waves. Under near-field earthquakes, the displacement at the base level may exceed the allowable limits due to the intense long-period velocity pulses for such ground motions [53]. Rao and Jangid [62] related the large deformations of base-isolators to the normal component of near-field earthquakes, while Liao et al. [63] showed that higher PGV/PGA ratios result in larger displacements in isolated bridges. Shen et al. [64] experimentally observed the resonance phenomenon under near-field earthquakes by performing field tests. In another study, Jonsson et al. [65] studied the performance of base-isolated bridges with friction and lead rubber bearing isolators under near-field earthquakes, and noticed that the existing codes need to be reviewed for the internal forces in the members.

The current semi-active base-isolation systems are tuned by adjusting damping and stiffness. To overcome the drawbacks of passive base-isolators and to use the advantages of smart materials and control devices, researchers proposed the use of semi-active devices along with the passive base-isolator. For example, Lu et al. [66] carried out numerical and experimental studies on base-isolations with controllable stiffness using a semi-active actuator.

Over the past few years, many researchers turn their attention toward the application of shape memory alloys (SMAs) in seismic design problems, particularly in controlling earthquake-induced vibrations [16, 67]. SMA materials are mainly popular for their ability to regain their original shape upon unloading after undergoing large deformations, and for their hysteretic behavior and energy dissipation. In addition, SMAs are fatigue and corrosion resistant materials [16, 67-70]. These unique properties of the SMA materials are the results of the transformations

between the austenite to martensite states, which can be induced by changing the temperature (shape memory effect), or by changing the stress level (superelastic effect) [68].

Using the hybrid isolation system harnesses the high vertical load-carrying capacity and lateral flexibility of the laminated rubber bearings and additional energy dissipating and re-centering capability of SMAs [71]. Among various attempts of these hybrid isolation devices, natural and lead rubber bearings are mostly adopted for the SMA based isolation bearings. The majority of the studies in the literature investigated the performance of structures using SMA materials as passive devices, while few researchers studied the advantages of SMA materials in active and semi-active control systems [72].

Recently, number of attempts have been done to develop new base-isolation systems by taking the advantages of the superelastic effects of SMAs. For example, Ozbulut et al. [15] showed that superelastic friction base-isolators are very effective and feasible devices in reducing the seismic vibration responses. Dolce et al. [73] compared the performance of different isolation systems adopting rubber, steel and SMAs as the supplementary devices. Ozbulut and Hurlebaus [71] investigated the performance of the conventional flat sliding bearings assisted with the SMA device as an auxiliary to resist the earthquake forces. The hybrid isolation system displayed both re-centering and energy dissipation abilities due to the superelastic effect of SMAs providing excellent performance for the bridges against the near-field earthquakes.

In this study, a superelastic lead rubber bearing (S-LRB) base-isolation system is used for controlling seismic vibrations of a multi-story building by meaning of a semi-actively controlled MR damper. Two types of LRB devices are used along with the SMA devices that are simulated using a fuzzy based model. The performance of the designed system is numerically evaluated

with and without the effects of the semi-active MR damper under near-field earthquakes that are scaled based on the target spectrum for a region in San Diego, CA.

2.5. Irregular buildings and soil-structure interaction

The main purpose of seismic performance-based design of structures is to reduce the damage and injury risks under earthquake dynamic loads. For a controlled structure, the most common objective is to reduce the deformation as well as the acceleration response of the building which are directly related to the structural integrity and safety. One of the oldest method that has been applied to numerous practical designs, is using passive control devices. introducing supplemental passive damping devices, may decrease the response of structures, however with less flexibility for different circumstances.

Passive tuned mass dampers (TMD) is one of the attractive mass vibration absorbers for reducing the structural responses that consists of a mass, spring and a dashpot. TMDs have been employed in a large number of structures around the word [74]. TMDs counteract the movement of the floor when they are stretched or compressed. Although TMDs are theoretically high performance devices, application of passive TMD systems are limited to narrow frequency band and need to be tuned according to the main structure. Therefore, they cannot be effective for such structures with closely spaced natural frequencies [43].

One of the variables in tuning a TMD is the mass ration (μ), that is usually within the range of 1-10% [43]. Using the mass ration, μ, researchers used different optimal designs; the formulation for a classic TMD design is described by Den Hartog [44], which assumes that the natural frequency and mass of the controlled structure are known. However, the estimated natural frequency and mass can differ from the real ones due to estimation errors. Those effects

will result in a suboptimal TMD tuning or even a mistuning, and thereby a loss of damping in the controlled structure [45].

ATMD and active mass driver (AMD) do not have the limitations of passive TMDs, however, they are highly unreliable since they rely on external large power source, as well as, good estimation of dynamic properties of the system [46]. A small error is processing the signals, may destabilize the structure during an earthquake [12]. These drawbacks are considerably solved by introducing semi-active TMDs (SATMD). SATMDs are adaptable during an earthquake; the most common types of SATMDs are those with adjustable damping or stiffness. Serval studies investigated the variation of damping of SATMD on the overall performance

Any of those mentioned systems need practically viable control algorithms that utilize the control devices with their full adaptability and minimum energy cost. Since the nature of earthquakes are unknown, designing and developing an optimal and adaptive controller have been remained as a big challenge for researchers. This study introduces an optimum control procedure for irregular high-rise buildings equipped with MR-TMD system. Despite the majority of the mentioned researches, the torsional effect of TMD, dimensions, as well as the supporting springs in both directions were considered.

The effectiveness of the designed system has been evaluated for a ten-story irregular building under three historic earthquakes using fuzzy logic control (FLC). Displacement and velocity of the roof level are selected as the input variables of the FLC. Then, the control force is determined by using the designed FLC for calculating the command voltage.

The seismic provisions are revised frequently to meet the new standards, however, the traditional approaches including increasing the member sizes or the quality of materials do not guarantee the minimum damage due to the future unknown seismic events [4]. Thus, effective

techniques, such as intelligent vibration control, need to be continuously developed for protection of existing and new structures, particularly buildings with asymmetric designs [75].

In the field of structural dynamic and vibration control, the majority of studies in the literature investigated the performance of regular buildings under unidirectional seismic loads by means of simplified shear frame models for each direction. Consequently, the nature of buildings as well as seismic motions are neglected. Earthquakes have arbitrary directions that can usually described by two components [76], and such bidirectional earthquake loads cause simultaneous torsional-translational oscillations in the asymmetric buildings. Due to the translation-torsion coupled vibrations in structures with irregularity in plan and elevation, severe damage can be observed in the corner columns, which needs to be considered in the new dynamic models and the proposed formula for the optimized design parameters [42]. In addition, nonlinear behavior of the border members, such as bracing elements, needs to be evaluated for highly irregular buildings.

For the structures constructed on soft medium, the soil-structure interaction (SSI) effects can influence the dynamic properties of the superstructure (e.g., natural frequencies, damping, and mode shapes) [77]. Lin et al. [132] discussed the impacts of inclusion of SSI effects to seismic response of active-tendon controlled one-story irregular building. Farshidianfar and Soheili [133] carried out a research on passive vibration control of regular multistory buildings considering SSI effects. Nazarimofrad and Zahrai [115] further investigated the SSI effects on multi-story irregular buildings strengthened by active tendons.

Protecting structures against earthquakes by means of smart devices and smart controllers have been a rapidly growing area of interest in the recent decades. Different vibration suppression techniques have been developed along with the advances in the field of the modern

control systems to prevent structures from damage or collapse, which are usually categorized as: passive (e.g., shape memory alloys (SMA), TMDs), active (e.g., active tendons, ATMDs), semi-active (e.g., MR dampers), and hybrid control devices (e.g., hybrid base-isolations, hybrid mass dampers).

In order to properly use control devices to reduce the structural responses, controllers need to be designed appropriately to send the essential command signals. For structures under bidirectional loads, a controller prevents collapse of the structure by controlling the coupled translation-torsion responses [78, 79]. Among the several control algorithms that have been developed for structural vibration control (e.g., LQR [80], fuzzy logic control [81-83], PID, sliding mode control [84], and H∞ control [85]), the LQR and LQG controllers have gained significant importance since they can calculate the optimal control forces by minimizing an energy-based cost function. Yoshida et al. [86] experimentally studied the coupled translational and torsional vibration of a two-story building using semi-active MR dampers. Kim and Adeli [60] investigated hybrid control of 3D coupled steel high-rise buildings under seismic loads that suggests using LQR and LQG algorithms for feedback control.

For a multi-story building, reduction of coupled translation-torsion vibration requires the usage of multiple sensors and devices [87] that need to be placed in the best locations in order to effectively sense and control the structural vibrations. In a study by Chandiramani and Motra [88], multiple MR dampers have been used to control lateral-torsional response of buildings with asymmetric plan; similar approach was taken in this section, as well.

In this study, the performance of controlled irregular high-rise buildings is investigated using MR dampers and LQR controller. For this purpose, a ten-story building was numerically simulated and two pairs of MR dampers were installed on the selected levels to control

translational-torsional motion. Clipped-optimal control was used in order to determine the command voltages of each damper based on the obtained optimal force from the LQR algorithm. Further, effect of the measurement and the systems noise, the optimum placement of dampers, as well as the soil-structure interaction were investigated.

3. SMART MATERIALS, DEVICES, AND CONTROLLERS

3.1. Introduction

As stated, structural vibration mitigation of dynamic systems could be achieved by using smart materials or controllers. In this chapter, the brief information shown below include existing studies and the current state of knowledge in shape memory alloys, Magnetorheological dampers, and Linear quadratic regulator and fuzzy logic control.

3.2. Shape memory alloys (SMAs)

Shape memory alloy (SMA) materials generally exhibit two major crystal morphologies referred to the martensite and austenite [70], of which the former crystal structure maintains stable state under low temperatures and high stresses, while the latter one maintains stable state under high temperatures and low stresses. As it is well-known, the ordinary martensite phase transformation employs a way adopted in steel quenching and hardening, where the steel is heated up to a critical temperature for a certain period, and then cooled rapidly to be transformed into a martensitic structure, and this martensitic phase change is not reversible. Unlike steel materials, SMAs demonstrate the reversible phase transformations between the martensite and austenite phases, and martensite can display differently in the form of twinned or detwinned structures according to residual strain conditions [70-72].

Figure 3-1 displays the shape memory effect of SMAs, where the stress-strain curve aims to illustrate the deformation state, while the temperature-phase diagram aims to illustrate the necessary conditions for the occurrence of phase changing. The four temperatures for thermal cycling are denoted as the austenite start temperature (A_s), austenite finish temperature (A_f), martensite start temperature (M_s), and martensite finish temperature (M_f). The SMA transforms from twinned martensite to detwinned martensite under the loading conditions at a temperature

below M_f, then keeps the detwinned martensite after unloading. When the temperature is increased above A_f, SMA transforms to autenite phase, leading to a complete shape recovery. Thereafter, it can go back to the initial twinned martensite under a cooling treatment that the temperature is decreased below M_f.

Unlike shape memory effect that triggered by temperature, superelastic effect is motivated by stress, which is illustrated in Figure 3-1 Generally, the SMA behaves in the form of austenite phase initially at a temperature above A_f, and transforms to the detwinned martensite phase after loading. When the load is completely removed, it goes back to the initial state of austenite. The full recovery of deformation occurs during the loading cycling.

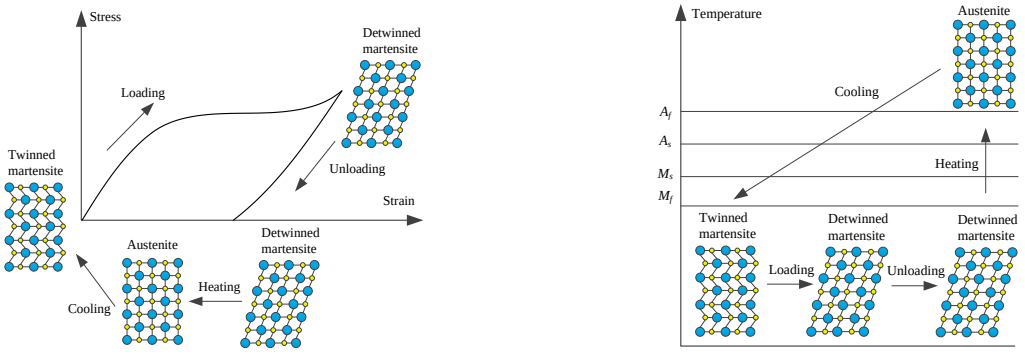

(a)

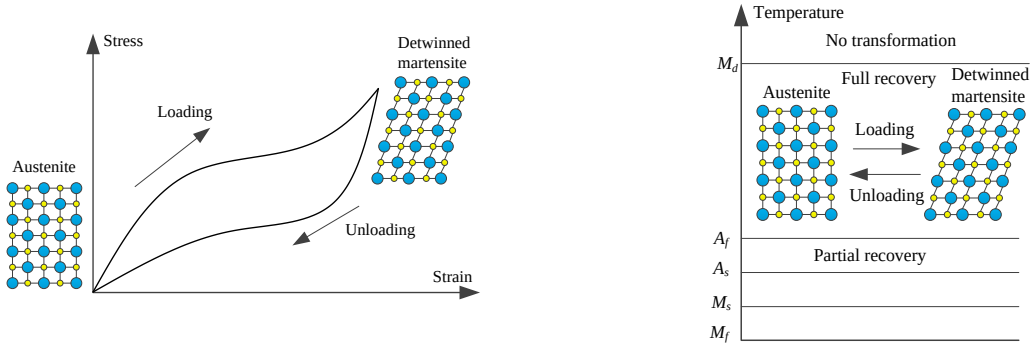

(b)

Figure 3-1. Shape memory effect (a) and superelastic effect (b) of SMAs [70].

The Nickels-titanium (NiTi)-based shape memory alloys [70] have gained the most attention among all types of SMA materials over the past several decades. One of the most

characteristic features of the NiTi-based alloys is that its completely recoverable strain can reach up to 8%, which provides tremendous potential for structural retrofits. The NiTi-based alloys adopt an approximate equiatomic compound of nickel and titanium, of which their respective atomic percentages can directly influence the phase transformation temperatures. Basically, the transformation temperature decreases as the atom content of nickel increases upon 50% and vice versa. Moreover, by adding the third element into the NiTi system, some other interesting properties can be induced accordingly. For example, the addition of Niobium (Nb) leads to a wider thermal hysteresis, displaying smaller response to the temperature changes.

3.3. Magnetorheological (MR) dampers

Nonlinear behavior of a single degree of freedom system was first describe by Bouc [89] in 1967 using a uniform adaptive model. Based on this model, Wen proposed an approximate procedure for solving random vibrations [90]. Bouc-Wen model has been widely used as a mathematical tool simulate the nonlinear behavior of civil and mechanical systems. By adjusting the unknown parameters in Bouc-Wen model, the actual nonlinear behavior of a nonlinear behavior of a system can be predicted. In 1997, the phenomenological model of the MR damper was introduced for the first time by spencer et al. [91] based on experimental studies on response of a prototype MR damper using Bouc-Wen model. The nonlinear force for an idealized model of MR damper can be calculated from Equation (3-1), as follows:

$$F = \alpha z + c_0 \dot{x} \tag{3-1}$$

where F, $\dot{x}$, c_0, and k_0 are the damper force, velocity, viscus damping at large velocities, and stiffness, respectively. z is an evolutionary variable for describing the hysteretic deformation of the MR damper, that is given as:

$$\dot{z} = -\gamma|\dot{x}|z|z|^{n-1} - \beta(\dot{x})|z|^n + A\dot{x} \tag{3-2}$$

where γ and β are the shape parameters, and A is related to the slope of the hysteretic loop, in which the smoothness of linear to nonlinear transition is governed by A. It is possible to adjust the parameters for a prototype MR damper and predict the force-displacement relationship before and after yielding.

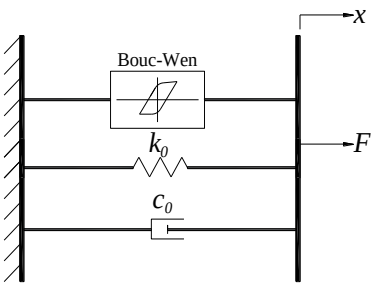

Figure 3-2. The simple Bouc-Wen model of an MR damper [44].

The voltage dependent model parameters are defined as a linear function of the efficient voltage, u [92]:

$$\alpha(u) = \alpha_a + \alpha_b u \tag{3-3}$$

$$c_0(u) = c_{0a} + c_{0b} u \tag{3-4}$$

The control voltage, v, is sent to the current driver and the efficient voltage, u, is then calculated through a first order filter that is used to account for the dynamics of rheological equilibrium of the MR fluid.

$$\dot{u} = -\eta(u - v) \tag{3-5}$$

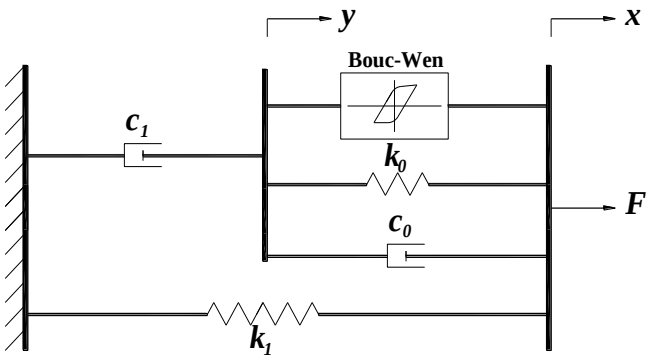

Figure 3-3. The modified Bouc-Wen model of MR damper [91].

Figure 3-3 shows the modified Bouc-Wen model of a MR damper. In this figure the nonlinear force of a MR damper, F, can be obtained using the following equations [91]:

$$F = c_1\dot{y} + k_1(x - x_0) \tag{3-6}$$

$$\dot{y} = \frac{1}{c_0 + c_1} + \left(\alpha z + c_0\dot{x} + k_0(x - y)\right) \tag{3-7}$$

where k_1 is the accumulator stiffness, z is the evolutionary variable to simulate the hysteretic deformation [91],

$$\dot{z} = -\gamma|\dot{x} - \dot{y}|z|z|^{n-1} - \beta(\dot{x} - \dot{y})|z|^n + A(\dot{x} - \dot{y}), \tag{3-8}$$

where γ and β are the shape parameters, and A is the parameter to describe the smoothness of linear to nonlinear transition. The voltage dependent parameters (i.e., α, c_0, and c_1) can be calculated using the following linear functions of the efficient voltage, u:

$$\alpha(u) = \alpha_a + \alpha_b u \tag{3-9}$$

$$c_0(u) = c_{0a} + c_{0b}u \tag{3-10}$$

$$c_1(u) = c_{1a} + c_{1b}u \tag{3-11}$$

The efficient voltage is determined using a first order filter as follows [91]:

$$\dot{u} = -\eta(u - v) \tag{3-12}$$

MR dampers are used in numerous numerical and experimental studies. Spence et al. showed that the Bouc-Wen model can predict the force-displacement of an MR damper prototype accurately, however it has less accuracy in low velocities for predicting force-displacement behavior [91]. It is important for a control strategy to adjust the applied voltage to the driver according to the measured desired control force. A trained neural network has been employed to predict required voltage of an optimal control in a study by Karamodin and Kazemi [93].

3.4. Linear quadratic regulator (LQR) and fuzzy logic control (FLC)

The full-scale semi-active control system was first implemented to the Kajima Shizuoka Building in 1998, in Shizuoka, Japan [36]. Two semi-active hydraulic dampers were installed at the 1st to 4th stories, while linear quadratic regulator (LQR) was used as a controlling algorithm to adjust damping forces. After that, there are many cases worldwide with a high variety in use of semi-active control systems and hydraulic dampers [35, 37, 94]. Kurino et al. [31] studied semi-active and passive control systems with dampers under different levels of earthquakes. The dampers in their systems were controlled by the Maxwell's model to allow generating two maximum and minimum damping forces for accommodating different levels of seismic response. In this method, the damper can be adjusted to either its high state or low state damping, which may use simpler algorithms, but does not generate continuous damping. Note that semi-active hydraulic damper systems in those studies were mainly driven by on-off bi-mode to switch valves for controlling damping forces to structures [32].

LQR control algorithm: In order to evaluate the effectiveness of a system, the LQR algorithm, which has been developed by Kurata et al. [28], can be used to compare the results with the uncontrolled system. LQR is widely used in optimum control techniques in structural control problems [66, 80, 95] that find active control parameters to minimize the cost function given by the form:

$$\mathrm{J} = \frac{1}{2}\int_{0}^{\infty} (\{z(t)\}^T[Q]\{z(t)\} + \{u(t)\}^T[R]\{u(t)\})\, dt \qquad (3\text{-}13)$$

Fuzzy logic control (FLC): Fuzzy logic control has been extensively used in structural vibration control to describe the complex mapping between a set of inputs and outputs [81, 82, 96]. In semi-active control using MR dampers, fuzzy controllers provide a command to adjust

the device variable parameters such as input voltage. Figure 3-4 shows the fuzzy control inference algorithm that basically consists of four main components: (1) the “rule-based” is set of rules that control the system. (2) The inference mechanism evaluates the control rules for the current time and decides what the output should be. (3) The fuzzification inference modifies the inputs; so they can be interpreted and compared to the rules in the knowledge base. (4) the defuzzification that converts the conclusions into the outputs.

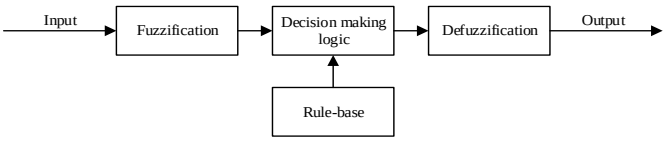

Figure 3-4. Fuzzy logic control inference block diagram.

4. DYNAMIC CONTROLLED SYSTEMS AND THEIR PERFORMANCE METRICS

4.1. Introduction

Much research has been conducted on structural control systems to improve the seismic performance of structures under earthquakes, and ultimately offer high performance resilient buildings beyond life risk mitigation. Among various structural control algorithms, semi-active control strategies have been widely accepted for overcoming some limitations existed in either passive or active control systems, thereby leading to better structural performance over their counterparts. In this study, we use dynamic systems with semi-active structural control to demonstrate the way for seismic risk mitigation and facilitation of the performance-based seismic design. Understanding of the basic steps and data process, from derivation of governing equations of controlled systems to performance metrics, will serve the reference of the following Chapters through this thesis.

4.2. Control system in buildings

4.2.1. Governing equations of building with semi-active control system

The dynamic governing equations of a building are usually described in matrix form [98] when subjected to a ground motion, $\ddot{x}_g$:

$$[\boldsymbol{M}]\{\ddot{x}(t)\} + [\boldsymbol{C}]\{\dot{x}(t)\} + [\boldsymbol{K}]\{x(t)\} = -[\boldsymbol{M}]\{\boldsymbol{E}\}\ddot{x}_g(t) \quad (4\text{-}1)$$

where, M, C and K are the mass, damping and stiffness matrices, and $\{x\}$, $\{\dot{x}\}$, $\{\ddot{x}\}$ are the nodal displacement, velocity and acceleration vectors, respectively. E is the influence factor which is a vector of all ones in this case, and n is the number of degrees of freedom. The Rayleigh method is used to get the damping matrix based on the mass and stiffness matrices [99]. An inherent damping of 2% is assumed for the first two modes of vibration.

Similarly, the dynamic governing equations of the building installed with a control system [98] are thus defined by a conventional dynamic system with a contribution of a controller:

$$[\boldsymbol{M}]\{\ddot{x}(t)\} + [\boldsymbol{C}]\{\dot{x}(t)\} + [\boldsymbol{K}]\{x(t)\} = [\boldsymbol{D}]\{u(t)\} - [\boldsymbol{M}]\{\boldsymbol{E}\}\ddot{x}_g(t) \tag{4-2}$$

where, {u(t)} is the controlling force vector; r is the number of the installed controllers, and D is the (n×r) matrix defined for the location of the controllers in the building [11, 12]; n and r are the number stories and number of dampers used, respectively.

$$\boldsymbol{D} = \begin{bmatrix} 1 & -1 & & & \\ & 1 & -1 & & \\ & & 1 & -1 & \\ & & & \ddots & \ddots \\ & & & & \ddots \end{bmatrix} \tag{4-3}$$

To solve the differential equation of motion in Equation (4-2), it is convenient to rewrite the governing equations in state-space form:

$$\{\ddot{x}(t)\} = -[\boldsymbol{M}]^{-1}[\boldsymbol{K}]\{x(t)\} - [\boldsymbol{M}]^{-1}[\boldsymbol{C}]\{\dot{x}(t)\} + [\boldsymbol{M}]^{-1}[\boldsymbol{D}]\{u(t)\} - \{\boldsymbol{E}\}\ddot{x}_g(t) \tag{4-4}$$

and the velocity vector, ẋ, is rewritten by

$$\{\dot{x}(t)\} = [\boldsymbol{I}]\{\dot{x}(t)\} \tag{4-5}$$

Thus, Equations (4-4) and (4-5) are expanded in a 2n×1 vector by

$$\begin{Bmatrix} \{\dot{x}(t)\} \\ \{\ddot{x}(t)\} \end{Bmatrix} = \begin{bmatrix} [\boldsymbol{0}] & [\boldsymbol{I}] \\ -[\boldsymbol{M}]^{-1}[\boldsymbol{K}] & -[\boldsymbol{M}]^{-1}[\boldsymbol{C}] \end{bmatrix} \begin{Bmatrix} \{x(t)\} \\ \{\dot{x}(t)\} \end{Bmatrix} + \begin{bmatrix} [\boldsymbol{0}] \\ [\boldsymbol{M}]^{-1}[\boldsymbol{D}] \end{bmatrix} \{u(t)\} + \begin{Bmatrix} \{\boldsymbol{0}\} \\ -\{\boldsymbol{E}\} \end{Bmatrix} \ddot{x}_g(t) \tag{4-6}$$

The second-order equation of motion for the system in Equation (4-2) is reduced in a first-order state-variable as:

$$\{\dot{z}(t)\} = [\boldsymbol{A}]\{z(t)\} + [\boldsymbol{B}]\{u(t)\} + \{\boldsymbol{H}\}\ddot{x}_g \tag{4-7}$$

where, $\{z(t)\}$ is the (2n×1) state-vector and the matrices, A, B and H, are defined below.

$$\{z(t)\} = \begin{Bmatrix} x(t) \\ \dot{x}(t) \end{Bmatrix} \tag{4-8}$$

$$\boldsymbol{A} = \begin{bmatrix} \boldsymbol{0} & \boldsymbol{I} \\ -\boldsymbol{M}^{-1}\boldsymbol{K} & -\boldsymbol{M}^{-1}\boldsymbol{C} \end{bmatrix};\ \boldsymbol{B} = \begin{bmatrix} \boldsymbol{0} \\ \boldsymbol{M}^{-1}\boldsymbol{D} \end{bmatrix};\ \boldsymbol{H} = \begin{bmatrix} \boldsymbol{0} \\ -\{\boldsymbol{E}\} \end{bmatrix} \tag{4-9}$$

Thus the solutions of this first-order differential state-space equation are determined based on numerical methods developed in the literature [12].

4.2.2. The LQR control algorithm

To determine the controlling force, semi-active system with the LQR algorithm, which has been developed by Kurata et al. [28], was used in the whole system. LQR is widely used in optimum control techniques in structural control problems [91, 95, 100] that finds an active control parameters to minimize the cost function given by the form:

$$J = \frac{1}{2}\int_0^\infty (\{z(t)\}^T[\boldsymbol{Q}]\{z(t)\} + \{u(t)\}^T[\boldsymbol{R}]\{u(t)\})\,dt \tag{4-10}$$

The weighting matrices for the semi-active LQR method, Q and R, are chosen as:

$$\boldsymbol{Q} = \begin{bmatrix} \boldsymbol{I}_{n\times n} & \boldsymbol{O} \\ \boldsymbol{O} & \boldsymbol{I}_{n\times n} \end{bmatrix} \times Q_n, \quad \boldsymbol{R} = [\boldsymbol{I}_{r\times r}] \times R_n \tag{4-11}$$

where, n and r are the number of stories and controllers. Q_n and R_n are the coefficients that are selected using optimization procedure in order to get the maximum reduction in the responses. For example, these two parameters, Q_n and R_n, are given in a vector form, in which the rows represent the one-story, five-story, and ten-story buildings used in numerical examples, respectively.

$$Q_n = \begin{bmatrix} Q_{n=1} \\ Q_{n=5} \\ Q_{n=10} \end{bmatrix} = \begin{bmatrix} 4.0 \\ 2.4 \\ 4.0 \end{bmatrix} \times 10^7, \quad R_n = \begin{bmatrix} R_{n=1} \\ R_{n=5} \\ R_{n=10} \end{bmatrix} = \begin{bmatrix} 0.0002 \\ 0.03 \\ 3.5 \end{bmatrix} \times 10^{-6} \tag{4-12}$$

Thus, the optimal control force vector at each step is

$$\{u_{opt}(t)\} = -[\boldsymbol{G}] \times \{z(t)\} \tag{4-13}$$

where the control gain matrix is defined by

$$[\boldsymbol{G}] = [\boldsymbol{R}]^{-1}[\boldsymbol{B}]^T[\boldsymbol{P}] \tag{4-14}$$

in which P is the Riccati matrix and $\{z(t)\}$ is the state feedback vector.

4.3. Performance metrics for assessment of controlled systems

To determine the effectiveness and robustness of different control systems for structural dynamics, performance metrics of dynamic controlled structures have been studies in the literature, including peak response, performance index, and energy of control.

4.3.1. Peak response

It is well known that maximum drift and maximum acceleration of stories are usually used to qualitatively and quantitatively assess performance of buildings with and without controller during the earthquakes.

4.3.2. Performance index

Reduction of the acceleration and the drift in a building during an excitation makes the residents feel comfortable and increases the safety of the structure. A scalar quantity, known as performance index (PI), was used to compare the performance of the different control systems. This approach has been used in [97] and [59]. To reflect the effects of either maximum drift or peak absolute acceleration response in the performance index, three indices, PI_t, PI_a, and PI_d, are defined by the form.

$$PI_t = w_a PI_a + w_d PI_d \tag{4-15}$$

$$PI_a = \frac{1}{n}\sum_{i=1}^{n}\left(\frac{a_{max,i}}{a_{un,i}}\right) \tag{4-16}$$

$$PI_d = \frac{1}{n}\sum_{i=1}^{n}\left(\frac{d_{max,i}}{d_{un,i}}\right) \tag{4-17}$$

where, PI_a, and PI_d represent the performance indices in terms of impacts of the maximum drift and peak absolute acceleration responses, respectively; PI_t is to account for the combined effects of both the maximum drift and peak absolute acceleration responses. For a specific system, a smaller value of these indices implies a better performance and more reduction in structural

responses. n is the number of stories; i represents the degree of freedom; d_{max} and dun are the maximum displacements corresponding to the i^{th} degree of freedom for controlled and uncontrolled systems, respectively. Similarly, the parameters, a_{max} and a_{un}, are the peak absolute accelerations obtained from controlled and uncontrolled systems, respectively. The parameters, w_a and w_d, are weighting coefficients for acceleration and displacement.

4.3.3. Energy of control force

In order to help understand the favorable features of the proposed method over the LQR method, energy of control is defined and used in this section, as well as the time-history of displacement and control force. Optimal control methods such as the LQR try to minimize the energy of the control through minimizing cost function in Equation (4-10). Energy of control is defined as:

$$E_c(t) = \int_0^t F_d \dot{u} dt \tag{4-18}$$

where $E_c(t)$ is the energy of control, and F_d and $\dot{u}$ are the damper force and velocity, respectively [80].

4.4. Numerical simulation of dynamic structures with controller

Three different multistory buildings were selected in the literature to demonstrate the performance of dynamic structures with LQR control algorithm for vibration mitigation. Different performance metrics in terms of peak response, performance index and energy of control force, were used to assess the effectiveness of control algorithms for dynamic structures.

4.4.1. Numerical examples

As illustrated in Fig. 4-1, three buildings with different stories varying from one to ten stories were selected to calibrate the effectiveness of the proposed control system with semi-active LQR controller for low-, mid-, and high-rise buildings, respectively.

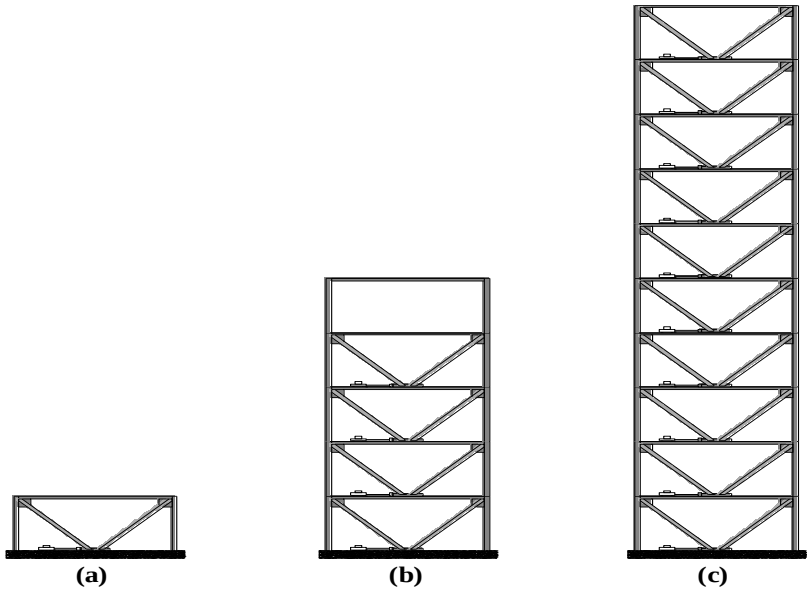

Figure 4-1. Three braced frame buildings with semi-active hydraulic dampers.

One-story building: this building was installed with a semi-active control system with a hydraulic damper as shown in Figure 4-1(a). This building was simulated as a single degree of freedom system with lumped mass at the floor level. Columns were modeled using equivalent springs. Mass, stiffness, and other properties of the frame, as well as damper parameters are given in Table 4-1.

Five-story building: An analytical model of the actual five-story building that has been studied by Kurata [28] was used in this study. This building is the first structure equipped with semi-active variable damping system. The height of the building is 19.75 m. This building was designed according to the Japanese building codes. In this building, for each of the first four floors, two dampers (8 dampers in total) were installed to the bracing members. These dampers were controlled by means of LQR algorithms. To control the structural vibration, sensors measure the response of the structure; then, a computer determines the damping force, and sends the results to the dampers to generate the required force. The analytical model of the North-South

frame of this building was created with semi-active hydraulic dampers as shown in Figure 4-1(b). In order to reduce the analysis time, floors were simplified with lumped masses, and other frame members were simulated using equivalent springs. Structural parameters of this building are given in Table 4-1.

Table 4-1. Structural properties of three buildings.

		Mass (kg)	**Stiffness w/out bracing (kN/mm)**	**Stiffness of bracing (kN/mm)**	**Stiffness of damper (kN/mm)**
One-story	1st	215200	31.24	1130	800
	5th	266100	84		
	4th	204800	89	1130	800
	3rd	207000	99	1130	800
	2nd	209200	113	1130	800
Five-story	1st	215200	147	876	800
	10th	230400	31.24	1130	800
	9th	230400	59.84	1130	800
	8th	230400	63.84	1130	800
	7th	230400	76.69	1130	800
	6th	230400	80.76	1130	800
	5th	230400	93.84	1130	800
	4th	230400	96.61	1130	800
	3rd	230400	97.80	1130	800
	2nd	230400	121.68	1130	800
Ten-story	1st	30960	162.36	1130	800

Ten-story building: In this building, similar to the previous models, the structure (Figure 4-1(c)) was considered as a shear frame, in which the floors were assumed more rigid as compared to the stiffness of the columns. Mass and stiffness properties of this model are given in Table 4-1.

Table 4-2. Characteristics of ground motion accelerations used in the analyses.

Earthquake	Date	Station	PGA
El Centro	1940/05/19	117 El Centro Array #9	0.32g
Northridge	1994/01/17	24087 Arleta – Nordhoff Fire Sta.	0.34g

Reference: PEER Ground Motion Database (http://ngawest2.berkeley.edu/).

4.4.2. Dynamic analysis and response of the buildings with control systems

The selected three buildings were installed with semi-active hydraulic dampers, while the assembly of the dynamic governing equations were presented in Equation (4-2). Semi-active control systems with the LQR was presented as well as passive control and uncontrolled ones for a comparison. Two representative earthquake ground motions were selected as the input variables to the buildings, as listed in Table 4-2. Note that selection of the ground motions is not the major objectives in this study and only two ground motions were chosen for simplicity to demonstrate the concept, although more various ground motions could be used to gain more information of structural response and characterize the corresponding control strategies.

Data outputs, particularly maximum drift and maximum acceleration of stories of the buildings during the earthquakes, were utilized as evaluation criteria, and reduction in these responses enables us to determine the performance of control systems [102]. Performance metrics of dynamic controlled structures are defined based on the literature, including performance index, energy of control, and noise interference, as presented in the following discussions.

4.5. Results and discussion

4.5.1. Effects of structural control on peak response

Maximum drift and maximum acceleration of stories of these three buildings during the earthquakes were plotted to demonstrate the effectiveness of the control systems, as illustrated in

Figure 4-2 through Figure 4-4, respectively. Figure 4-2 indicates that the max drift of the one-story building with passive devices exceeds that of the structure with other devices. The maximum drift of the controlled structure by SA-LQR control has 30% more reduction as compared with uncontronlled. From the peak absolute acceleration graph, the semi-active LQR system has the most reduction in the response by 56%. By comparing the control systems, both LQR and passive control system can effectively improve the response of the one-story building with respect to the uncontrolled structure.

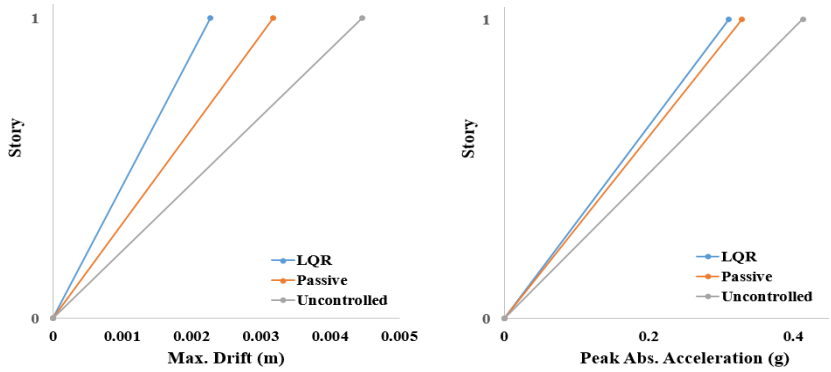

Figure 4-2. Peak response of the one-story building under El Centro earthquake.

As illustrated in Fig. 4-3, a significant reduction in responses in the five-story building can be obtained using the passive or LQR control system. Figure 4-3 and 4-4 indicate that with the controller, the LQR control system has similar effects to passive system with optimum damping in drift response reduction for the lower stories, and slightly difference in the top floors of the ten-story building. Similar conclusions could be drawn for the peak absolute acceleration reduction.

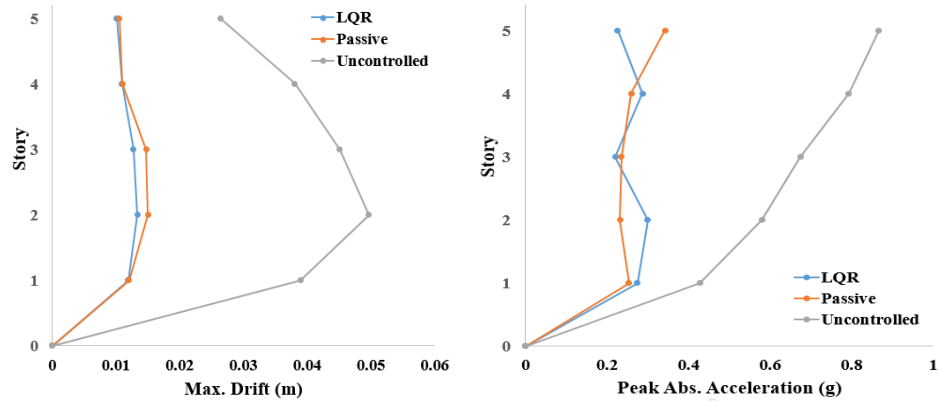

Figure 4-3. Peak response of the five-story building under El Centro earthquake.

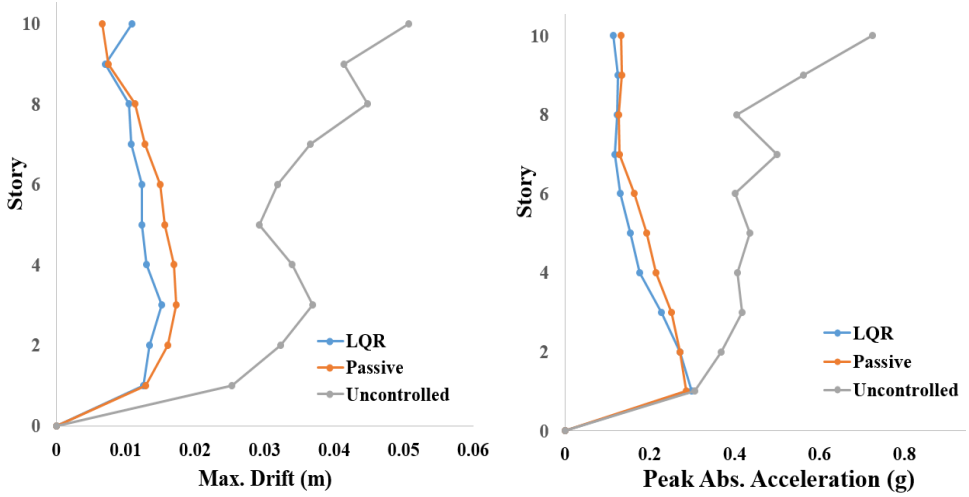

Figure 4-4. Peak response of the ten-story building under El Centro earthquake.

4.5.2. Assessment of structural control using performance index

To reflect the effects of either maximum drift or peak absolute acceleration response in the performance index, three indices, PI_t, PI_a, and PI_d, are defined in above section. The parameters, w_a and w_d, are weighting coefficients for acceleration and displacement, and they were selected equal to one in this study.

The PI_t for one-, five- and ten-story buildings with LQR control system under the El Centro earthquake, illustrated in Figure 4-5, are reduced by 11%, 12%, and 9% as compared to the passive control with the optimum damping. Similar trend is observed for the case under the Northridge earthquake.

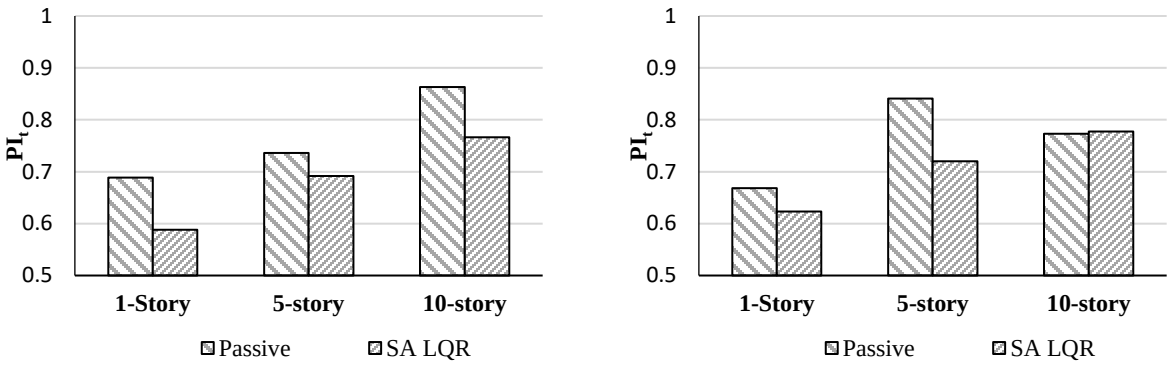

El Centro Northridge

Figure 4-5. Performance index PI_t of the buildings with passive, and semi-active LQR control.

To further investigate the performance of the proposed control method over other approaches under earthquakes with different magnitudes and peak ground acceleration (PGA), another sets of analysis have been carried out on the five-story building under six historical earthquakes that are commonly used as external excitation, as listed in Table 4-3. The control systems include a) passive control with optimum damping (P_{opt}), b) passive control with maximum damping (P_{Max}), and c) semi-active LQR (SA LQR). The results are presented in Figure 4-6.

Table 4-3. Characteristics of ground motion accelerations used in the analyses.

Earthquake	Station & Direction	Magnitude (Mw)	PGA (g)
1940 El Centro	El Centro Array #9 270°	7.2	0.21
1994 Northridge	Sylmar - Olive View Med FF 360°	6.7	0.84
1995 Kobe	H1170546.KOB 90°	7.2	0.63
1999 Chi-Chi	TCU068 N	7.6	0.36
1989 Loma Prieta	Hollister - South & Pine 0°	6.9	0.37
1971 San Fernando	Pacoima Dam 164°	6.6	1.22

Reference: PEER Ground Motion Database (http://ngawest2.berkeley.edu/).

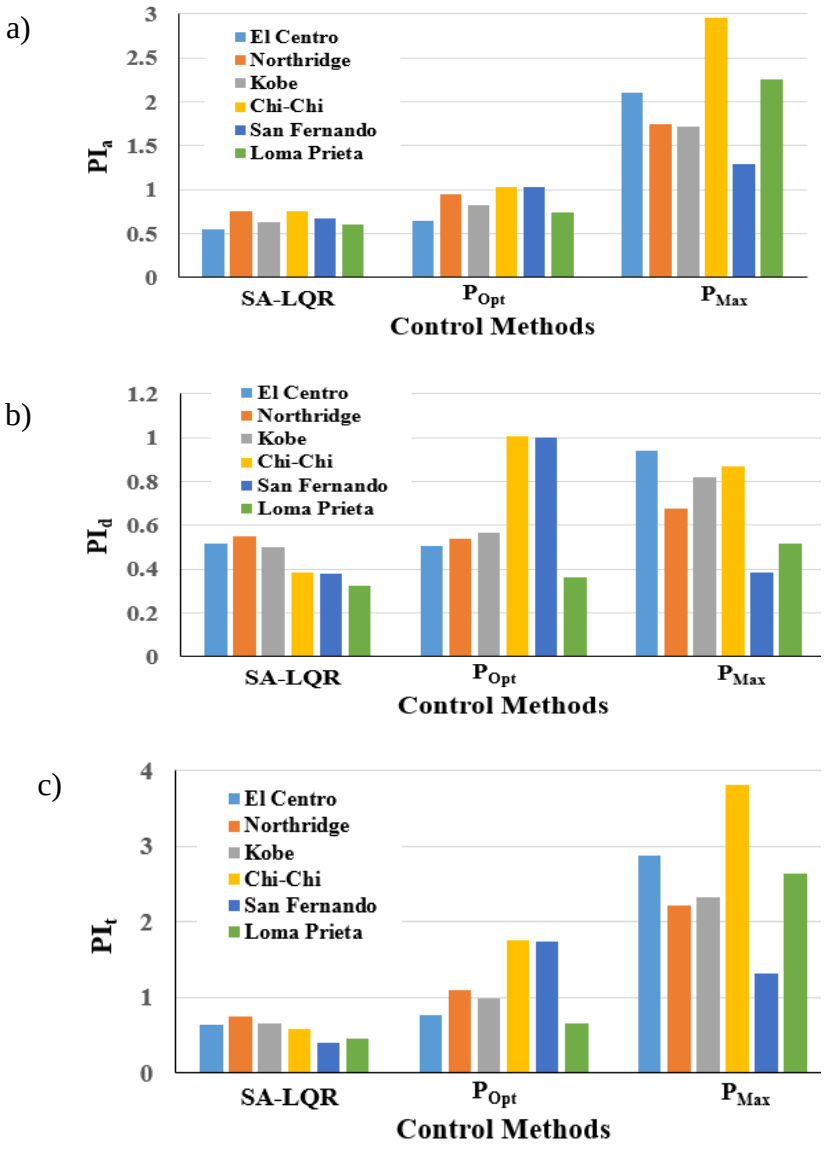

Figure 4-6. Performance indices of the five-story building under six historical earthquakes (a)-(c) curve.

Three performance indices in terms of the maximum drift, peak absolute acceleration or overall are plotted over six earthquakes. As clearly shown in Figure 4-(a)-(c), the SA-LQR controllers has better performance in terms of reducing the peak absolute acceleration in the story level under the all six earthquakes as compared to both passive controls. Two passive systems have different performances under different ground excitations. Clearly, the passive control with maximum damping, due to less adaptive capacity, cannot effectively reduce seismic

response at most earthquake scenarios, particularly less effective to mitigation of peak absolute acceleration responses. Even though the optimally designed passive system considerably reduces the drift and acceleration under the El Centro, Northridge, and Kobe earthquakes, for the Chi-Chi, San Fernando, and Loma Prieta earthquakes, it is not as effective as SA-LQR in reducing the drift response.

4.5.3. Assessment of structural control using energy of control force

Figure 4-(a)-(c) plot the time-history of displacement, control force and energy of control at the top floor of the ten-story building under the El-Centro earthquake, respectively. The consumed energy using the LQR controller is presented in Figure 4-(c). It can be envisioned that use of consumed energy is capable of assessing the effectiveness of the different controllers.

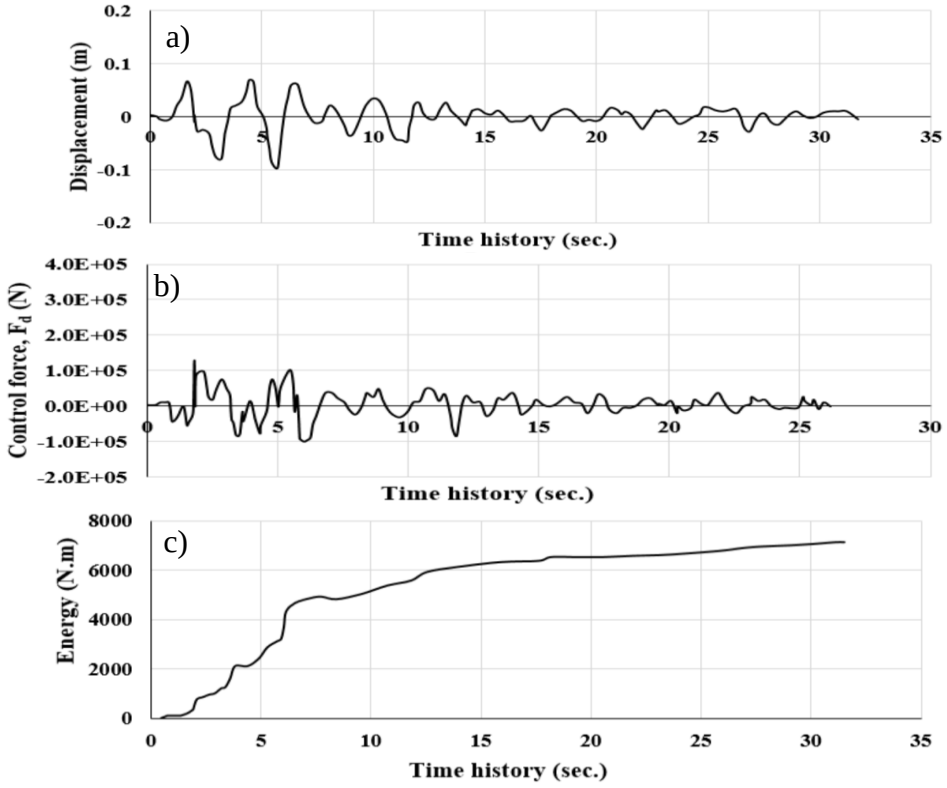

Figure 4-7. Controlled displacement, control force, and energy of control at the top floor of the ten-story building under the El Centro earthquake (a)-(c).

4.5.4. Effects of noise interferences on structural control

Presence of noise in collected data is inevitable. Different methods have been proposed for offline and online noise filtering. Among them, the Kalman filter [105] have been used for studies on structural vibration control and damage identification. The block diagram of typical application of Kalman filter is shown in Figure 4-.

The Kalman filter tries to estimate the state vector z_i of the descerete control system for which the governing equation in state-space form is:

$$z_i = \boldsymbol{A} z_{i-1} + \boldsymbol{B} u_{i-1} + w_{i-1} \tag{4-19}$$

$$y_i = \boldsymbol{C} z_i + v_i \tag{4-20}$$

where y_i is the measurement vector; C is output matrix; and w_i and v_i represent the process and measurement noise, respectively, which are assumed to be independent white Gaussian noises.

$$p(w) \sim N(0, \boldsymbol{Q}), \tag{4-21}$$

$$p(v) \sim N(0, \boldsymbol{R}) \tag{4-22}$$

where Q and R are the process and measurement noise covariance.

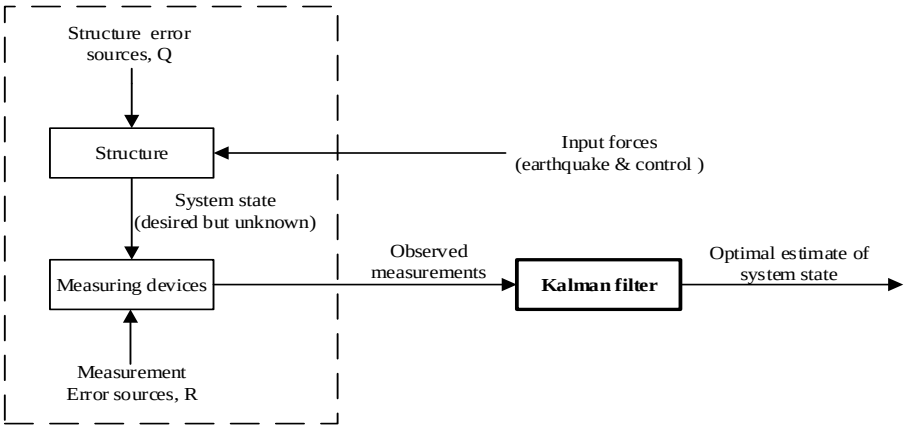

Figure 4-8. Typical application of the Kalman filter [105].

The recursive discrete Kalman filter cycle includes a set of mathematical equations for time update and measurement update, which is given in Figure 4-9 in summary.

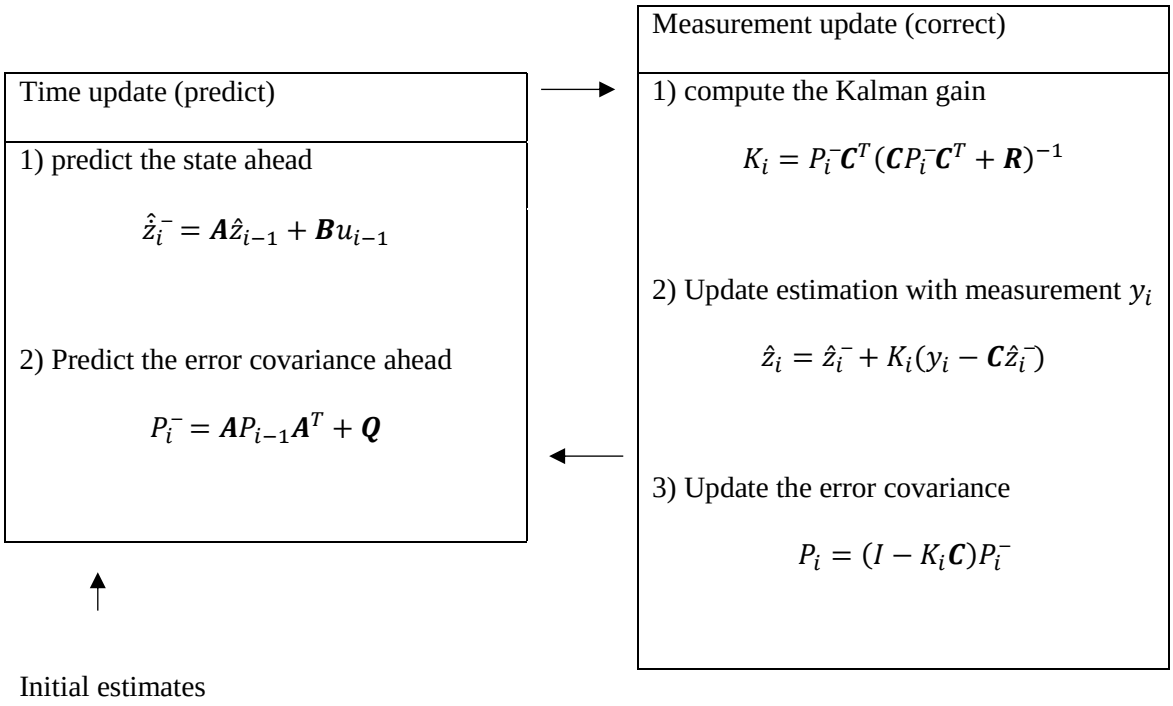

Figure 4-9. Flowchart of the Kalman filter algorithm.

Two cases are considered to demonstrate the effectiveness in reducing the noise in real-time using the Kalman filter. For both cases, $Q = 10^{-9} \times I_{n\times n}$, $R_{Case\text{-}I} = 10^{-5} \times I_{n\times n}$, and $R_{Case\text{-}II} = 10^{-6} \times I_{n\times n}$. Figure 4-(a)-(b) show the measured and filtered displacement responses at the first story of the five-story building under El Centro earthquake. Figure 4-(b) shows the zoomed plot for the selected time window and it is clearly that the Kalman filter significantly reduces the noise effects in the measured displacement, and for both cases, the filtered data match well with each other.

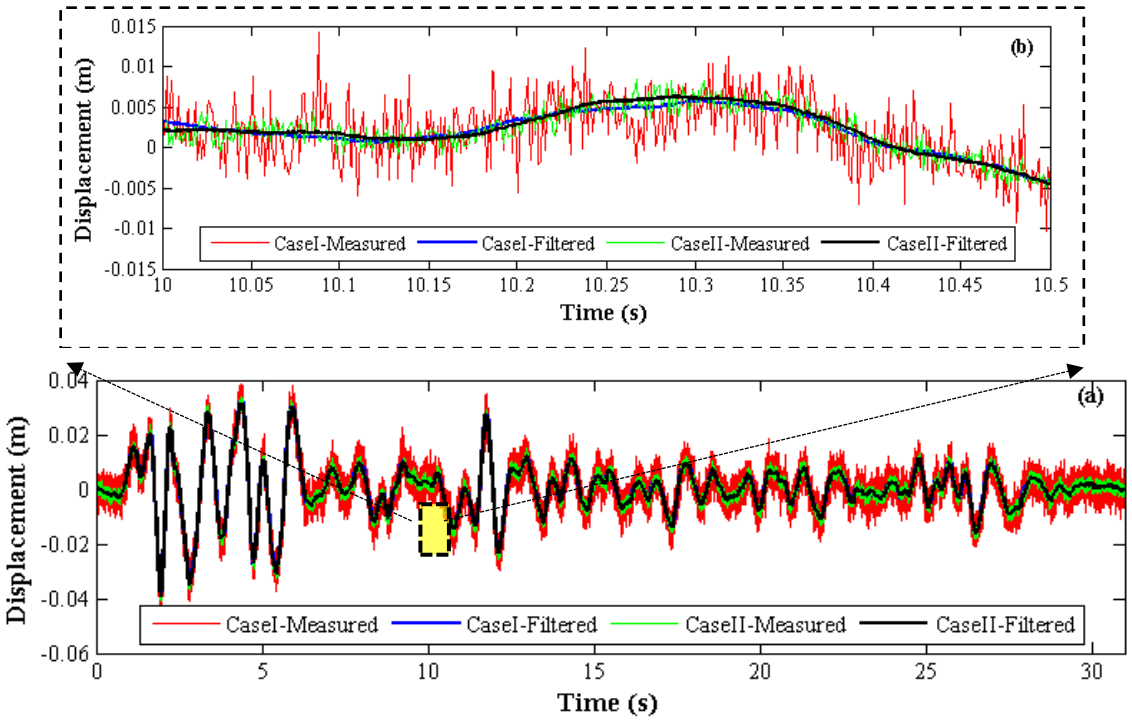

Figure 4-10. Displacement response of first story of five-story building before and after Kalman filter under El Centro earthquake loading: (a) the time history and (b) zoomed time window.

4.6. Summary

In this study, we demonstrate the steps of dynamic structures with control system and use a numerical example for assessing the effectiveness of seismic response mitigation. Performance metrics are used to evaluate the effectiveness of the controlled structures, including performance index, energy of control, and noise interference. The data fusion for raw sensor data is crucial to implement the control systems, since the collected data could be contaminated by various operating conditions. Clearly, the Kalman filter can effectively reduce the noise effects and avoid potential error in estimating controlling parameters.

5. WAVELET-BASED SEMI-ACTIVE CONTROL INTEGRATED WITH DAMAGE DETECTION FOR BASE-ISOLATED BUILDINGS

Buildings installed with control systems may still suffer from a certain level of damage under an earthquake event [26, 101]. Such damage requires different control forces to mitigate seismic response, as compared to undamaged ones, when subjected to next earthquake event. As a result, control systems for buildings require initial input data from damage detection technologies. Although structural damage detection and structural vibration control have gained enormous attentions, most of them have been treated separately according to their individual objectives. Only a few studies [26, 101, 116, 117] have been developed to investigate the integration of damage detection with vibration control. Based on the previous studies by Amini and his co-workers in the literature [26, 101], this study explores the control algorithm integrated with a damage detection technique for base-isolation system. Identical to [26, 56, 57], the Natural Excitation Technique (Next) and Eigen system Realization Algorithm (ERA) methods are used for system identification purpose, while a fuzzy logic controller with wavelet analysis is used for control purpose. Using the system identification method, the modal parameters are identified, and the stiffness matrix is estimated. Then, the damage index is obtained by comparing the results from undamaged and damaged systems. The calculated index is used for determining the control force through the fuzzy logic controller [26, 81]. Since the natural frequencies of the structure would change during an earthquake, wavelet time-frequency analysis of excitation is used as a complementary powerful tool to minimize the resonance effect by updating the control force adaptively. Finally, the calculated control force is applied to the base of the structure using Magnetorheological (MR) damper.

5.1. Base-isolated structure

The governing equations of an *n*-DOF subjected to earthquake ground motion and control force, are usually described as follows [26, 98, 101]:

$$[M]\{\ddot{x}(t)\} + [C]\{\dot{x}(t)\} + [K]\{x(t)\} = [D]\{u(t)\} - [M]\{E\}\ddot{x}_g(t) \tag{5-1}$$

where, M, C and K denote $n \times n$ mass, damping and stiffness matrices, respectively; x, ẋ, ẍ are the $n \times 1$ nodal displacement, velocity and acceleration vectors, respectively. *E* is an $n \times 1$ influence factor which is a vector of all ones, and *D* is $n \times n$ location matrix. $u(t)$ is $n \times 1$ control force vector [11]. Naeim and Kelly [106] described a 2-DOF base isolated system, that can be expanded to MDOF systems [26], as follows:

$$\begin{bmatrix} m+m_b & m \\ m & m \end{bmatrix}\begin{Bmatrix} \ddot{x}_b \\ \ddot{x}_s \end{Bmatrix} + \begin{bmatrix} c_b & 0 \\ 0 & c_s \end{bmatrix}\begin{Bmatrix} \dot{x}_b \\ \dot{x}_s \end{Bmatrix} + \begin{bmatrix} k_b & 0 \\ 0 & k_s \end{bmatrix}\begin{Bmatrix} x_b \\ x_s \end{Bmatrix} = -\begin{bmatrix} m+m_b & m \\ m & m \end{bmatrix}\begin{Bmatrix} \ddot{u}_g \\ 0 \end{Bmatrix} \tag{5-2}$$

The Equation (5-2) can be rewritten as Equation (5-3) for n-DOF isolated system as [26]:

$$\begin{bmatrix} m_{total}+m_b & r^T M \\ Mr & M \end{bmatrix}\begin{Bmatrix} \ddot{x}_b \\ \ddot{x}_s \end{Bmatrix} + \begin{bmatrix} c_b & 0 \\ 0 & C \end{bmatrix}\begin{Bmatrix} \dot{x}_b \\ \dot{x}_s \end{Bmatrix} + \begin{bmatrix} k_b & 0 \\ 0 & K \end{bmatrix}\begin{Bmatrix} x_b \\ x_s \end{Bmatrix} = -\begin{bmatrix} m_{total}+m_b & r^T M \\ Mr & M \end{bmatrix}\begin{Bmatrix} \ddot{u}_g \\ 0 \end{Bmatrix} \tag{5-3}$$

The nonlinear behavior of a seismically isolated structure can be explained by nonlinear deformation of the superstructure earthquake resisting system as well as the isolation system. In this study, since the earthquake resisting system is much more stiffer than the base-isolators, it is reasonably assumed that only isolation system elements exhibit post-yield behavior [12]. The mechanical behavior of seismic base-isolators are extensively studies and documented. It has been shown that consideration of bilinear behavior of base isolation system reflects the actual performance of structure with acceptable accuracy [26, 107]. In this study, the bilinear model is used to express the relationship between the shear force and the lateral displacement, because it is simple and fits both rubber-based and sliding-based type of isolators. The bilinear model of the isolation system is determined by three parameters: elastic stiffness (K_e), post-yield stiffness

(K_p) and characteristic strength (Q), for prediction of a satisfactory estimation of the nonlinear behavior of the base-isolation system.

The restoring force of the isolator, $k_b x_b$ in the Equation (5-3) can be calculated [26, 107]:

$$F = \begin{cases} k_e[\alpha x + (1-\alpha)x_y] & if \quad -(x_d - 2x_y) \le x \le x_d \ and \ \dot{x} > 0 \\ k_e[x - (1-\alpha)(x_d - x_y)] & if \quad (x_d - 2x_y) \le x \le x_d \ and \ \dot{x} < 0 \\ k_e[\alpha x - (1-\alpha)x_y] & if \quad -x_d \le x \le (x_d - 2x_y) \ and \ \dot{x} < 0 \\ k_e[x + (1-\alpha)(x_d - x_y)] & if \quad -x_d \le x \le -(x_d - 2x_y) \ and \ \dot{x} > 0 \end{cases} \tag{5-4}$$

5.2. System identification and damage detection

5.2.1. ERA/NExT damage detection algorithm

Structural health monitoring (SHM) is the strategy for implementing damage detection process for aerospace, mechanical, and civil engineering infrastructures. For many in-suite structure the data using for damage detection was excited by ambient excitation. Using NExT for estimating parameters is based on the ambient excitation technique [56, 57]. In this theory, cross correlation function is used for getting the modal parameters. The multi degree of freedom vibration differential equation is:

$$M\ddot{x}(t) + C\dot{x}(t) + Kx(t) = F(t) \tag{5-5}$$

where M, C, and K are the mass, damping, and stiffness matrices, respectively; $x(t)$,$\dot{x}(t)$,$\ddot{x}(t)$ are the vectors of displacement, velocity, and acceleration. By post-multiplying the Equation (5-5) by the vector $x_i(s)$ and taking the expected value, the equation of motion can be rewritten as:

$$ME[\ddot{x}(t)x_i(s)] + CE[\dot{x}(t)x_i(s)] + KE[x(t)x_i(s)] = E[F(t)x_i(s)] \tag{5-6}$$

By using the correlation function, $R(.)$, Equation (5-6) can be written as:

$$MR_{\ddot{x}x_i}(t,s) + CR_{\dot{x}x_i}(t,s) + KR_{xx_i}(t,s) = R_{Fx_i}(t,s) \tag{5-7}$$

5.2.2. ERA methods for modal identification

The ERA method is an effective identification method for modal parameters identification [56, 57]. The discrete state-space equations are defined as [26, 124]:

$$x_{k+1} = Ax_k + Bu_k \tag{5-8}$$

$$y_k = Cx_k \tag{5-9}$$

where A, B, and C are the system matrix, input matrix, output matrix, respectively. For civil engineering applications, it is difficult to get the excitation information using NExT to acquire data. Thus, Equation (5-10) can be written as a discrete-time stochastic state-space model as [125]:

$$x_{k+1} = Ax_k + w_k \tag{5-10}$$

$$y_k = Cx_k + v_k \tag{5-11}$$

where w_k and v_k are the white Gaussian noise terms that satisfies the following equation [125];

$$E\left[\begin{pmatrix} w_p \\ v_p \end{pmatrix}\begin{pmatrix} w_q^T & V_q^T \end{pmatrix}\right] = \begin{pmatrix} Q & S \\ S^T & R \end{pmatrix}\delta_{pq} \tag{5-12}$$

where δ_{pq} is the Kronecker delta function. p and q are arbitrary time instants. Two assumptions are considered for the stochastic systems; the process is stationary with zero mean, and they are independent from each other;

$$E[x_k x_k^T] = \Sigma\,, \qquad E[x_k] = 0 \tag{5-13}$$

where the covariance matrix Σ is independent from the time step k. The statistic relationship of x_k, w_k, and v_k can be written as [56]:

$$E[x_k w_k^T] = 0\ \ , \qquad E[x_k v_k^T] = 0 \tag{5-14}$$

The covariance matrices $R_i \epsilon \mathbb{R}^{l\times l}$ can be defined as:

$$R_i = E[y_{k+i} y_k^T] \tag{5-15}$$

where i is time lag. The NExT state-output covariance matrix $G \in \mathbb{R}^{n\times l}$ is defined as [56]:

$$G = E[x_{k+i} y_k^T] \tag{5-16}$$

For stationarity process, it is easy to obtain following properties [126].

$$R_i = CA^{i-1}G \quad , for\ i = 1,2,\dots \tag{5-17}$$

$$R_{-i} = G^T\left(A^{i-1}\right)^T C^T \quad , for\ i = 1,2,\dots \tag{5-18}$$

The output covariances are gathered in a block Toepliz matrix T as [126]:

$$T_{1|i} = \begin{pmatrix} R_i & R_{i-1} & \cdots & R_1 \\ R_{i+1} & R_i & & R_2 \\ \vdots & & \ddots & \vdots \\ R_{2i-1} & R_{2i-2} & \cdots & R_i \end{pmatrix} = \begin{pmatrix} C \\ CA \\ \cdots \\ CA^{i-1} \end{pmatrix} \underbrace{\begin{pmatrix} A^{i-1}G & \cdots & AG & G \end{pmatrix}}_{\vec{n}} = O_i\Gamma_i \tag{5-19}$$

where O_i and Γ_i are the extended observability matrix and the extended stochastic controllability matrix, respectively. It is easy to get the output matrix, C, from the definition of

$$C = O_i(1{:}\,l, :) \tag{5-20}$$

Applying the single value decomposition (SVD) to the Toeplitz matrix, the singular values and the orthogonal matrices can be determined [126];

$$T_{1|i} = USV^T = \begin{pmatrix} U_1 & U_2 \end{pmatrix} \begin{pmatrix} S_1 & 0 \\ 0 & 0 \end{pmatrix} \begin{pmatrix} V_1^T \\ V_2^T \end{pmatrix} \tag{5-21}$$

where U and V are the orthonormal matrices, and S_1 is a diagonal matrix of the singular values in descending order. A shifted block Toeplitz matrix can be defined as:

$$T_{2|i+1} = O_i A \Gamma_i \tag{5-22}$$

Matrix A can be solved using Equation (5-21) and Equation (5-22):

$$A = O_i^{\dagger} T_{2|i+1} \Gamma_i^{\dagger} = S_1^{-\frac{1}{2}} U_1^T T_{2|i+1} V_1 S_1^{-\frac{1}{2}} \tag{5-23}$$

where $(\cdot)^{\dagger}$ is an operator to get the pseudo-inverse of the matrix. Once the A and C matrices are determined, the mode shapes can be obtained using the following equations;

$$A = \Psi \Lambda \Psi^{-1} \tag{5-24}$$

$$V = C\Psi \tag{5-25}$$

5.2.3. Least squares solution of the eigenvalue problem

For the representative MDOF system of the building, the mass and stiffness matrices are defined in the following form:

$$M = \begin{bmatrix} m_1 & 0 & \cdots & 0 \\ 0 & m_2 & & 0 \\ \vdots & & \ddots & \vdots \\ 0 & 0 & \cdots & m_n \end{bmatrix} \tag{5-26}$$

$$K = \begin{bmatrix} k_1 + k_2 & -k_2 & \cdots & 0 \\ -k_2 & k_2 + k_3 & & 0 \\ \vdots & & \ddots & \vdots \\ 0 & 0 & \cdots & k_n \end{bmatrix} \tag{5-27}$$

The eigenvalue problem of a typical dynamic system can be solved using the following equation:

$$\left(K - \lambda_j M\right)\phi_j = 0 \qquad or \qquad K\phi_j = \lambda_j M\phi_j \tag{5-28}$$

Using the normalized mode shapes and the eigenvalues from the previous step, Equation (5-25), the relationship between the eigenvalues and the eigenvectors can be expressed as [127]:

$$\Delta_j\{k\} = \{\Lambda_j\} \tag{5-29}$$

where

$$\Delta_j = \begin{pmatrix} \phi_{1,j} & \phi_{1,j} - \phi_{2,j} & 0 & \cdots & 0 \\ 0 & \phi_{2,j} - \phi_{1,j} & \phi_{2,j} - \phi_{3,j} & & 0 \\ & & \vdots & \ddots & \vdots \\ 0 & 0 & 0 & \cdots & \phi_{n,j} - \phi_{n-1,j} \end{pmatrix} \tag{5-30}$$

$$\{k\} = \begin{bmatrix} k_1 \\ k_2 \\ \vdots \\ k_n \end{bmatrix} \tag{5-31}$$

$$\{\Lambda_j\} = \begin{bmatrix} \phi_{1,j}\lambda_j m_1 \\ \phi_{2,j}\lambda_j m_2 \\ \vdots \\ \phi_{n,j}\lambda_j m_n \end{bmatrix} \tag{5-32}$$

where $\phi_{i,j}$ is the i^{th} element of ϕ_j. Each eigenvalue and eigenvector satisfies Equation (5-29); therefore, they can be written in the following form [127]:

$$\begin{bmatrix} \Delta_1 \\ \Delta_2 \\ \vdots \\ \Delta_n \end{bmatrix} \begin{bmatrix} k_1 \\ k_2 \\ \vdots \\ k_n \end{bmatrix} = \begin{bmatrix} \Lambda_1 \\ \Lambda_2 \\ \vdots \\ \Lambda_n \end{bmatrix} \tag{5-33}$$

To solve the Equation (5-33), the pseudo-inverse matrix method and least squares estimate are used to estimate the stiffness matrix [26];

$$\widehat{K} = \Delta^{\dagger}\Lambda \tag{5-34}$$

The damage is defined as [26]:

$$\Delta k(\%) = \frac{|k_0 - k_d|}{k_0} \times 100 \tag{5-35}$$

where k_0 and k_d are the stiffness matrices for the undamaged and the damaged buildings.

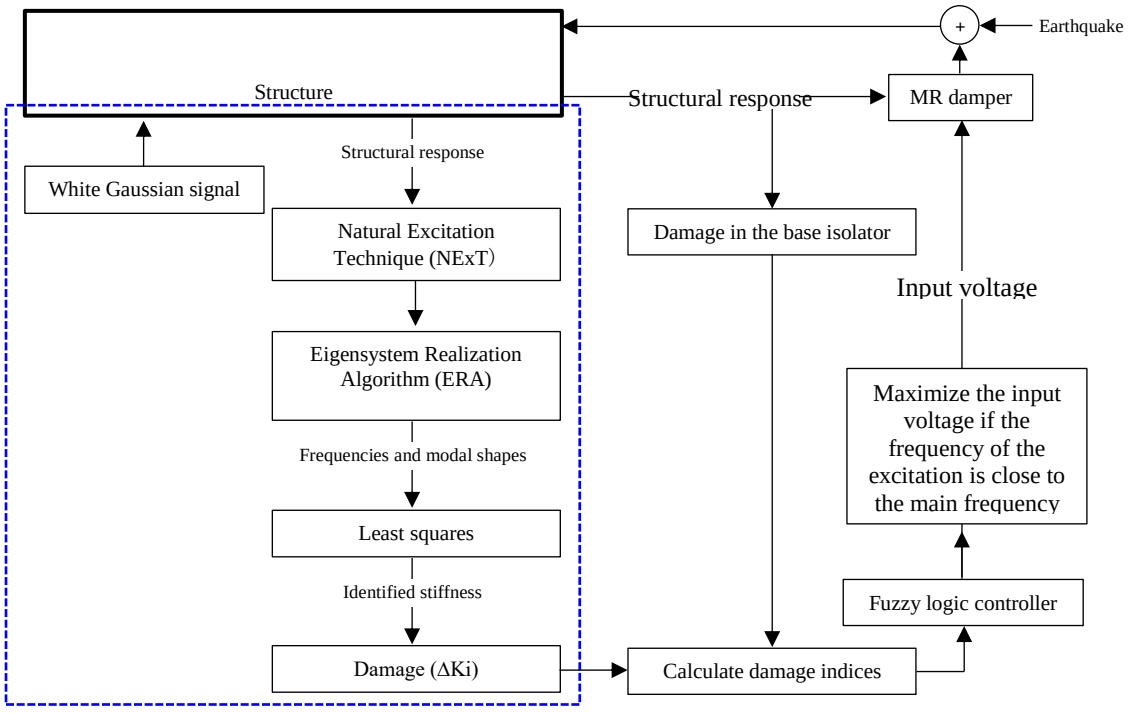

Figure 5-1. Flowchart of the control method.

Two damage case (25% damage in 1st or 3rd story level) are considered in this study to investigate the performance of the proposed algorithm. Since using accelerometers are frequently recommended as a cost effective devices for measuring the response of structure, damage in base-isolation is defined based on the base level acceleration and results are presented in Figure 5-2 and 5-3.

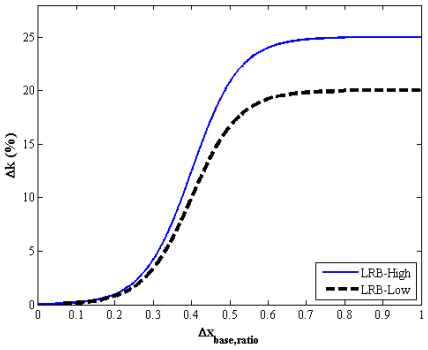

Figure 5-2. Damage intensity vs. base acceleration for two types of isolation systems.

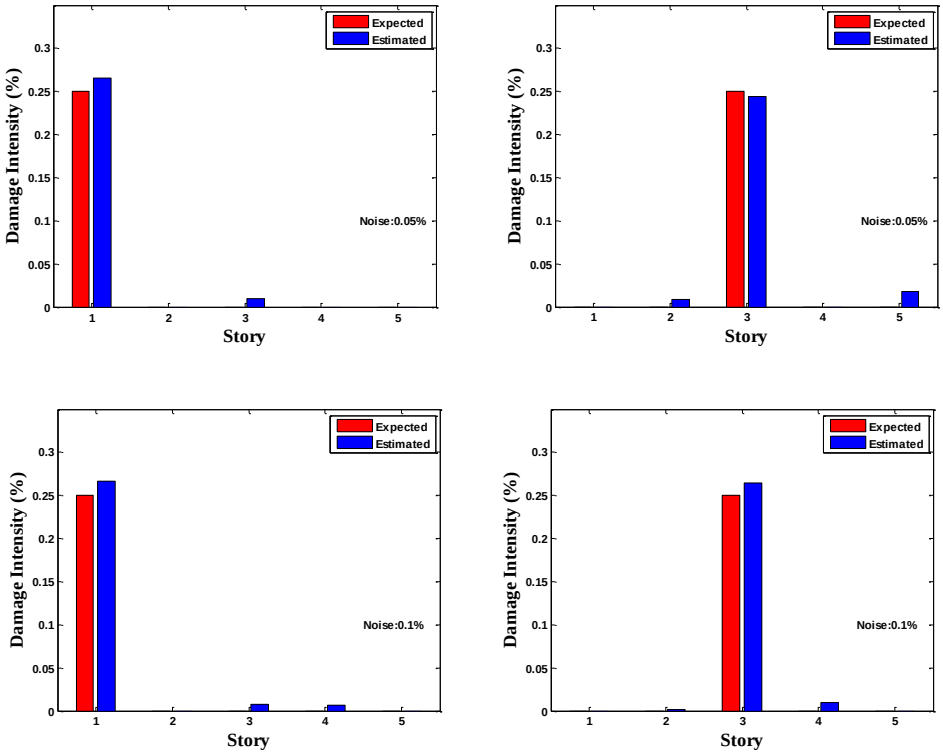

Figure 5-3. Expected and estimated damage intensity using subspace identification.

From Figure 5-2, it is assumed that the induced damage is less than 5% when the measured base acceleration is under 3 g, and the maximum damage intensity reaches to 20% and 25% for LRB-low and LRB-high base isolators, respectively. The accuracy of the damage detection algorithm is shown in Figure 5-3 for the two damage cases with and without noise in the measurement. For the damage detection of the superstructure, the base level is considered to be fixed.

5.3. Fuzzy logic control

The fuzzy logic controller [26, 46, 81, 96, 101, 110] (WDFLC in this section) employs the damage index R_d and damage index rate dR_d as two input variables to calculate the output variable which is the command voltage V of the damper in this study. Similar to the previous studies by Amini and his co-workers in the literature [26, 101], R_d and dR_d are defined:

$$R_d\ (\%) = \sqrt{\frac{1}{2n}\sum_{i=1}^{n}\beta_i^2 \Delta k_i^2} \tag{5-36}$$

$$dR_d = \tan^{-1}\left(\frac{\partial R_d}{\partial t}\right) \tag{5-37}$$

where Δk_i is the damage at i^{th} level with importance factor of β_i.

The input variable dR_d is defined using five Gaussian membership functions with fuzzy sets of [26, 101]: NL=negative large, NS=negative small, Z=zero, PS=positive small, and PL=positive large. Similarly, R_d and V variables are defined using five Gaussian membership functions with fuzzy sets of: Z=zero, S=small, M=Medium, L=large, and VL=very large. The conditional control rules are defines using 25 IF-THEN statements that are given in Table 5-1. Figure 5-4 shows the relationship between the inputs and the output variables. The logic that is used to build the rules is that: if the damage index is high and still increasing, then the output voltage is large. When the output voltage is zero, the damper acts as a passive damper.

Table 5-1. Fuzzy rules used for the WDFLC [26, 101].

		dR_d				
		NL	**NS**	**Z**	**PS**	**PL**
R_d	**Z**	Z	Z	Z	S	M
	S	Z	Z	S	M	L
	M	Z	S	M	L	VL
	L	S	M	L	VL	VL
	VL	M	L	VL	VL	VL

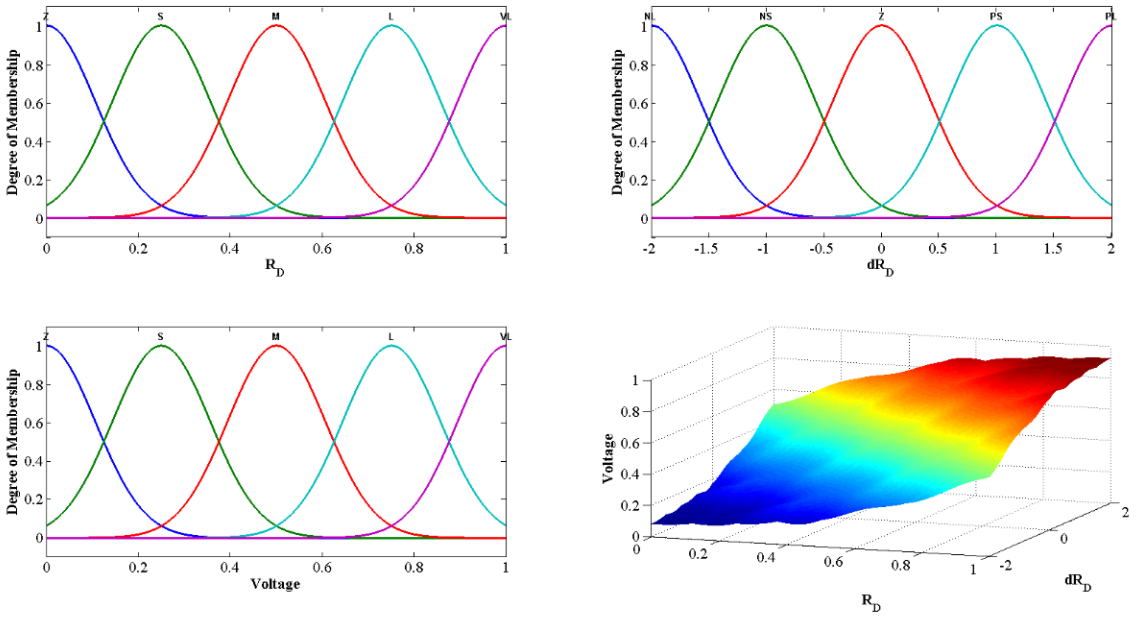

Figure 5-4. Membership functions and the relationship between the input and output variables of WDFLC [101].

The second fuzzy logic controller (FLC in this section) was designed based on the velocity and displacement of the base level; the output variable is the command voltage of the damper in this controller, as well. Input variables are defined using seven Gaussian membership functions with fuzzy sets of: NL=negative large, NM=negative medium, NS=negative small, ZE=zero, PS=positive small, PM=positive medium, PL=positive large. The output variable is defined using five Gaussian membership functions with fuzzy sets of: Z=zero, S=small, L=large, VL=very large. Since the center of area is selected as the defuzzification method, for

both FLC and WDFLC, the output voltage is always a positive number, which is scaled by the maximum voltage in Figure 5-5.

Table 5-2. Conditional fuzzy rules used for the FLC.

	Displacement							
	Voltage	**NL**	**NM**	**NS**	**ZE**	**PS**	**PM**	**PL**
Velocity	**NL**	VL	VL	L	L	M	S	Z
	NM	VL	L	L	M	S	Z	S
	NS	L	L	M	S	Z	S	M
	ZE	L	M	S	Z	S	M	L
	PS	M	S	Z	S	M	L	L
	PM	S	Z	S	M	L	L	VL
	PL	Z	S	M	L	L	VL	VL

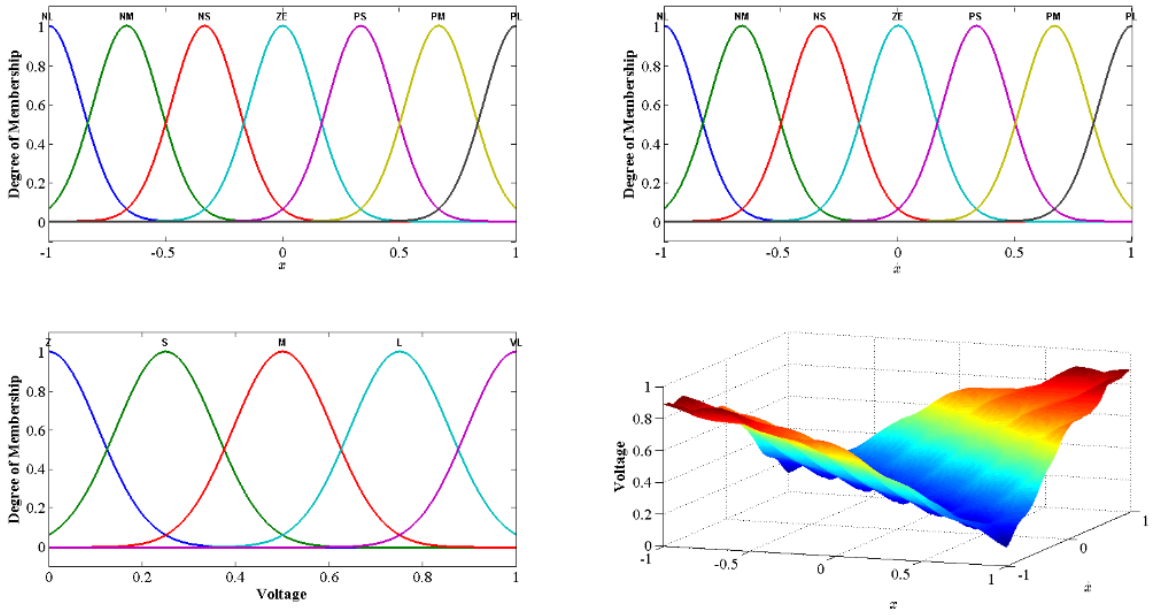

Figure 5-5. Membership functions and the relationship between the input and output variables of FLC.

5.4. Wavelet analysis

Natural frequencies of a structure would be changed during an earthquake, wavelet time-frequency analysis of excitation is used herein as a complementary tool to minimize the

resonance effect by updating the control force adaptively [46, 81, 96, 110]. Wavelet transform is a time frequency decomposition methods [119-123]. The excellent local zooming property of wavelet made it become a very popular tool for analyzing nonstationary signals. Commonly, continuous wavelet transformation (CWT) is used for continuous signals as [121]:

$$Wx(a,b) = x \otimes \psi_{b,a}(t) = \frac{1}{\sqrt{a}} \int_{-\infty}^{+\infty} x(t)\psi^* \left(\frac{t-b}{a}\right) dt \tag{5-38}$$

where * denotes complex conjugation, and a and b are the scale and translation factors, respectively. Using the Equation (5-38), the signal $x(t)$ is decomposed into basic function $\psi\left(\frac{t-b}{a}\right)$ called the mother wavelet, using the wavelet transform.

Usually, the scale factor a is set to be equal to 2. The frequency spectrum of the wavelet stretch by a factor of 2 and all frequency components shift up by a factor of 2. Thus, discrete wavelet transform (DWT) can be obtained by [119, 120]:

$$Wx(j,k) = \int_{-\infty}^{+\infty} x(t) 2^{\frac{j}{2}} \psi^*(2^j t - k) dt \tag{5-39}$$

Wavelet packet analysis [121] consist of a further generalized wavelet transform, which has different time-frequency windows to decompose signals that are not convenient in the wavelet decomposition. A wavelet packet function can be written as [121]:

$$\psi^{\mathrm{i}}_{j,k}(t) = 2^{\frac{j}{2}} \psi^i\left(2^j t - k\right) \quad i = 1, 2, \ldots \tag{5-40}$$

where i, j, and k are the modulation, the scale, and the translation parameter, respectively.

ψ^i is obtained by using recursive relationship:

$$\psi^{2i}(t) = \sqrt{2} \sum_{k=-\infty}^{\infty} h(k)\psi^i(2t-k) \tag{5-41}$$

$$\psi^{2i+1}(t) = \sqrt{2} \sum_{k=-\infty}^{\infty} g(k)\psi^i(2t-k) \tag{5-42}$$

where $h(k)$ and $g(k)$ are the quadrature mirror filters that are determined by mother wavelet function and scaling function. ψ^1 is the mother wavelet and it has some significant properties including invertibility and orthogonality.

Wavelet packets have an adjustable time and frequency resolution [121]. They have different time and frequency resolutions at every level. The top level has higher resolution in the time domain and the bottom level has higher resolution in the frequency domain. The frequency recursive relations are shown in Figure 5-6 that shows a full 3rd level wavelet packet decomposition.

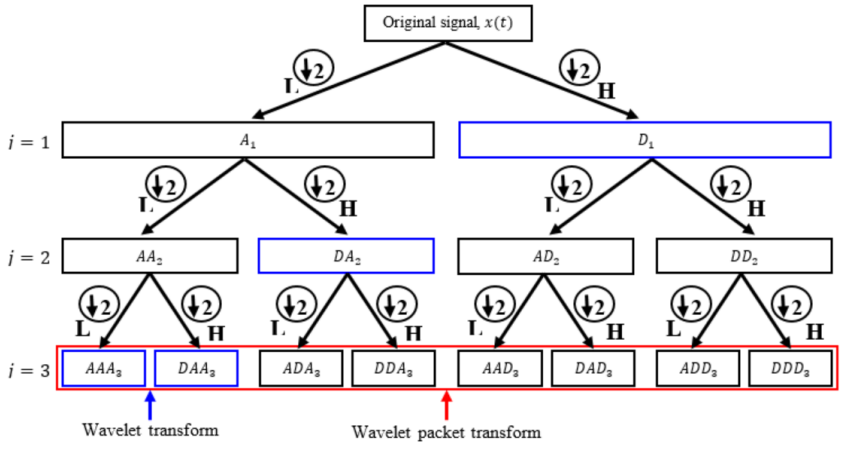

Figure 5-6. The 3rd level wavelet transform and wavelet packet transform.

The blue box and the red box indicate the wavelet transform and the wavelet packet transform of the signal $x(t)$. *H* means high-pass filtering and *L* means low-pass filtering, and *A* and *D* are the approximation and detail coefficients, respectively. The recursive relations between the j^{th} and the $(j+1)^{th}$ level are:

$$x_j^i(t) = x_{j+1}^{2i-1}(t) + x_{j+1}^{2i}(t) \tag{5-43}$$

$$x_{j+1}^{2i-1}(t) = (x_j^i(t) * h) \downarrow 2 \tag{5-44}$$

$$x_{j+1}^{2i}(t) = (x_j^i(t) * g) \downarrow 2 \tag{5-45}$$

5.5. Numerical example

5.5.1. Dynamic properties of the building model

In this section, in order to investigate the performance of the integrated method for damage detection and control, a five-story based-isolated building is selected from the studies conducted by Ozbulut et al. and Amini et al. [21, 26], as shown in Figure 5-7.

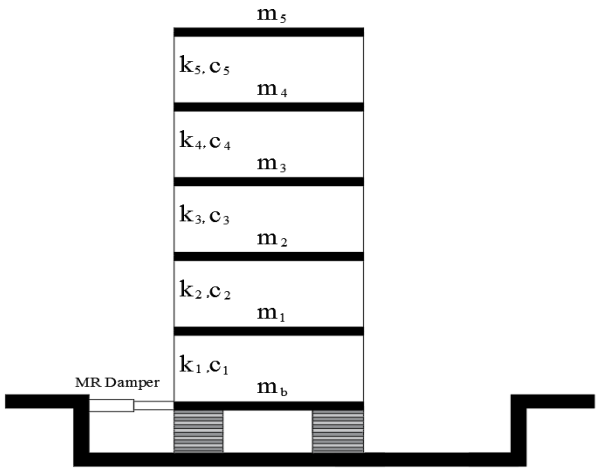

Figure 5-7. The dynamic model of the five-story base-isolated building [21, 26].

The building is simulated as a lumped-mass model representing a shear frame with one degree of freedom for each floor. Dynamic properties of the model are given in Table 5-3. The Rayleigh method is used to get the damping matrix based on the mass and stiffness matrices [99]. An inherent damping of 2% is assumed for the first two modes of vibration. Base-isolators are simulated based on the bilinear model for two types of low- and high- lead rubber bearing (LRB). The dynamic properties of LRB devices are given in

Table 5-4. The augmented model of the five-story building with isolation system is a six-degree-of-freedom system.

In this study, it is reasonably assumed that the super structure remains linear, and the control force is applied to the base level using a 50 kN MR damper.

Modal analysis of the structures shows that the first mode of vibration is the most effective mode, and therefore, the first natural frequency of the structure is compared with the ground motion frequency for each time-step during the earthquake, and for the frequencies within the range of $\omega_1 \pm 10\%$, the command voltage is increased to its maximum level, 5 volt.

Table 5-3. Dynamic properties of five-story based-isolated building [26].

Story	**m (kg)**	**k (kN/m)**
5th	5897	19059
4th	5897	24954
3rd	5897	28621
2nd	5897	29093
1st	5897	33732

Table 5-4. Dynamic properties of LRB devices [26].

LRB type	**m (kg)**	**c (kN/m/s)**	**k_e (kN/m)**	**k_p (kN/m)**	**Q (kN)**
LRB-low	6800	7.54	1389	231.5	13890
LRB-high	6800	7.54	2315	231.5	47921

5.5.2. MR damper parameters

In this study, the ten parameters of a 50 kN MR damper are selected based on the models developed by Fu et al. [108] that is also used in ref. [26], and they are given in Table 5-5. The saturation voltage of the damper is 5 V; therefore, the range of the command varies from 0 to 5 volts. Behavior of the MR damper is simulated performing the 4th order Runge-Kutta method [109, 110]. Figure 5-8 shows the force-displacement and force-velocity hysteresis loops for the selected device that is generated using a sinusoidal velocity with an amplitude of 40 cm/s and frequency of 1 Hz.

Table 5-5. MR damper model parameters [26].

Parameter	Value	Parameter	Value
c_{0a}	44 N-s m-1	α_a	108 7200 N m-1
c_{0b}	440 N-s m-1.V	α_b	496 1600 N m-1.V
n	1	Γ	300 m-2
A	1.2	β	300 m-2
η	50 s-1	V_{max}	5

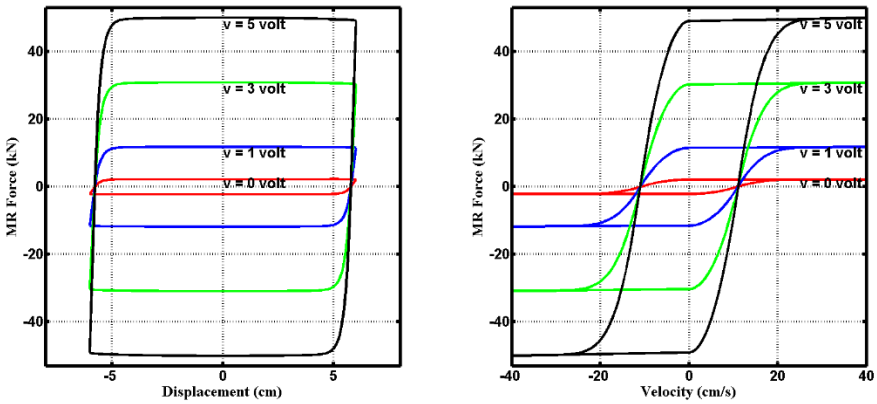

Figure 5-8. Typical force-displacement/velocity hysteresis loops for the 50 kN MR damper.

5.5.3. Earthquake records

Six earthquake records are selected in this research to evaluate the performance of the proposed control method under different external excitations. The characteristics of the selected earthquakes are given in Table 5-6. In addition, elastic acceleration as well as velocity response spectra are plotted in Figure 5-9. All the records are downloaded from PEER ground motion database (http://ngawest2.berkeley.edu/).

Table 5-6. Characteristics of the earthquake records.

Earthquake	Station & Direction	Magnitude (Mw)	PGA (g)	PGV (cm/s)
1940 El Centro	El Centro Array #9 270°	7.2	0.21	30.2
1994 Northridge	Sylmar - Olive View Med FF 360°	6.7	0.84	129.6
1995 Kobe	H1170546.KOB 90°	7.2	0.63	76.6
1999 Chi-Chi	TCU068 N	7.6	0.36	292.2
1971 San Fernando	Pacoima Dam 164°	6.6	1.22	56.2
1989 Loma Prieta	Hollister - South & Pine 0°	6.9	0.37	62.4

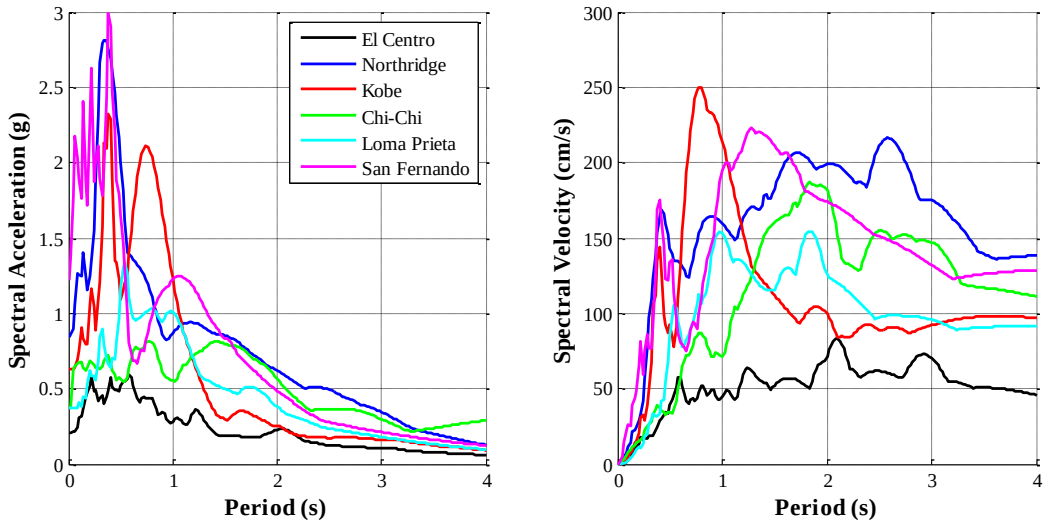

Figure 5-9. Spectral responses for the selected earthquakes.

5.6. Results and discussion

5.6.1. Maximum responses

The time-history analyses of the building were performed in MATLAB for the six historical earthquakes. The response quantities that have been evaluated is this study include: maximum base displacement $x_{b,\max}$, maximum displacement at the roof $x_{\max}$, maximum inter-story drift $d_{s,\max}$, maximum floor acceleration $\ddot{x}_{s,\max}$, and maximum force of the MR damper $F_{d,\max}$. The results of the analyses for the damaged building using the clipped-optimal, passive-max, FLC, and WDFLC control techniques are given in Table 5-7.

Table 5-7. Maximum responses of the damaged base-isolated building.

Earthquake	Response	Uncontrolled	Clipped-Optimal	Passive-max	FLC	WDFLC
El Centro	$x_{b,\max}$ (cm)	7.3 (4.3)	5.1 (4.8)	2.7 (2.2)	4.4 (3.9)	3.7 (2.5)
	$x_{\max}$ (cm)	7.5 (4.8)	5.5 (5.4)	3.6 (3.4)	4.8 (4.6)	4.1 (3.1)
	$d_{s,\max}$ (cm)	0.1 (0.1)	0.2 (0.3)	0.3 (0.4)	0.2 (0.3)	0.2 (0.2)
	$\ddot{x}_{s,\max}$ (cm/s^2)	245.9 (356.5)	379.5 (538.0)	472.8 (469.8)	293.5 (381.6)	262.8 (317.8)
	$F_{d,\max}$ (kN)	-	25.6 (32.2)	49.6 (49.6)	28.1 (29.9)	14.2 (15.6)
Northridge	$x_{b,\max}$ (cm)	42.7 (24.3)	16.9 (11.4)	16.7 (11.0)	32.7 (20.4)	13.5 (10.8)
	$x_{\max}$ (cm)	43.8 (25.1)	17.9 (13.0	17.8 (12.3)	33.6 (21.5)	14.2 (11.8)
	$d_{s,\max}$ (cm)	0.4 (0.3)	0.3 (0.5)	0.3 (0.5)	0.4 (0.4)	0.5 (0.6)
	$\ddot{x}_{s,\max}$ (cm/s^2)	937.9 (983.3)	938.4 (1273.6)	1134.8 (1221.6)	967.0 (1021.1)	996.8 (1155.9)
	$F_{d,\max}$ (kN)	-	50 (50)	50 (50)	28.6 (30)	19.3 (21.2)
Kobe	$x_{b,\max}$ (cm)	14.3 (13.2)	13.1 (12.9)	12.9 (11.3)	11.2 (12.8)	7.3 (7.8)
	$x_{\max}$ (cm)	17.7 (13.9)	13.3 (13.6)	13.6 (12.4)	11.8 (13.9)	7.4 (8.5)
	$d_{s,\max}$ (cm)	0.2 (0.3)	0.3 (0.4)	0.3 (0.4)	0.2 (0.4)	0.5 (0.6)
	$\ddot{x}_{s,\max}$ (cm/s^2)	664.8 (871.1)	841.2 (858.9)	860.0 (856.4)	714.2 (833.1)	645.5 (683.7)
	$F_{d,\max}$ (kN)	-	50 (50)	50 (50)	29.4 (30.2)	20.8 (21.6)
Chi-Chi	$x_{b,\max}$ (cm)	34.9 (13.2	31.2 (11.1)	7.2 (4.7)	26.8 (9.0)	16.2 (6.6)
	$x_{\max}$ (cm)	35.8 (13.9)	32.2 (12.4)	7.8 (5.5)	27.7 (9.8)	16.8 (7.2)
	$d_{s,\max}$ (cm)	0.3 (0.3)	0.4 (0.4)	0.3 (0.4)	0.3 (0.3)	0.3 (0.4)
	$\ddot{x}_{s,\max}$ (cm/s^2)	603.3 (871.1)	515.9 (703.4)	618.3 (621.8)	592.0 (660.4)	566.1 (597.9)
	$F_{d,\max}$ (kN)	-	49.6 (49.6)	49.8 (49.8)	27.8 (23.0)	16.7 (17.7)
San Fernando	$x_{b,\max}$ (cm)	32.8 (26.0)	28.7 (23.5)	18.5 (14.8)	27.7 (20.9)	12.9 (9.5)
	$x_{\max}$ (cm)	33.7 (26.9)	29.8 (24.8)	19.7 (15.9)	28.6 (22.0)	13.4 (10.5)
	$d_{s,\max}$ (cm)	0.3 (0.3)	0.3 (0.4)	0.4 (0.4)	0.3 (0.4)	0.5 (0.5)
	$\ddot{x}_{s,\max}$ (cm/s^2)	1239.6 (1607.2)	1275.1 (1619.4)	1478.5 (1578.7)	1305.2 (1650.0)	1478.1 (1602.7)
	$F_{d,\max}$ (kN)	-	49.8 (49.7)	50 (50)	29.7 (29.3)	24.6 (24.8)
Loma Prieta	$x_{b,\max}$ (cm)	24.6 (16.1)	20.2 (13.8)	11.6 (9.1)	17.6 (12.5)	7.6 (5.6)
	$x_{\max}$ (cm)	25.3 (16.8)	20.9 (14.9)	12.3 (10.2)	18.3 (13.4)	7.9 (6.2)
	$d_{s,\max}$ (cm)	0.2 (0.2)	0.3 (0.4)	0.3 (0.4)	0.3 (0.3)	0.3 (0.4)
	$\ddot{x}_{s,\max}$ (cm/s^2)	493.6 (575.0)	460.4 (669.3)	554.3 (625.9)	435.6 (579.6)	412.8 (471.3)
	$F_{d,\max}$ (kN)	-	23.2 (30.9)	50 (50)	26.4 (27.1)	16.3 (17.5)

In Table 5-7, there are two values per each quantity, which correspond to base-isolation systems using LRB-low and LRB-high, respectively. From this table, it can be seen that the base deformation was significantly reduced using the passive control with the maximum command voltage. However, regardless to the input excitation, the maximum floor acceleration was increased considerably, 200% for the El Centro earthquake and 20% for the Chi-Chi earthquake, which shows the importance of the adaptability of a control system for different earthquakes.

The maximum displacement at the top floor is slightly larger than the base deformation that supports the previous assumptions regarding the elastic behavior of the supper structure.

By comparing the results for the three control strategies, it can be seen that the wavelet based control fuzzy logic control, WDFLC, improves the performance of the base-isolated building concerning the base displacement with small increase of the floor acceleration. For example, there are -30%, 6%, -23%, 9%, and 16% increase in the maximum floor acceleration with respect to the uncontrolled cases for the El Centro, Northridge, Kobe, Chi-Chi, San Fernando, and Loma Prieta earthquakes, respectively, using the WDFLC method, while the peak base displacement is reduced by 27%, 20%, 44%, 48%, 55%, and 62% for the same earthquakes.

5.6.2. Time-history of responses

In order to further investigate the behavior of the building, as well as the performance of the proposed algorithm, the time-history of the displacement at the base level (Figure 5-10a), acceleration at the roof level (Figure 5-10b), and the voltage of the MR damper (Figure 5-10c) are discussed here for the Northridge earthquake. From the base displacement response time-history, it can be seen that under the same circumstance, WDFLC algorithm performs better compared with FLC; the reduction of the peak displacement response is 68% for Northridge earthquake, which is significant with respect to the FLC and clipped-optimal controllers.

As it is explained earlier, it is expected that the acceleration response increases for each DOF of the system when the displacement responses are reduced considerable. However, not only the displacement of the base level is reduced using WDFLC algorithm, but also the maximum acceleration response is not increase more than 5%. The reason for this improvement can be explained using the MR damper voltage time-history plot (Figure 5-10c). This graph shows the input command voltage for each of the control techniques: clipped- optimal passive-

max, FLC, and WDFLC. Using the passive-max method, the displacement is reduced considerably, but with the cost of increase in the acceleration, which is due to the maximum uncontrollable voltage that in send to the MR damper. On the other hand, it can be seen that during the time of excitation, WDFLC algorithm sends similar or higher voltage signals compared to FLC, which results in more reduction for the displacement response. Despite the passive-max algorithm, WFLCD algorithm does not keep the voltage at its maximum possible level except for the time-steps that the main frequency of the structure is critically close to the excitation frequency that is obtained using wavelet transform.

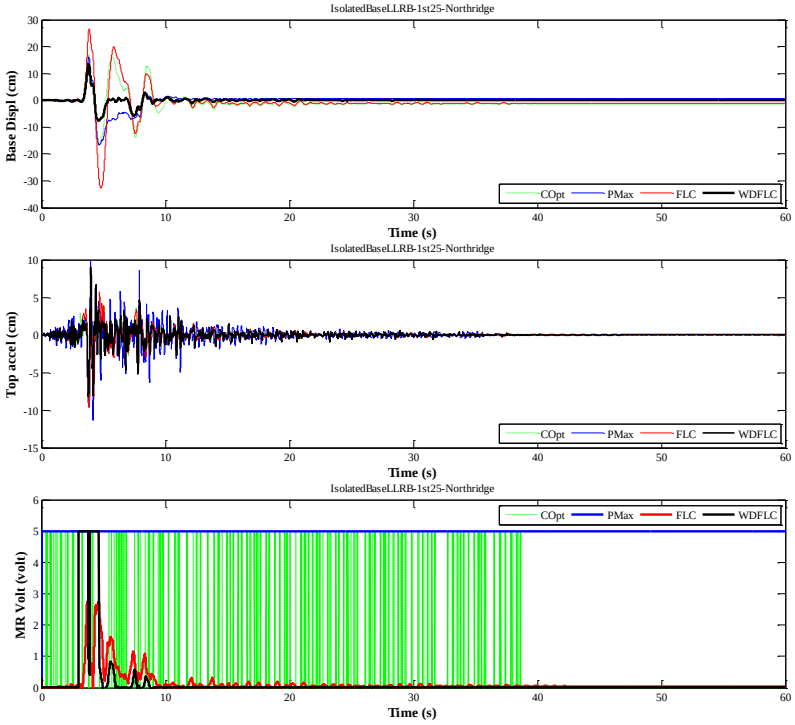

Figure 5-10. Time-history response of the base-isolated building with 25% of damage in the 1st story under Northridge earthquake.

5.6.3. Performance indices

Nine performance indices were used in this study to evaluate the performance of the proposed controller in comparison with the other semi-active controllers as well as the

uncontrolled system. These performance indices are defined based on the structural responses (displacement, acceleration, drift, and shear force) at the base and story levels.

Table 5-8. Nine performance indices that are used in this study.

a. Peak base displacement	b. Peak structure displacement	c. Peak inter-story drift
$J_1 = \frac{\max_t \|x_b(t)\|}{\max_t \|\hat{x}_b(t)\|}$	$J_2 = \frac{\max_t \|x_s(t)\|}{\max_t \|\hat{x}_s(t)\|}$	$J_3 = \frac{\max_{t,f} \|d_f(t)\|}{\max_{t,f} \|\hat{d}_f(t)\|}$
d. Peak base shear	e. Peak shear force	f. Peak control force
$J_4 = \frac{\max_t \|V_b(t)\|}{\max_t \|\hat{V}_b(t)\|}$	$J_5 = \frac{\max_t \|V_s(t)\|}{\max_t \|\hat{V}_s(t)\|}$	$J_6 = \frac{\max_t \|f_d(t)\|}{F_{max}}$
g. Peak floor acceleration	h. RMS base displacement	i. RMS base acceleration
$J_7 = \frac{\max_{t,f} \|a_f(t)\|}{\max_{t,f} \|\hat{a}_f(t)\|}$	$J_8 = \frac{\max_i \|\sigma_d(t)\|}{\max_i \|\sigma_{\hat{d}}(t)\|}$	$J_9 = \frac{\max_i \|\sigma_a(t)\|}{\max_i \|\sigma_{\hat{a}}(t)\|}$

In above equations, $\| \|$=vector magnitude; ˆ=corresponding response quantity in the uncontrolled case (denominators); V_b, V_s=base and structural shear force; x_b, x_s=base and structural displacement; d_f, a_f=floor drift and acceleration; f_d, F_{max}=damper force and maximum force that can be generated using the MR damper; σ_d, σ_a=RMS of base displacement and roof acceleration; t=time 0≤t≤Tfinal.

Figure 5-11 and Figure 5-12 show the nine performance indices for each control strategies for two damaged base-isolated buildings with LRB-low and LRB-high isolators, respectively. From the figures, it is evident that the maximum base displacement, J_1, is reduced more by using the WDFLC compared to the other strategies for all the earthquakes except the Chi-Chi earthquake for which, the passive-max control results in more reduction in the displacement reduction. The best performance is achieved for the Northridge earthquake which has the highest PGA (68% reduction). The peak structure displacement at roof level, J_3, shows a very similar response reduction, because the superstructure experience minimum inter-story drifts in base-isolated buildings. From the J_3 index, however, the inter-story drifts are larger for

the proposed method, but as it is mentioned above, the inter-story drifts in this base-isolated building is very small and negligible, which can be seen from Table 5-7.

Since the base shear force is related to the base displacement, a similar pattern can be seen between J_1 and J_4. For the Northridge earthquake, by using the proposed method, the maximum base shear force is reduced by approximately 60%, that is 8% more than the passive-max and clipped-optimal controllers, and 40% more than the FLC controller.

The index J_6 indicates the maximum generated MR damper force during the earthquake. It is obvious that for the controlled building using the passive-max controller, the ratio is almost constant and equal to 1. For the WDFLC method, despite the significant reduction in the responses, the maximum control force does not reach to the maximum level. On the other hand, since the clipped-optimal control switches the command voltage between the minimum and maximum levels, the maximum control force is higher for this case. It is worth to mention that MR damper force is highly dependent on the relative velocity and displacement in addition to the input voltage, and therefore, for the FLC and WDFLC controllers the maximum control force is less possible to be generated.

The root mean squares (RMS) of the base displacement and base acceleration are shown in Figure 5-12*h* and Figure 5-12*i*, respectively. Both figures confirm that the response reduction using the WDFLC algorithm is considerably high compared to the FLC, clipped-optimal, and the passive-max methods.

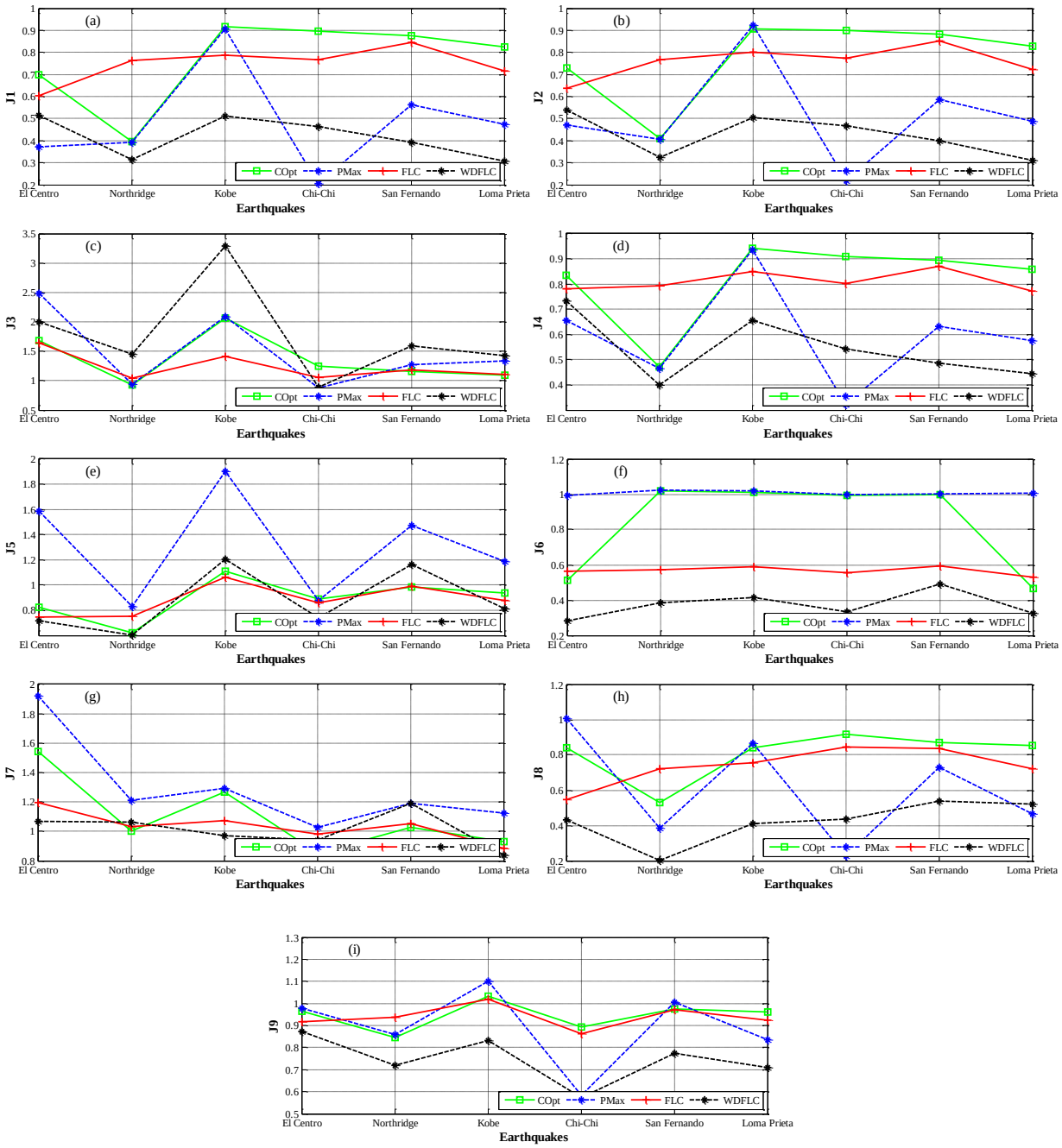

Figure 5-11. Performance indices for the different control methods for 25% damage in the 1st story level (LRB-low).

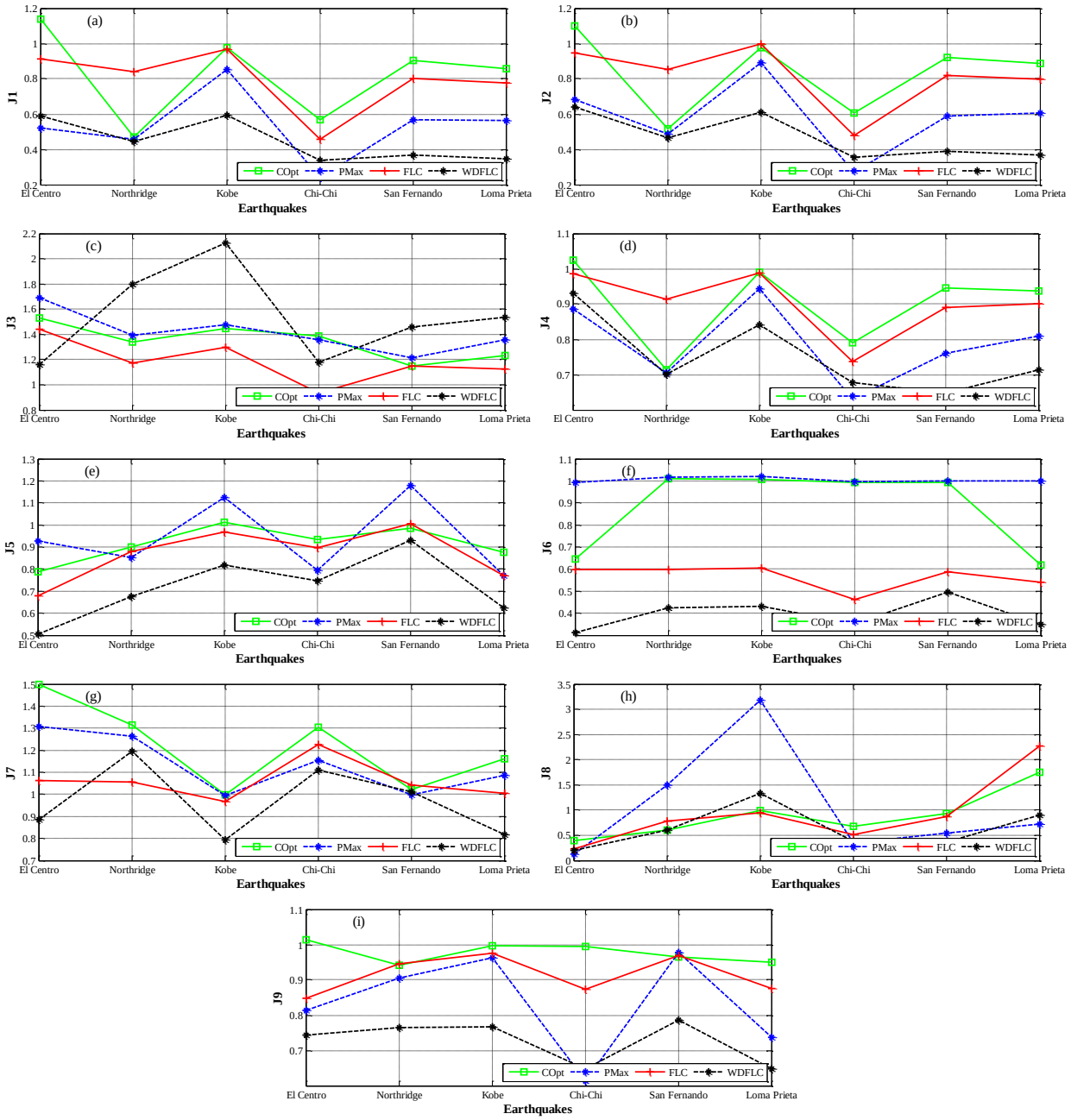

Figure 5-12. Performance indices for the different control methods for 25% damage in the 1st story level (LRB-high).

5.6.4. Energy of control

As we defined in Equation (4-19) in Chapter 4, to evaluate the capability of the proposed method, the energy of control could be used for assessing different the controllers. Energy of control is defined by Equation (4-19):

$$E_c(t) = \int_0^t F_d \dot{x}_b dt$$

where $E_c(t)$ is the energy of control, F_d is the generated MR damper force, and $\dot{x}_b$is the velocity of the base level. Figure 5-13 shows the time-history of the control energy for the base-isolated building with LRB-low under six selected historical earthquakes with different PGAs and characteristics.

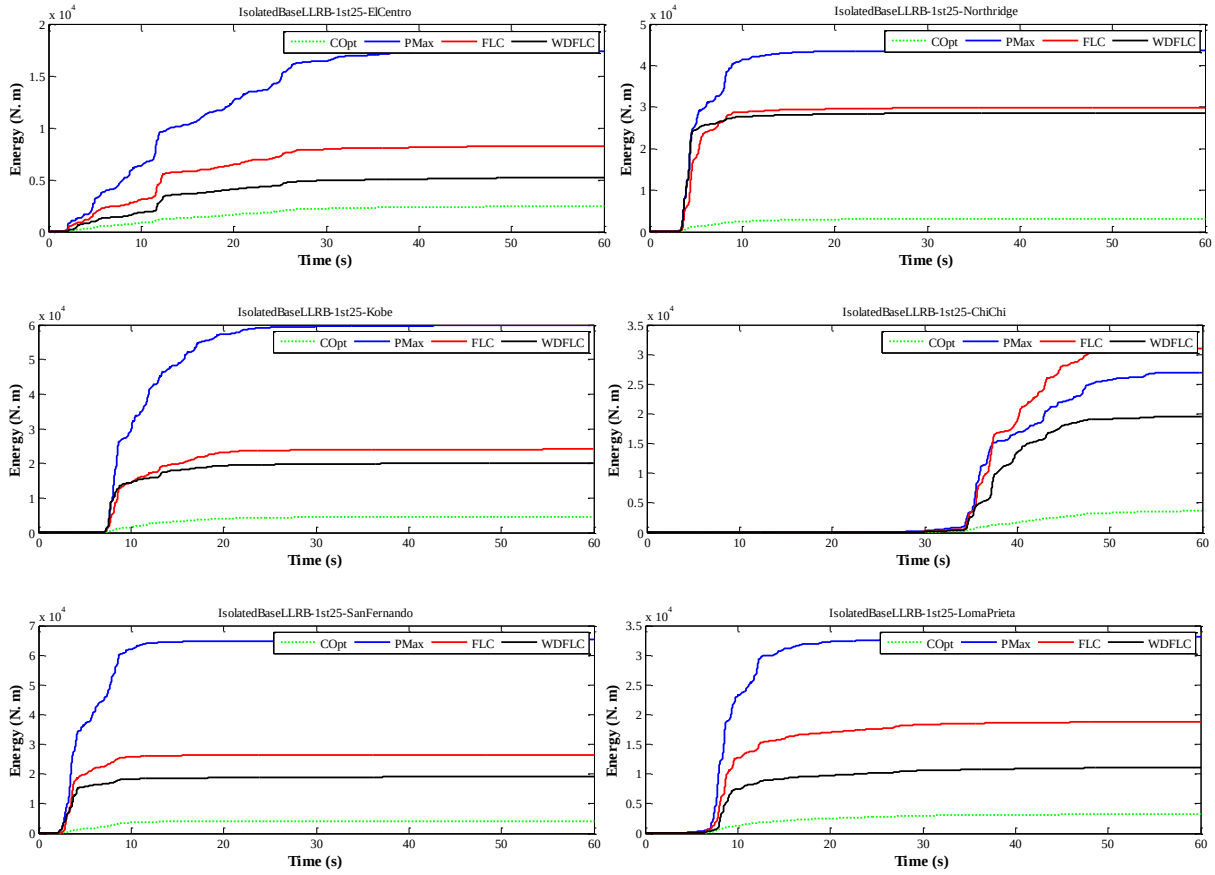

Figure 5-13. Energy of control for the base-isolated building with LRB-low (damage=25% at 1st level).

Under all the earthquakes, the control energy is reduced considerable using the proposed algorithm, WDFLC, compared to the passive-max and FLC controllers. Although the clipped-optimal controller has the minimum control energy, there are some disadvantages for this algorithm. For instance, the command voltage for such controller is not smooth, and therefore, it

is vulnerable to signal delays; in addition, the performance indices of the clipped-optimal control are higher than the proposed control, which reflects the superior performance of the proposed strategy. In sum, considering different earthquakes with different mechanism, the proposed controller reduces the control energy significantly compared to the fuzzy logic control and the passive control with maximum input voltage.

5.7. Summary

To mitigate seismic response of the multistory base-isolated buildings, we discuss the integrated algorithm that consists of two major phases, the pre-earthquake damage detection and the vibration control during an earthquake. For the damage detection part, the Next and ERA methods are used for system identification (with or without damage), while for the vibration control, a semi-active fuzzy logic controller is employed using MR dampers to increase the reliability of the system. For improving the adaptability of the control, wavelet analysis is used in this study to avoid resonance.

The numerical model of five-story building is subjected to six different earthquakes in order to evaluate the performance of the proposed control system. Thus, nine performance indices are defined based on the displacements and accelerations at the base and floor levels. In addition, the responses of the building are compared with traditional fuzzy logic control and passive control with maximum voltage of MR damper.

The results show that the wavelet-based fuzzy logic control performs better compared with the traditional fuzzy logic controller in term of reducing the displacements and acceleration responses simultaneously, which highlights the advantage of using wavelet analysis in this study along with the damage detection techniques. The algorithm uses the wavelet analysis to process the earthquake signals within small time windows. Therefore, it provides a powerful tool to

avoid the resonance phenomenon, and consequently, it improves the overall performance of the system under different earthquakes. It is worth to mention that the limitation of the methods for the earthquakes with higher PGAs and PGVs, as well as the near- and far-field characteristics need to be investigated in future studies.

6. SEISMIC PROTECTION OF BUILDINGS USING SUPERELASTIC LEAD RUBBER BEARING (S-LRB) BASE-ISOLATORS AND MR DAMPERS UNDER NEAR-FIELD EARTHQUAKES

The main problem with the design of base-isolation systems is that the parameters do not always guarantee the minimum damage under any near and far-field earthquakes. In addition, base-isolation systems usually undergo nonlinear behavior and there is always a residual displacement after major a major earthquake [70-72]. In this study, super elastic effect of shape memory alloy (SMA) materials is used to recover the initial state of base-isolators [70-72]. In order to improve the performance of the systems and controllability of the structures, magnetorheological (MR) damper is used in parallel with SMA cables. Fuzzy logic control (FLC) is used to control the input voltage of MR damper.

6.1. SMA-based seismic isolation systems

Sliding bearings and laminated rubber bearings comprise the major types of base isolation systems. The former type of the isolation system mainly utilizes the static friction to provide resistance to motion under small earthquakes, and yields sliding to dissipate the input energy under strong earthquakes. While the later isolation system generally involves natural rubber bearing (NRB), lead-rubber bearing (LRB) and high damping rubber bearing (HDRB), which have been widely applied in both construction and retrofitting. The comparison of these two types of isolation devices are detailed in Table 6-1, based on the numerical simulations and experimental investigations [111]. Despite the popularity of these isolation devices, they are faced with inherent drawbacks of aging, excessive residual deformations, instability under large deformations, and difficulty of replacement after strong earthquake [70, 112].

Table 6-1. Comparisons of sliding isolation bearing and elastomeric bearing [111].

	Sliding bearings	Laminated rubber bearings
Advantages	a) Wide range adjusted to excitation frequencies; b) Confinement to torsional deformations.	a) Large vertical carrying capacity of laminated rubber isolation reinforced with steel plates; b) Extra energy dissipation with additional central lead metal core.
Drawbacks	a) Difficulty in construction due to the heavy weight and large size; b) No capacity of re-centering.	a) Sensitive to excitation frequency; b) Larger lateral displacement.

Thus, to overcome such defects and limitations of conventional isolation devices, smart materials in terms of shape memory alloys (SMAs) have been developed as an effective addition to be combined with those aforementioned isolation bearings to reduce the tremendous forces caused by earthquakes [70-73].

In this study a superelastic-LRB (S-LRB) base-isolation system is used on the basis of the previous study in the literature [70-72], which consists of two superelastic SMA device and a lead-rubber bearing device. The lead-rubber bearing device consists of layers of low damping rubber and steel that provides a sufficient rigidity and flexibility in the vertical and horizontal directions, respectively. The superelastic SMA device consists of NiTi SMA wires that are guided using frictionless wheels. Although the LRB device mainly dissipates the hysteretic energy, SMA device provides the restoring force with a relatively small capability of energy dissipation. Thus, combination of these two devices provides both advantages.

The nonlinear behavior of the lead-rubber bearing base isolator can be estimated using the bilinear model.

6.2. Magnetorheological dampers

In this section of the research, the MR damper is simulated based on the simple Bouc-Wen model that is illustrated earlier in Chapter 3.

6.3. Fuzzy inference system (FIS)

The flowchart of fuzzy logic model [70] is shown in Figure 6-1. The simulation parameters are described below.

6.3.1. Fuzzy model of the superplastic NiTi SMA wires

A Sugeno-type fuzzy inference system was developed and proposed by Ozbulut and Hurlebaus [70] to simulate the complex nonlinear dynamic behavior of superplastic NiTi SAM wires at different temperatures (ranging from 0-40 ℃), and different strain rates (ranging from 0.5 to 2 Hz). They used a large number of experimental data and neuro-fuzzy modeling (ANFIS) technique to establish the final FIS structure. Since the model considers the strain rate, it has advantages over the idealized models that are based on the strain-stress relationship.

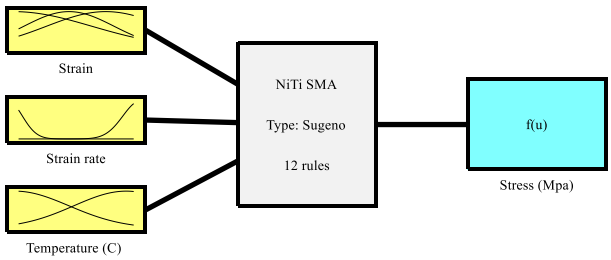

Figure 6-1. Fuzzy model of the superplastic NiTi SMA wires (replotted from [70]).

The inputs of the FIS model are the strain, strain rate, and temperature of the NiTi SMA wires, and the output is the stress in MPa. The membership functions for the three inputs are from the Gaussian type that is defined as:

$$f(x;\sigma,c) = e^{\frac{-(x_i-c)^2}{2\sigma^2}} \tag{6-1}$$

where x, c, and σ are the input variable and shape parameters, respectively. The parameters for the input membership functions and the coefficients for the Sugeno type output are given in Table 6-2. In addition, the total 12 rules are given in this table. More detailed information about the fuzzy model of the NiTi SMA is available from ref. [70].

Table 6-2. FIS model parameters for NiTi SMA [70].

Variable	Membership function (Type)	Parameters*	Range
Strain	In1MF1 (Gaussian)	[4.098, -0.2671]	
	In1MF2 (Gaussian)	[2.359, 2.632]	
	In1MF3 (Gaussian)	[3.104, 4.555]	
Strain rate	In2MF1 (Gaussian)	[6.835, -30.83]	
	In2MF2 (Gaussian)	[8.275, 32.29]	
Temperature (C)	In3MF1 (Gaussian)	[18.74, -1.23]	
	In3MF2 (Gaussian)	[18.22, 37.42]	
Stress (MPa)	Out1MF1 (Linear)	[-2518, -16.72, -23.16, -7815]	[-9.953 867.5]
	Out1MF2 (Linear)	[5765, -10.99, -17.74, 1.379e+04]	
	Out1MF3 (Linear)	[2155, 5.255, -17.9, 3258]	
	Out1MF4 (Linear)	[6861, -0.01061, -10.66, 1.475e+04]	
	Out1MF5 (Linear)	[-1286, 17.23, 102.8, 1793]	
	Out1MF6 (Linear)	[1706, 22.62, 50.57, -5852]	
	Out1MF7 (Linear)	[218.3, -4.417, 80.79, -4583]	
	Out1MF8 (Linear)	[1703, -9.897, 33.29, -8792]	
	Out1MF9 (Linear)	[-1408, 4.27, -80.43, 1.993e+04]	
	Out1MF10 (Linear)	[2530, -4.792, -26.04, -3.155e+04]	
	Out1MF11 (Linear)	[-122.6, -1.782, -62.43, -2363]	
	Out1MF12 (Linear)	[1942, 4.03, -15.73, -2.97e+04]	

* [σ, c] for the input Gaussian membership functions, and [x_0, x_1, …, x_n] for the output membership function for mapping the inputs to the outputs. Rules of the FIS model is defined in the form of vectors. For example, [1, 1, 2; 2] means that if In2MF1 and In2MF1 and In3MF2; then, Out1MF1. The total 12 rules are [1,1,1;1], [1,1,2;2], [1,2,1;3], [1,2,2;4], [1,3,1;5], [1,3,2;6], [2,1,1;7], [2,1,2;8], [2,2,1;9], [2,2,2;10], [2,3,1;11], and [2,3,2;12].

6.3.2. Fuzzy logic control

In this study, a fuzzy logic control [26, 81, 96, 110] is used to manage the input voltage of the MR damper. Details of the FLC as well as the membership functions could be found in the literature [83, 113], and only the parameters of the designed FLC is presented in this section. For the current FLC, seven Gaussian membership functions are used to define the input variables,

displacement and velocity of the base level and five Gaussian membership functions are used to determine the output variable, voltage.

6.4. Numerical example

6.4.1. Dynamic properties of the five-story base-isolated building model

A five-story base-isolated building model, based on the studies carries out by Ozbulut et al. and Amini et al. [21, 26], is selected for the numerical simulation (Figure 6-2). Mass and stiffness of each story of the superstructure is given in Table 6-3, and the initial design of the LRB base-isolator properties are given in Table 6-4. The design parameters are optimized for the LRB-SMA device. The damping matrix for the model is obtained using Rayleigh method considering an inherent 5% damping for the first two modes of vibration [99].

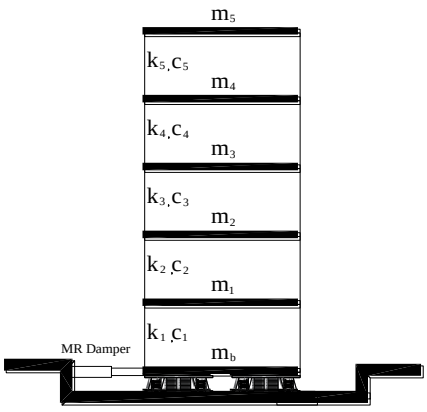

Figure 6-2. Five-story base-isolated building with MR damper and NiTi SMA [26].

Table 6-3. Mass and stiffness of five-story based-isolated building model [26].

Story	m (kg)	k (kN/m)
5th	5897	19059
4th	5897	24954
3rd	5897	28621
2nd	5897	29093
1st	5897	33732

Table 6-4. Dynamic properties of LRB devices [26].

LRB type	m (kg)	c (kN/m/s)	k_e (kN/m)	k_p (kN/m)	Q (kN)
LRB-low	6800	7.54	1389	231.5	13890
LRB-high	6800	7.54	2315	231.5	47921

6.4.2. MR damper parameters

In this study, the simple Bouc-Wen model of MR damper is used as described before.

6.4.3. Earthquake records

In order to cover a range of different characteristics of near-field earthquakes including frequency content, duration, peak ground acceleration, and peak ground velocities, 45 ground motions that are recorded within 30 km of the epicenters.

Table 6-5. Characteristics of the selected near-field ground motions.

No.	Earthquake	Year	Station	Comp.	Mw	Dist. (km)	Mechanism	PGA (g)	PGV (cm/s)	PGD (cm)
1	San fernando	1971	Pacoima Dam-Left Abutment	164	6.61	1.81	Reverse	1.22	114.47	39.02
2	San fernando	1971	Pacoima Dam-Left Abutment	254	6.61	1.81	Reverse	1.24	57.28	12.80
3	Gazli	1976	Karakyr	000	6.8	5.46	Reverse	0.70	66.22	27.34
4	Gazli	1976	Karakyr	090	6.8	5.46	Reverse	0.86	67.65	20.72
5	Coyote lake	1979	Gilroy Array #6	230	5.74	3.11	Strike slip	0.42	44.35	12.44
6	Coyote lake	1979	Gilroy Array #6	320	5.74	3.11	Strike slip	0.32	25.40	4.38
7	Coalinga	1983	Pleasant Valley P.P. - bldg	045	6.36	8.41	Reverse	0.30	39.40	6.38
8	Coalinga	1983	Pleasant Valley P.P. - bldg	135	6.36	8.41	Reverse	0.27	21.54	3.02
9	Morgan hill	1984	Anderson dam(Downstream)	250	6.19	3.26	Strike slip	0.42	25.41	4.44
10	Morgan hill	1984	Anderson dam(Downstream)	340	6.19	3.26	Strike slip	0.29	27.80	6.44
11	Nahanni, Canada	1985	Site1	010	6.76	9.6	Reverse	1.11	43.93	6.81
12	Nahanni, Canada	1985	Site1	280	6.76	9.6	Reverse	1.20	40.63	10.20
13	N. Palm Springs	1986	North Palm Springs	210	6.06	4.04	Reverse Oblique	0.69	65.99	16.17
14	N. Palm Springs	1986	North Palm Springs	300	6.06	4.04	Reverse Oblique	0.67	27.94	4.91
15	Whittier Narrows-01	1987	Santa Fe Springs - E.Joslin	048	5.99	18.49	Reverse Oblique	0.47	34.39	6.50
16	Whittier Narrows-01	1987	Santa Fe Springs - E.Joslin	318	5.99	18.49	Reverse Oblique	0.46	31.57	4.55
17	Superstition Hills-02	1987	Parachute Test Site	225	6.54	0.95	Strike slip	0.43	134.29	46.18
18	Superstition Hills-02	1987	Parachute Test Site	315	6.54	0.95	Strike slip	0.38	53.06	17.82
19	Loma Prieta	1989	Gilroy Array #2	000	6.93	11.07	Reverse Oblique	0.37	34.76	9.51
20	Loma Prieta	1989	Gilroy Array #2	090	6.93	11.07	Reverse Oblique	0.32	40.37	18.46
21	Sierra Madre	1991	Cogswell Dam-Right Abutment	065	5.61	22	Reverse	0.26	9.55	0.95
22	Sierra Madre	1991	Cogswell Dam-Right Abutment	155	5.61	22	Reverse	0.30	14.92	2.08
23	Erzican, Turkey	1992	Erzican	EW	6.69	4.38	Strike slip	0.50	78.16	28.04
24	Erzican, Turkey	1992	Erzican	NS	6.69	4.38	Strike slip	0.39	107.14	31.99
25	Northridge-01	1994	LA dam	064	6.69	5.92	Reverse	0.43	74.84	19.06
26	Northridge-01	1994	LA dam	334	6.69	5.92	Reverse	0.32	47.38	24.57
27	Kobe	1995	KJMA	000	6.9	0.96	Strike slip	0.83	91.11	21.11
28	Kobe	1995	KJMA	090	6.9	0.96	Strike slip	0.63	76.11	18.33
29	"Kocaeli_ Turkey"	1999	Izmit	090	7.51	7.21	Strike slip	0.23	38.29	24.29
30	"Kocaeli_ Turkey"	1999	Izmit	180	7.51	7.21	Strike slip	0.17	22.33	11.84

Source: http://ngawest2.berkeley.edu/

Thirty near-field earthquake records are selected in this research, and their characteristics are given in Table 6-5. Figure 6-3 shows the response spectral accelerations for the selected

ground motions before and after matching with the target design spectrum. The target spectrum is defined for an area in southern California for a soil class of D, and SeismoMatch program is used for scaling the records.

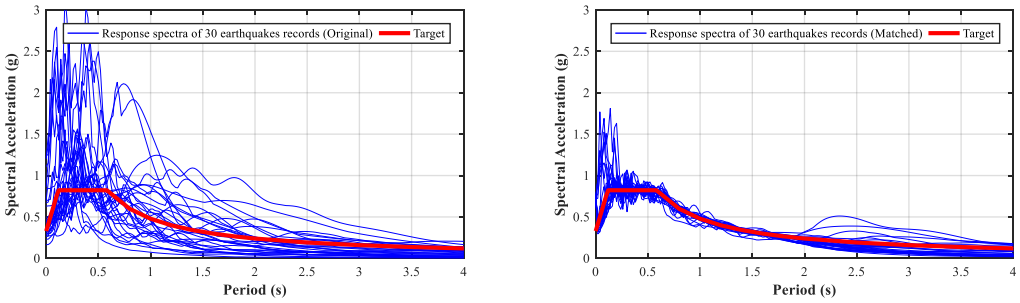

Figure 6-3. Spectral responses for the selected earthquakes before and after matching using SeismoMatch.

6.4.4. Results and discussion

6.4.4.1. Maximum responses

Figure 6-4 and Figure 6-5 show the effect of the SMA cables that are used in the base-isolation system. Both figures clearly show that effectiveness of the SMA cables, regardless of the LRB type. The maximum reduction is achieved using MR damper with passive-on control method.

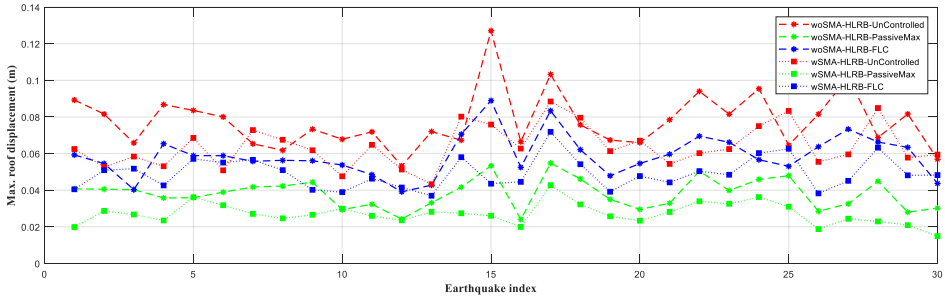

Figure 6-4. Effect of SMA using different control methods (L-LRB).

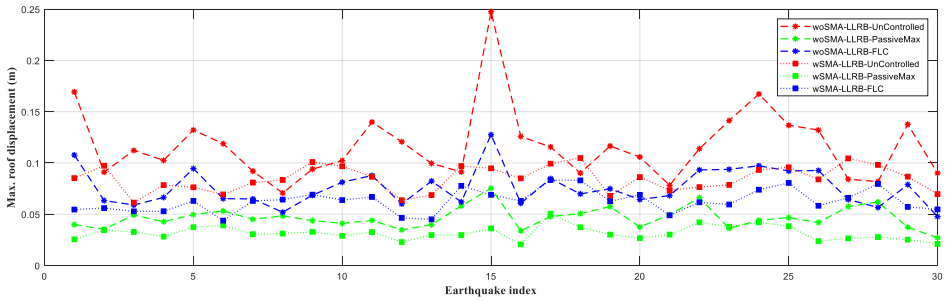

Figure 6-5. Effect of SMA using different control methods (H-LRB).

6.4.4.2. Time-history of responses

Figure 6-6 shows the time-history response of the base-isolated building for the three control cases: uncontrolled, passive-on, and fuzzy logic control. As it can be clearly seen from the time history response plot for all the records, using superelastic materials in the base-isolation the minimum residual displacement is achieved for any control methods. Thus, it using the self-centering materials such as SMAs can significantly improve the performance of base-isolated buildings along with the application of MT dampers.

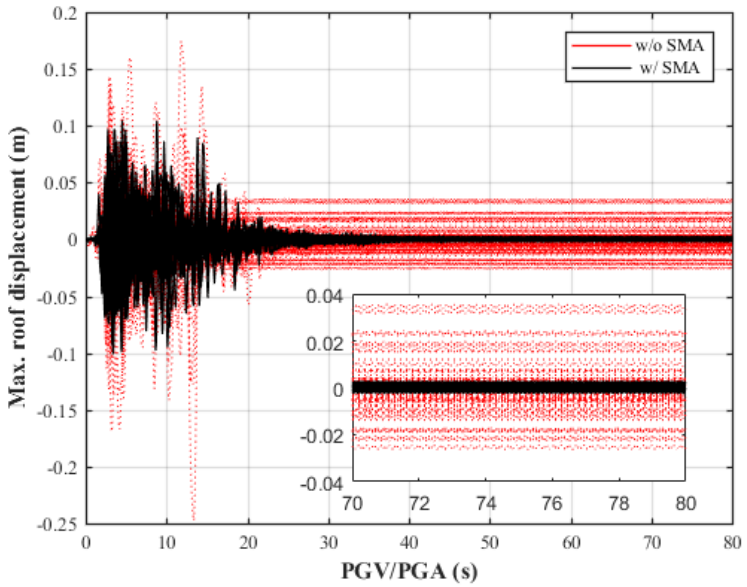

Figure 6-6. Time-history response of the building under all the earthquake records.

Further investigations are conducted in order to see the influence of the PGV/PGA ratio on the maximum roof displacement. Figure 6-7 shows the response of the building versus the PGV/PGA ratio. Clearly, using MR damper with SMA materials significantly reduces the peak displacement.

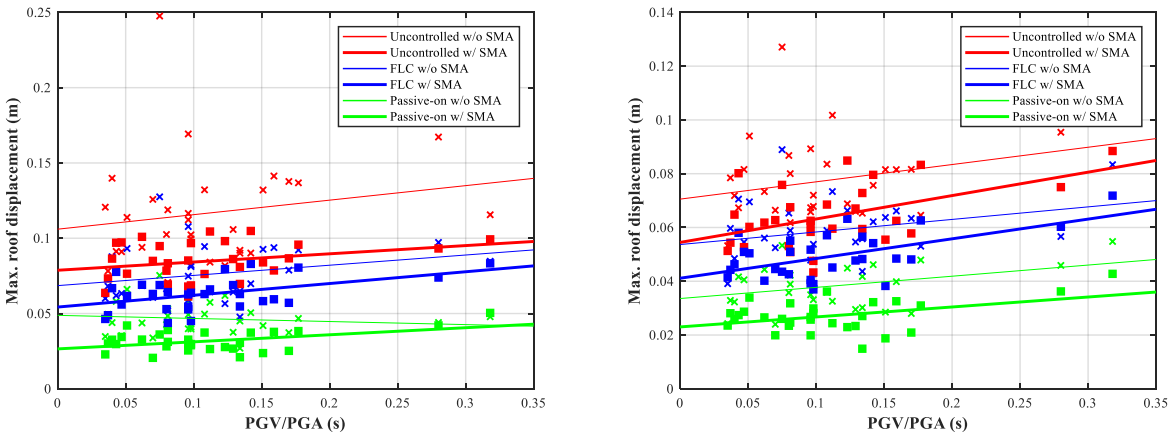

Figure 6-7. Maximum roof displacement vs. PGV/PGA ratio using L-LRB (left) and H-LRB (right).

6.5. Summary

In this section of the thesis, the application of SMA materials with MR damper is investigated for the base-isolated structures under near-field earthquakes. Fuzzy logic control and passive-on methods are used to evaluate the effectiveness of the method. The results show that the superelastic effect of SMA can help to regain the original displacement of the isolator and minimum residual displacement is achieved.

7. OPTIMAL DESIGN OF ACTIVE TUNED MASS DAMPERS FOR MITIGATING TRANSLATIONAL–TORSIONAL MOTION OF IRREGULAR BUILDINGS

The active tuned mass dampers (ATMDs) are accepted as effective energy dissipating devices to effectively reduce structural dynamic response when subjected to seismic loads. The conventional design of these devices, however, may not be applicable to high-rise buildings with irregularity in plan and elevation, where significant torsional motions could be dominant during a strong earthquake. Some attempts [128-132] have been made to address the impacts of structural irregularity. Xu and Igusa [128] reported their study by using multiple TMDs for torsional resistance. One big challenge is how to effectively tune multiple objectives, similar to other observation [129]. Lin et al. [130] investigated the bi-directional coupled TMDs to account for potential vibration along two horizontal directions as well as rotation effects. Their results demonstrated that the design concept is effective for bi-directional effects under earthquake. Very recently, He et al. [131] attempted to develop TMDs with poles and torsional pendulums for reduction of vibration-induced torsion. Bases on these studies in the literature, this study is to explore active TMD for reducing the torsional motion as well as resisting the lateral translational displacements. Similar to design of pendulums, three actuators are used to apply the control forces to the twin-TMD system in two directions, while the optimal control forces were determined using linear quadratic regulator (LQR) algorithm. In addition, instead of using two independent mass dampers in two directions, a single damper system was used to minimize the displacements and rotation simultaneously. To demonstrate the performance of the system, the final design was applied to an irregular ten-story building subjected to near- and far-field earthquakes. The results indicate that the design approach is more cost effective as compared to

the design with independent pairs of dampers in two directions. Further, the system exhibits higher reliability under different ground accelerations in two directions than conventional ones.

7.1. Optimal design of TTMD

7.1.1. Configuration of TTMD system

Similar to design of pendulums [131, 132], as shown in Figure 7-1, the twin tuned mass damper (TTMD) system includes two masses, M_1 and M_2, that are connected to each other with a rigid bar; while the bar is restrained in the x-direction at midpoint, it can move in the y-direction and rotate about the midpoint O. Three springs and dashpots are used to stabilize the system. For the active-TTMD system, three actuators apply the controlling forces in two directions as well as the moment for suppressing the translational-torsional vibration. For simplicity, properties of each twin dampers are selected identical, and the optimal values were obtained through an optimization algorithm. The length of the connecting rigid bar is assumed to be 10 m.

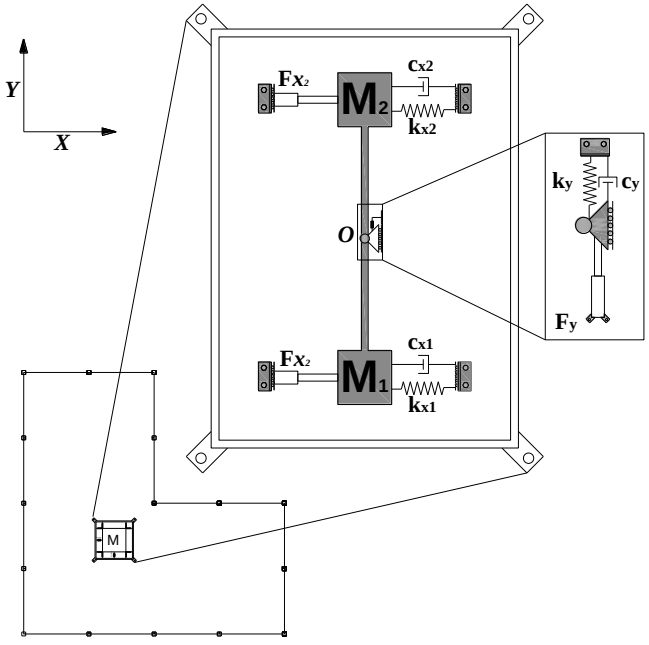

Figure 7-1. Schematic diagram of plan view of smart tuned mass damper installed on the roof.

7.1.2. Particle swarm optimization (PSO)

Since the optimization problem is continuous in this study, the particle swarm optimization (PSO) [80, 114] is used for optimal design of TTMD parameters. The procedure is based on PSO algorithm that takes the parameters of TTMDs as the design variables and determines them to meet the objectives. The design objectives can be varied; in this study, in order to maintain the integrity of the building, optimization problem can be expressed as [114]:

Find: $M_{TMD}, C_{1,2,3_{TMD}}, K_{1,2,3_{TMD}}$

Minimize: $X_{max} = max\left|x_{roof}(t)\right|$

Subjected to: $0 < M < M_{max}; 0 < K_i < K_{i,max};\ 0 < C < C_{i,max};\ i = 1,2,3$

where M_{TMD} is the total mass of the system; C_i and K_i are the damping and stiffness of each dashpot and spring in both directions, respectively. A brief explanation of PSO algorithm has been presented in the following section.

Particle swarm optimization (PSO) was introduced by Kennedy in 1995 [114]. In PSO, the information about the design space is shared by all the members of the swarm, starting with a set of randomly generated solutions and ending with a global optimum solution over a number of iterations. PSO algorithm is inspired by the behavior of swarms such as schools of fish, flocks of birds that are able to adapt to the changes in their environment and find food or avoid predators by sharing information. Figure 7-2 shows the algorithm for PSO, which can be summarized in three main steps: generating particles positions, x_i, and velocities, v_i, velocity update, and finally, position update. The initial swarm can be generated randomly, using the upper and lower bounds of the design variables. Then with each iteration, the position of partials can be updated as:

$$\mathbf{x}_{i+1}^{j} = \mathbf{x}_{i}^{j} + \mathbf{v}_{i+1}^{j}\Delta t \tag{7-1}$$

where $\mathbf{x}_{i+1}^{j}$, and $\mathbf{v}_{i+1}^{j}$ are the position and velocity of j^{th} particle in $(i+1)^{th}$ iteration, respectively. Velocity of particle in PSO algorithm is updated using the Equation (7-2). In this equation, c_1, and c_2 are the inertia factor, self-confidence factor, and swarm confidence factor, respectively. The flowchart for the PSO algorithm has been illustrated in Figure 7-2. In this figure, p_{Best} and g_{Best} are the particle best position and global best position, respectively.

$$\mathbf{v}_{i+1}^{j} = w\mathbf{v}_{i}^{j} + c_1 rand\left(\frac{\left(\mathbf{p}^{j} - \mathbf{x}_{i}^{j}\right)}{\Delta t}\right) + c_2 rand\left(\frac{\left(\mathbf{p}_{i}^{g} - \mathbf{x}_{i}^{j}\right)}{\Delta t}\right) \tag{7-2}$$

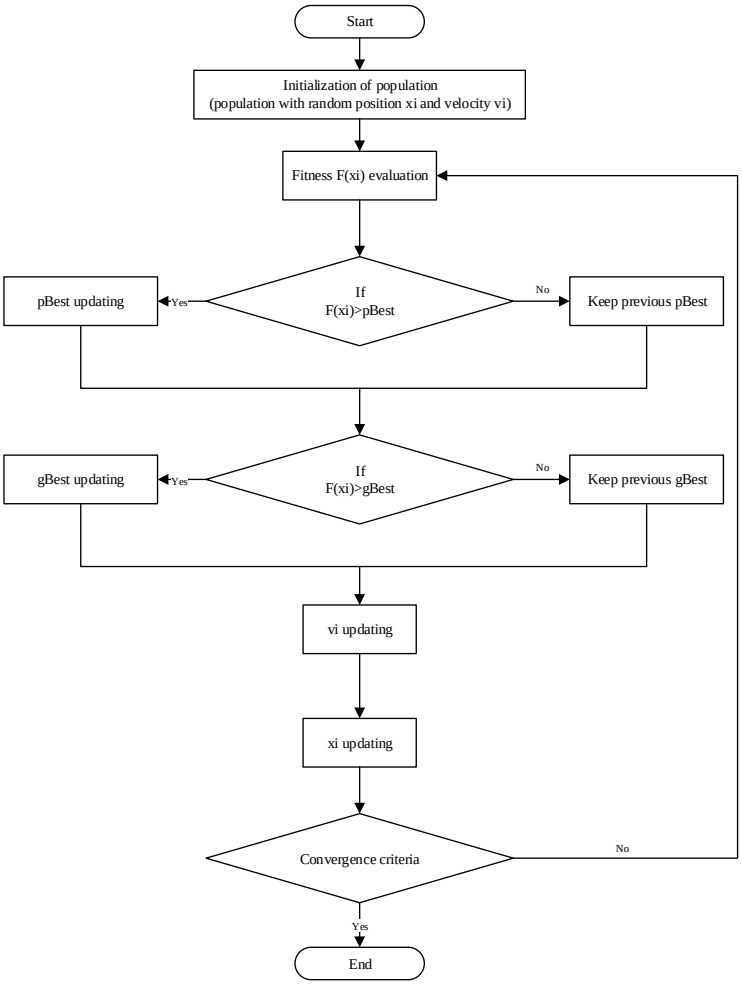

Figure 7-2. Flowchart of the PSO algorithm.

7.2. Vibration control using active and passive TTMDs

7.2.1. Governing equations of the controlled system

The governing motion equations of controlled *n*DOF system can be condensed and described as [12], under seismic ground acceleration load, $\ddot{x}$:

$$[M]\{\ddot{x}(t)\} + [C]\{\dot{x}(t)\} + [K]\{x(t)\} = [\gamma]\{u(t)\} + \{\delta\}\ddot{x}_g(t) \tag{7-3}$$

where, M, C and K are (3×n×3×n) matrices of mass, damping and stiffness, and x, ẋ, ẍ are the (n×1) displacement, velocity and acceleration vectors, respectively. $\{u(t)\}$ is the control force vector, and $\{\delta\}$ is the coefficient vector for earthquake ground acceleration $\ddot{x}_g(t)$. $[\gamma]$ is the controller location matrix that also represent the influence of each controller on the DOFs, and takes the following form for a three dimensional building controlled by active TTMD;

$$[\gamma] = \begin{bmatrix} \mathbf{0} & \mathbf{0} & & & \\ & \mathbf{0} & \mathbf{0} & & \\ & & \mathbf{0} & \ddots & \\ & & & \ddots & -\boldsymbol{D} \\ & & & & \boldsymbol{D} \end{bmatrix} \tag{7-4}$$

For the passive controlled system, the *D* matrix is equal to zero, because the TTMD system is considered as an additional story level in simulation. For the active-TTMD system, three control forces are applied using the three actuators, two in x-direction and one in y-direction; therefore, the other elements of $[\gamma]$ are zero for the lower stories. In this matrix, 0 is (3×3) matrix of zeros and D is defined as:

$$\boldsymbol{D} = \begin{bmatrix} 1 & 1 & 0 \\ 0 & 0 & 1 \\ \frac{L}{2} & -\frac{L}{2} & 0 \end{bmatrix} \tag{7-5}$$

In other words, *D* determines the coefficient of the three input control forces (columns) on the three DOFs (rows). The mass matrix can be assembled as:

$$M = \begin{bmatrix} \boldsymbol{m}_1^* & \mathbf{0} & \mathbf{0} \\ \mathbf{0} & \ddots & \mathbf{0} \\ \mathbf{0} & \mathbf{0} & \boldsymbol{m}_n^* \end{bmatrix} \tag{7-6}$$

where 0 is (3×3)-dimensional zero matrix and can be obtained as follows:

$$\boldsymbol{m_n^*} = \begin{bmatrix} m_n & 0 & 0 \\ 0 & m_n & 0 \\ 0 & 0 & I_{z,n} \end{bmatrix} \tag{7-7}$$

where m_n is the total mass of nth story level, and $I_{z,n}$ is mass moment of inertia about z-direction, defined as [115]:

$$I_z = \sum_{j=1}^{j_m} \left[\frac{m_j}{12}(a^2 + b^2) + m_j \left[\left(x_{m,j} - \bar{X}_m\right)^2 + \left(y_{m,j} - \bar{Y}_m\right)^2 \right] \right] \tag{7-8}$$

where, $m_{x,j}$, and $m_{y,j}$ are the mass of jth slab in x and y directions, with coordinate of $x_{m,j}$ and $y_{m,j}$, respectively. $(\bar{X}_m, \bar{Y}_m)$ is the coordinate of center of mass of the diaphragm, and a and b are the dimension of each slab panel. In order to assemble the total stiffness matrix, stiffness of each story, $[\boldsymbol{k}_n]$, need to be determined in three-dimension [115].

$$[\boldsymbol{k}_n] = \begin{bmatrix} k_{xx} & 0 & k_{x\theta} \\ 0 & k_{yy} & k_{y\theta} \\ k_{\theta x} & k_{\theta y} & k_{\theta\theta} \end{bmatrix} \tag{7-9}$$

The elements of $\boldsymbol{k}_n$ can be found in detail [115]:

$$k_{xx} = \sum_{j=1}^{nk} k_{x,j}, \quad k_{yy} = \sum_{j=1}^{nk} k_{y,j} \tag{7-10}$$

$$k_{x\theta} = k_{\theta x} = \sum_{j=1}^{nk} k_{x,j}(\bar{Y}_k - y_{k,j}) \tag{7-11}$$

$$k_{y\theta} = k_{\theta y} = \sum_{j=1}^{nk} k_{y,j}(\bar{X}_k - x_{k,j}) \tag{7-12}$$

$$k_{\theta\theta} = \sum_{j=1}^{j_k} \left(k_{x,j}\left(\bar{Y} - y_{k,j}\right)^2 + k_{y,j}\left(\bar{X} - x_{k,j}\right)^2 \right) \tag{7-13}$$

where, $k_{x,j}$, and $k_{y,j}$ are the stiffness of j^{th} lateral resisting members in x and y directions, with coordinate of $x_{k,j}$ and $y_{k,j}$, respectively. The center of stiffness is located at $(\bar{X}_k, \bar{Y}_k)$. Therefore, the stiffness matrix can be assembled as [115]:

$$K_s = \begin{bmatrix} k_1 + k_2 & -k2 & 0 & 0 \\ -k2 & k2 + k_3 & -k_3 & 0 \\ 0 & 0 & .. & -k_n \\ 0 & 0 & -k_n & k_n \end{bmatrix} \quad (7\text{-}14)$$

Damping matrix of the system, C_s, is determined using the Rayleigh method based on the mass and stiffness matrices [99], and an inherent damping of 5% is assumed for the first and fourth modes of vibration. The equation of motion can be solved by rewriting it in state-space form as [12]:

$$\{\dot{Z}(t)\} = [A]\{Z(t)\} + [B_u]\{u(t)\} + \{B_r\}\ddot{x}_g(t) \quad (7\text{-}15)$$

where

$$\{Z(t)\} = \begin{Bmatrix} x(t) \\ \dot{x}(t) \end{Bmatrix} \quad (7\text{-}16)$$

$$A = \begin{bmatrix} [0] & I \\ -M^{-1}K & -M^{-1}C \end{bmatrix}; \{B_u\} = \begin{bmatrix} [0] \\ M^{-1}[\gamma] \end{bmatrix}; \quad \{B_r\} = \begin{bmatrix} \{0\} \\ [M]^{-1}\{\delta\} \end{bmatrix} \quad (7\text{-}17)$$

The solution procedure for the state-space equation is available is literature [12].

7.2.2. Numerical example: ten-story irregular steel moment frame

A ten-story irregular building frame was selected in the literature [2] as the example case. The 3D and plan views are shown in Figure 7-3. Following assumption has been made in order to idealize the numerical model of the example: all the column members have the same symmetric cross section and length; each floor acts as a rigid diaphragm and all the columns are fixed at the ends. For this model, all the columns are assumed to have the same stiffness in both directions, and each floor is considered as a rigid diaphragm. Using these assumptions, the stiffness of the i^{th} column in both directions, with the height of h_i and the moment of inertia of I_i, can be estimated as: $k_i = \frac{12EI_i}{h_i^3}$, where E is the Young's modulus of the steel. The dynamic properties of the building are given in Table 7-1.

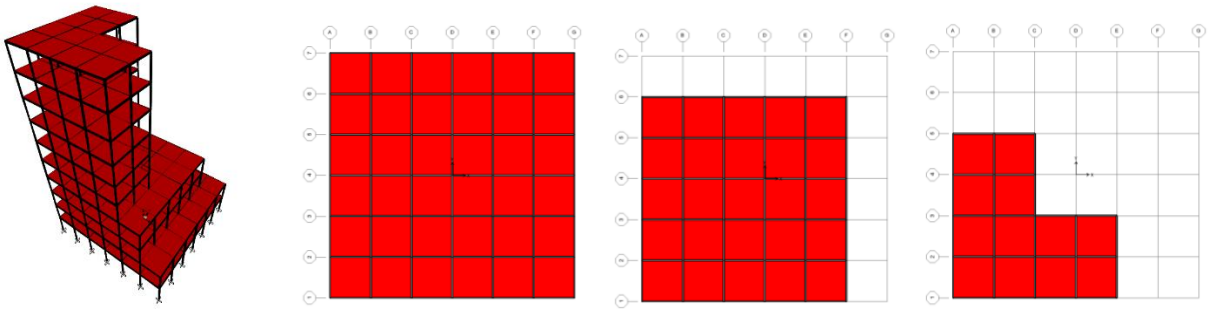

(a) 3D view (b) 1st-2nd (c) 3rd-4th (c) 5th-10th

Figure 7-3. The 3D and plan views of the building model.

Table 7-1. Dynamic properties of the 10-story building model.

Story	Mass (kg)	$\sum K_x, \sum K_y$ (kN/m)	Eccentricity
1	1552500	23820	(2.81,2.81)
2	1552500	23820	(2.81,2.81)
3	858750	18360	(3,3)
4	858750	18360	(3,3)
5	495000	12060	(1.59, 1.59)
6	495000	12060	(1.59, 1.59)
7	495000	12060	(1.59, 1.59)
8	495000	12060	(1.59, 1.59)
9	495000	12060	(1.59, 1.59)
10	495000	12060	(1.59, 1.59)
Sum:	7792500		

For an irregular building, higher modes of vibration may participate as well as the primary first modes. Since the model is not neither symmetric nor has the same center of mass for all the stories, the modal analysis of the system was carried out in order to investigated the mode shapes and contribution of each mode. Modal analysis results are given in Figure 7-4. This supports this proposal that for such buildings: (1) the earthquake ground should be applied in both directions simultaneously, and (2) dimensions, location and other properties of a TMD can have considerable effect of the overall performance of the system. In this study, influence of the

location of the TMD was not investigated; thus, it is assumed that it is located at the center of mass of roof level.

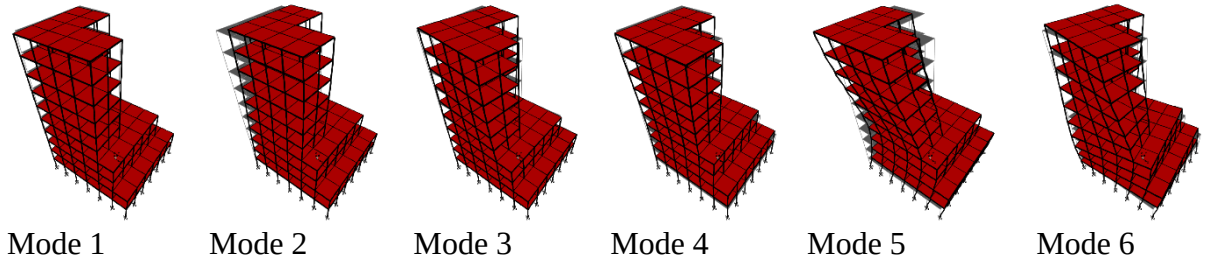

Figure 7-4. Mode shapes of the building.

7.2.3. Ground excitation

The 10-story building is subjected to random excitation that is obtained by filtering a white noise through a linear filter—known as Kanai-Tajimi filter—which represents the surface ground. While the TTMD parameters are designed for the white noise excitation (Figure 7-5), three historic earthquake records are selected in this research to evaluate the performance of the active controlled system with actuators under different ground excitations. The characteristics of the selected earthquakes are given in Table 7-2.

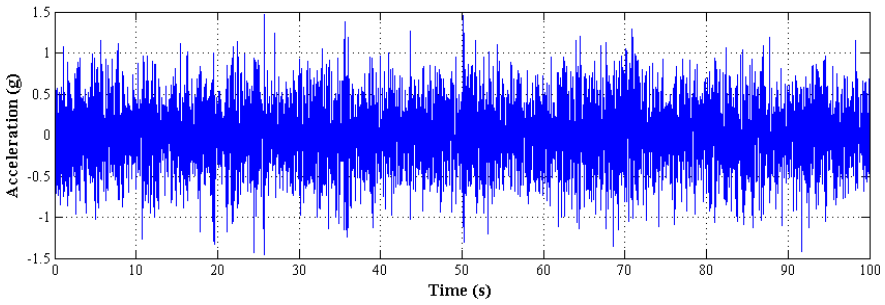

Figure 7-5. Filtered white noise excitation.

Table 7-2. Characteristics of the earthquake records.

Earthquake	Station & Direction	Magnitude (Mw)	PGA (g)	PGV (cm/s)
1940 El Centro	El Centro Array #9 270°	7.2	0.21	30.2
	El Centro Array #9 180°	7.2	0.28	31.0
1994 Northridge	Sylmar - Olive View Med FF 360°	6.7	0.84	129.6
	Sylmar - Olive View Med FF 090°	6.7	0.61	77.53
1995 Kobe	H1170546.KOB 090°	7.2	0.63	76.6
	H1170546.KOB 000°	7.2	0.83	91.13

Source: http://ngawest2.berkeley.edu/

7.3. Results and discussion

7.3.1. Optimization results

The optimum parameters for the typical TMD systems, for minimizing the roof displacement, can be obtained using the equations given in Table 7-3. The optimum design parameters of the traditional TMD system for different mass ratios can be obtained by using the equations in this table, which are basically developed for unidirectional earthquake excitation without considering the eccentricities. For three mass ratios of 1%, 3%, and 5%, the mass, damping, and stiffness of the TMD are given in Table 7-4.

Table 7-3. The optimal parameters for a TMD attached to a MDOF system [44].

Minimizing item	Frequency ratio	Damping ratio
Displacement	$\frac{1}{(1+\mu)^2}$	$\frac{3\mu}{8(1+\mu)^3}$

Table 7-4. Optimum parameters of the TMD damper in one-direction.

Criterion	μ_d	C_d	M_d (kg)	K_d (N/m)
Displacement	1%	7763	77925	53119
	3%	37662	233775	147336
	5%	75761	389625	227379

For simplicity and for having more feasible results, the mass of each TMDs are selected to be the same, the connecting rigid bar length are known and equal to 10 m. Figure 7-6 shows the number of PSO algorithm iteration vs. the best cost which is the displacement of the roof level in this study. It can be seen that the peak displacement has been reduced considerably by optimizing the design variables using PSO algorithm. Since each building has its own configurations, it is preferable to find the optimum parameters using such a powerful algorithm like PSO. The optimization process was repeated for three different mass rations: μ= 1%, μ= 2%, and μ= 5%.

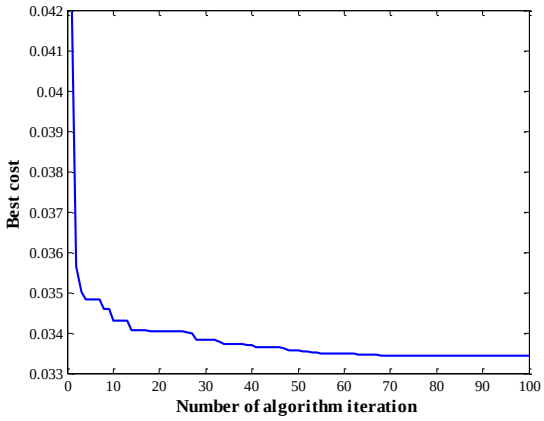

Figure 7-6. The best design history of the controlled 10-story steel frame with TTMD using PSO algorithm (μ=0.05).

7.4. Performance of the designed TTMD and ATTMD under historic earthquakes

While the TTMD parameters are designed using the white noise excitation, three historic earthquake records are selected in this research to evaluate the performance of the TTMD and ATTMD control systems under different ground excitations. The characteristics of the selected earthquakes are given in Table 7-2.

The torsional motion of the building is considered in the proposed control system; for the proposed ATTMD, the actuators generate a moment in addition to the forces in two directions. The moment counteracts the torsional motion; therefore, the overall displacements in both

directions, particularly for those columns in the corners, are reduced. Figure 7-7 shows the maximum displacement response of the building at the roof level—the corner columns— as well as the roof rotation using the three control systems, TMD, TTMD, and ATTMD. It is evident that by using the proposed design approach for TTMD system, both translational and torsional responses of the irregular building is reduced significantly compared to the traditional TMD system with the same mass ratios. In addition, the active form of the TTMD system (ATTMD) considerably reduces the response of the building during the excitation time. For example, from the displacement responses, by using the ATTMD control system there is no noticeable displacement after 50th second of the ground excitations. The maximum responses for each scenario are given in Table 7-5. In this table, $x_{\max}$ and θ_{roof} are the maximum displacement and rotation at the roof level, respectively.

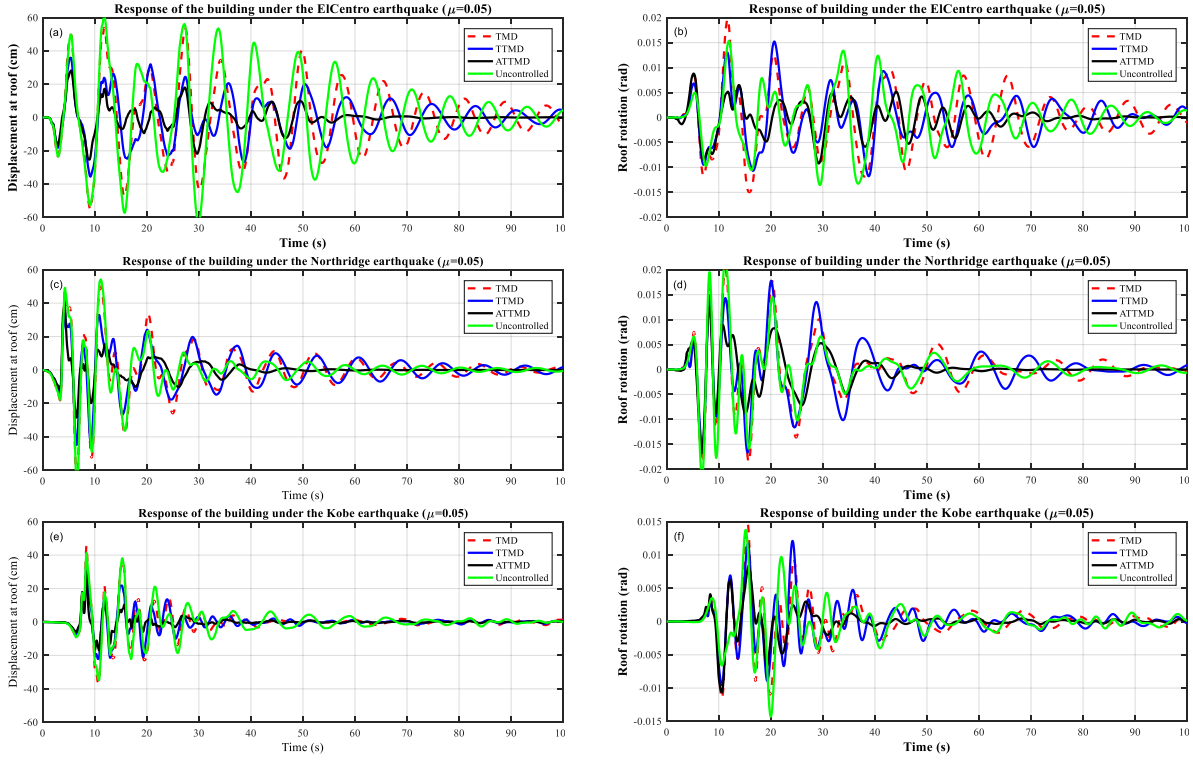

Figure 7-7. Displacement and rotation responses at roof level under the El Centro, Northridge, and Kobe earthquakes.

Table 7-5. Maximum responses of the uncontrolled building.

μ	Earthquake	Response	Uncontrolled	TMD	TTMD	ATTMD
1%	El Centro	$x_{\max}$	69.4 cm	-7%	-32%	-65%
		θ_{roof}	0.0210 rad	-1%	-25%	-44%
	Northridge	$x_{\max}$	72.3 cm	-5%	-30%	-45%
		θ_{roof}	0.0204 rad	-1%	-25%	-11%
	Kobe	$x_{\max}$	42.4 cm	+7%	-16%	-23%
		θ_{roof}	0.0145 rad	+1%	-19%	-26%
3%	El Centro	$x_{\max}$	69.4 cm	-16%	-44%	-60%
		θ_{roof}	0.0210 rad	-4%	-33%	-48%
	Northridge	$x_{\max}$	72.3 cm	-7%	-30%	-44%
		θ_{roof}	0.0204 rad	-1%	-25%	-13%
	Kobe	$x_{\max}$	42.4 cm	+7%	-16%	-26%
		θ_{roof}	0.0145 rad	+0%	-20%	-26%
5%	El Centro	$x_{\max}$	69.4 cm	-21%	-48%	-59%
		θ_{roof}	0.0210 rad	-6%	-40%	-56%
	Northridge	$x_{\max}$	72.3 cm	-8%	-38%	-53%
		θ_{roof}	0.0204 rad	-1%	-28%	-31%
	Kobe	$x_{\max}$	42.4 cm	+7%	-19%	-25%
		θ_{roof}	0.0145 rad	+1%	-31%	-37%

From Table 7-5, it can be seen that the traditional optimal design does not guarantee the maximum reduction of response in the irregular 10-story building. For example, by using the TMD system with 5% mass ratio, the maximum reduction in the displacement response obtained under the El Centro earthquake (21%), however, the same design increases the displacement and the rotation at roof level by 7% and 1%, respectively. On the other hand, the proposed TTMD system offers significant response reduction for all the mass ratios and under all three earthquake records. The maximum response reduction is for the TTMD design with 5% mass ratio under El Centro earthquake by 48%. Although for the building controlled by TMD, greater mass ratios result in more reduction, for the active-TTMD, the maximum reduction in the response is

achieved using the least mass ratio, μ=1%. Differences between the reduction percentages suggest that it is more appropriate to optimize the design case-by-case and separately, and avoid using set of equations for all configurations. Particle swarm optimization (PSO) algorithm is a powerful tool in finding the optimal design parameters of the proposed TTMD for buildings with irregularities in plan and elevation.

7.5. Summary

This study explores active tuned mass dampers for irregular high-rise buildings. The optimal parameters of the twin tuned mass damper systems are obtained through the particle swarm optimization (PSO) algorithm using a filtered white noise as the ground acceleration. The performance of the proposed system is evaluated for a 10-story irregular building under three historic earthquakes that are applied bi-directionally to the system. The results confirm that, despite the traditionally designed TMDs, the TTMD is more effective in reducing the translational-torsional motion of irregular structures. In addition, the active-TTMD control system is also investigated in this study, which significantly decreases the responses by using the LQR for determining the optimal control forces. The results of this study may lead to introduce new design criteria for designing of tuned mass damper systems for irregular buildings.

8. VIBRATION CONTROL OF 3D IRREGULAR HIGH-RISE BUILDINGS CONSIDERING SOIL-STRUCTURE INTERACTION USING MR DAMPERS

Response of irregular structures are highly dependent on the restraints provided at the base level and the dynamic properties of soils. Literature [77, 115, 132, 133] demonstrates that soil-structure interaction (SSI) effects can influence structural performance. Lin et al. [132] discussed the impacts of inclusion of SSI effects to seismic response of active-tendon controlled one-story irregular building. Farshidianfar and Soheili [133] carried out a research on passive vibration control of regular multistory buildings considering SSI effects. Nazarimofrad and Zahrai [115] further investigated the SSI effects on multi-story irregular buildings strengthened by active tendons. Based on the study by Nazarimofrad and Zahrai [115], seismic performance of irregular high-rise buildings strengthened with a semi-active controller using LQR and MR dampers is investigated in this study, where SSI effects are included. The multiple degree of freedom system model equation of motion is solved considering SSI forces that are modeled using springs and dashpots representing swaying, torsional and rocking motions. Numerical example of uncontrolled 3D irregular ten-story building with two different soil parameters is investigated under seven near-field earthquakes. In order to optimally control the vibration of the building, a semi-active controller using LQR and MR dampers is designed and compared with other control schemes including passive-on, passive-off and active controllers. The influence of dampers location as well as the maximum command voltage on the control performance is also examined. The results demonstrated that performance of buildings is more sensitive for soft soils compared to dense soils, while the use of the semi-active controller significantly reduced the inter-story drifts as well as the roof twist in both cases. In addition, using pairs of MR dampers with proper distance from the center of stiffness of the floor enable the more reductions in

torsional motion of a building, thereby reducing potential damages to the outer columns due to large inter-story drifts.

8.1. Controlled structure with SSI effects

8.1.1. Governing equations of dynamic structure with controller

Figure 8-1(a) shows an overview of a typical high-irregular tall building, while Figure 8-1(b) demonstrates a representative floor retrofitted with the MR damper devices on the basis of the previous study [115]. As illustrated in Figure 8-1(b), floor rotates about the center of rigidity (C.R.), and the controlling moment due to the eccentricity of the control devices are determined based on their distance, d_i, from the center of mass (C.M.); e_x and e_y are the mass eccentricity with respect to the center of rigidity. The diagonal elements that connect the MR dampers to the main frames are considered rigid in this study.

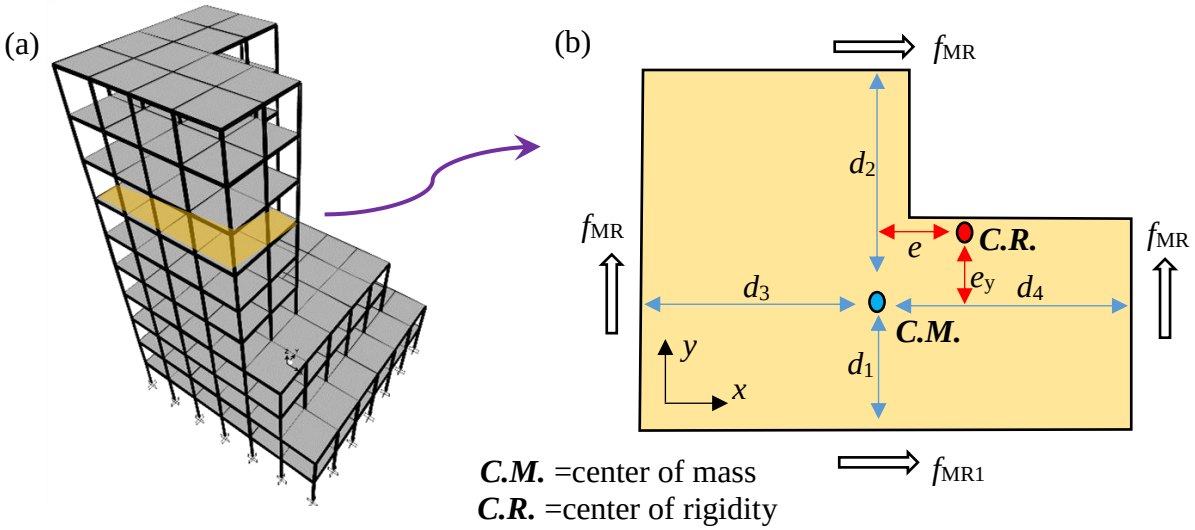

Figure 8-1. Dynamic system retrofitted with MR dampers: a) overview of a highly-irregular tall building and b) plan view of a representative floor with MR dampers

The motion of a controlled building can be described using the general governing equations of motion for a controlled nDOF system as follow [12, 115]:

$$[\boldsymbol{M}]\{\ddot{x}(t)\} + [\boldsymbol{C}]\{\dot{x}\} + [\boldsymbol{K}]\{x\} = [\boldsymbol{\gamma}]\{u(t)\} + \{\boldsymbol{\delta}\}\ddot{x}_g(t) \tag{8-1}$$

where, $\boldsymbol{M}$, $\boldsymbol{C}$, and $\boldsymbol{K}$ are the mass, damping, and stiffness matrices in three-dimensions, and x, $\dot{x}$, $\ddot{x}$ are the displacement, velocity and acceleration vectors with respect to the ground, respectively. $\{\boldsymbol{\delta}\}$ is the coefficient vector for the ground acceleration $\ddot{x}_g(t)$, which needs be defined for bidirectional earthquake loads in two directions. Input control forces, $\{\boldsymbol{u}(t)\}$, on each degrees of freedom are determined by the controllers location matrix, $[\boldsymbol{\gamma}]$. For the numerical simulations, the equation should be rewritten in the state-space form as [12]:

$$\{\dot{\boldsymbol{Z}}(t)\} = [\boldsymbol{A}]\{\boldsymbol{Z}(t)\} + [\boldsymbol{B}_u]\{\boldsymbol{u}(t)\} + \{\boldsymbol{B}_r\}\ddot{x}_g(t) \tag{8-2}$$

where

$$\{Z(t)\} = \begin{Bmatrix} x(t) \\ \dot{x}(t) \end{Bmatrix}; A = \begin{bmatrix} [0] & I \\ -M^{-1}K & -M^{-1}C \end{bmatrix}; \{B_u\} = \begin{bmatrix} [0] \\ M^{-1}[\gamma] \end{bmatrix}; \{B_r\} = \begin{bmatrix} \{0\} \\ [M]^{-1}\{\delta\} \end{bmatrix} \tag{8-3}$$

8.1.2. Inclusion of SSI effects

Inclusion of SSI effects to controlled structures has been investigated by researchers [115, 132, 133]. Nazarimofrad and Zahrai [115] presented a detailed work on the formulation of dynamic structures considering the SSI effects. The SSI effects are ideally simplified in the mass, damping and stiffness matrices in Equation (8-1). The derivation of the assembly of mass, stiffness and damping matrices could be found in Nazarimofrad and Zahrai [115]. As such, the stiffness matrix of the whole system can be assembled as [115]:

$$K = \begin{bmatrix} K_{11} & \mathbf{0} \\ \mathbf{0^T} & K_{22} \end{bmatrix} \tag{8-4}$$

where K_{11} and K_{22} are the stiffness matrices of the superstructure and the soil [115],

$$K_{11} = \begin{bmatrix} k_1 + k_2 & -k2 & 0 & 0 & 0 \\ -k2 & k2 + k_3 & -k_3 & 0 & 0 \\ 0 & -k_3 & \ddots & \vdots & 0 \\ 0 & 0 & \dots & \ddots & -k_n \\ 0 & 0 & 0 & -k_n & k_n \end{bmatrix}, \quad K_{22} = \begin{bmatrix} k_{x,s} & 0 & 0 & 0 & 0 \\ 0 & k_{y,s} & 0 & 0 & 0 \\ 0 & 0 & k_{t,s} & 0 & 0 \\ 0 & 0 & 0 & k_{rx,s} & 0 \\ 0 & 0 & 0 & 0 & k_{ry,s} \end{bmatrix} \tag{8-5}$$

The stiffness and damping of the linear springs and dashpots corresponding to the five degree of freedom considers for the base of the structure; lateral, rotation, and rocking. The

damping and stiffness parameters for considering the soil-structure interaction can be obtained using the equations given in Table 8-1.

Table 8-1. Properties of the springs and dashpots [35, 36].

Motion	Swaying	Rocking	Twisting
r	$\sqrt{\frac{A_0}{\pi}}$	$\sqrt[4]{\frac{4I_x}{\pi}}$ or $\sqrt[4]{\frac{4I_y}{\pi}}$	$\sqrt[4]{\frac{2I_z}{\pi}}$
Stiffness	$k_s = \frac{8\rho V_s^2 r}{2-\nu}$	$k_r = \frac{8\rho V_s^2 r^3}{3(1-\nu)}$	$k_t = \frac{16\rho V_s^2 r^3}{3}$
Damping	$c_s = \frac{4.4r^2}{2-\nu}.\rho V_s$	$c_r = \frac{0.4r^4}{1-\nu}.\rho V_s$	$c_t = 0.8r^4\rho V_s$

8.2. MR damper and its parameters

The model parameters of the MR damper [91] are given in Table 8-2.

Table 8-2. The model parameters of the MR damper.

Parameter	Value	Parameter	Value
c_{0a}	50.30 (kN s/m)	α_a	8.70 (kN/m)
c_{0b}	48.70 (kN s/m V)	α_b	6.40 (kN/m V)
c_{1a}	8106.2 (kN s/m)	γ	496 m-2
c_{1b}	7807.9 (kN s/m V)	β	496 m-2
k_0	0.0054 (kN/m)	A	810.50
k_1	0.0087 (kN/m)	n	2
x_0	0.18 (m)	η	190 s^{-1}

8.3. Control algorithms

To determine appropriate control algorithms for the command voltage of the MR dampers, four of the most commonly used methods, including semi-active control, passive-on, passive-off and active control algorithms, are herein used to evaluate the seismic performance of the controlled system under different circumstances. The LQR algorithm is employed to determine the optimal

input control forces and the LQR method has been used for semi-active control by Azimi et al [94], and in this study, we select FLC, because it could effectively determine the command voltage based on fuzzy interference functions, and thus fit for irregular building controlling to reduce structural dynamic responses. The designed FLC attempt to determine the command voltage for the MR dampers based on the displacement and velocity of the top floor. Thus, both input variables are defined using seven Gaussian membership functions, and the output variable is defined using five Gaussian membership functions. The inputs variables as well as the output are scaled to define the fuzzy inference system (FIS).

8.4. Numerical studies

8.4.1. Prototype of a 10-story irregular framed building

A ten-story irregular framed building is selected from the literature [115] for numerical simulations. The overview of the building and the plan view of the typical floor are illustrated in Figs. 8-2(a) and 8-2(c). For this model, all the columns are assumed to have the same stiffness in both directions, and each floor is considered as a rigid diaphragm. Using these assumptions, the stiffness of the i^{th} column in both directions, with the height of h_i and the moment of inertia of I_i, can be estimated as: $k_i = \frac{12EI_i}{h_i^3}$, where E is the Young's modulus of the steel.

Fig. 8-3 displays the first six mode shapes and the corresponding natural frequencies of the building. It is evident that for irregular structures, the traditional shear-frame models do not result in an optimal design, particularly under bidirectional loads with different accelerations. All of the modes consist of displacements in both directions and rotation; therefore, it is appropriate to place the dampers within the external frames with considerable distance with respect to the center of mass as proposed in Fig. 8-1, in order to use the advantages of the generated moment forces due to the eccentricity.

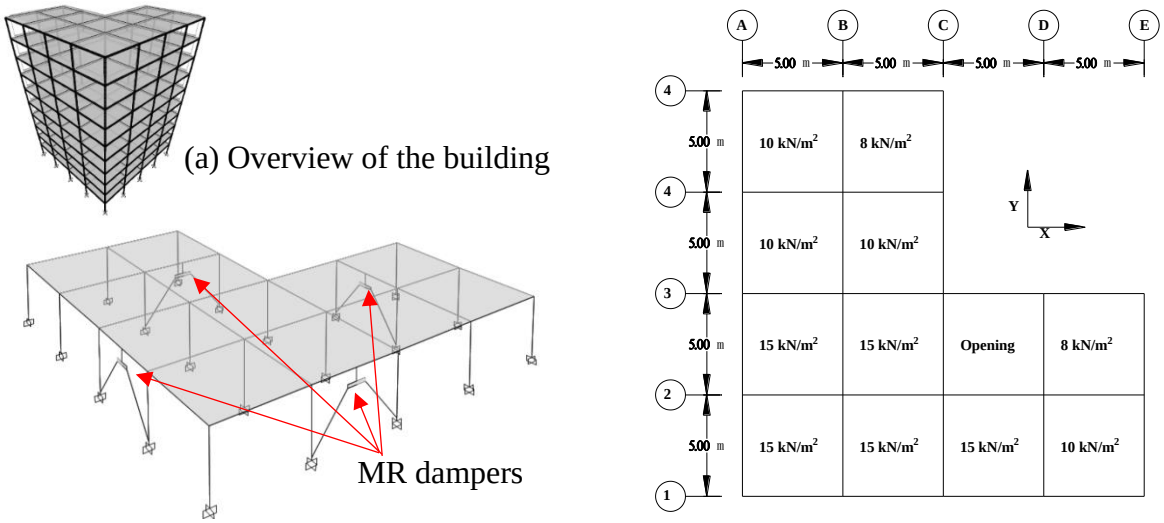

(b) 3D view of the first floor (c) Plan view of the floor (identical to rest floors)

Figure 8-2. Verification of the results for the uncontrolled building considering SSI effects under the Northridge earthquake (revised from [115]).

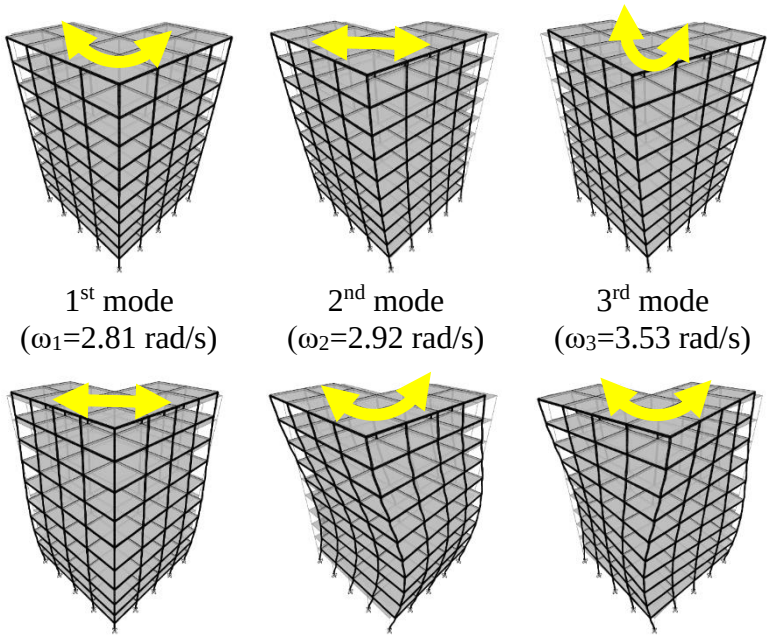

Figure 8-3. First six modes of the irregular building.

8.4.2. Soil properties

To consider the soil-structure interaction effects, soft soil is simulated by using five springs and dashpots with respect to five degrees of freedom: swaying and rocking in *x* and *y*

direction, and twisting about *z* and y. Two cases, buildings on rock base and on soft soil base, are addressed herein. The soil has a Poisson's ratio of 0.33, density of 2400 kg/m^2, shear-wave velocity of 500 m/s, and shear modulus of 6×10^8 N/m^2 [115].

8.4.3. Earthquake loads

Six of the most commonly used historic earthquake records are chosen in order to evaluate the performance of the semi-actively controlled system with MR dampers. The elastic acceleration response spectra of earthquakes are plotted in Figure 8-4 for both directions.

Table 8-3. Characteristics of six historical earthquake records used in this study.

Earthquake*	Station & Direction	Magnitude (Mw)	PGA (g)	PGV (cm/s)
1940 El Centro	El Centro Array #9 270°	7.2	0.21	31.3
	El Centro Array #9 180°	7.2	0.28	30.9
1994 Northridge	Sylmar - Olive View Med FF 360°	6.7	0.84	129.6
	Sylmar - Olive View Med FF 090°	6.7	0.61	77.5
1995 Kobe	H1170546.KOB 090°	7.2	0.63	76.1
	H1170546.KOB 000°	7.2	0.83	91.1
1999 Chi-Chi	TCU068 N	7.6	0.37	264.1
	TCU068 E	7.6	0.51	249.6
1971 San Fernando	Pacoima Dam 164°	6.6	1.22	114.5
	Pacoima Dam 254°	6.6	1.24	57.3
1989 Loma Prieta	Hollister - South & Pine 0°	6.9	0.37	63.0
	Hollister - South & Pine 0°	6.9	0.18	30.9

Source: http://ngawest2.berkeley.edu/

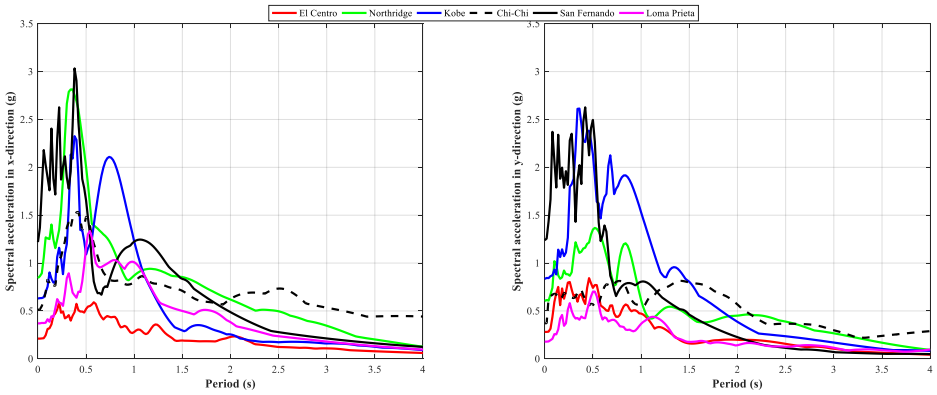

Figure 8-4. Unscaled spectral acceleration for the selected six historical earthquakes.

In order to investigate the performance of the control system, as well as the soil-structure effects, and the behavior of the building under near- field and far-field earthquakes, two sets of near- and far-field earthquakes are selected. The far-field earthquakes set includes the 22 bidirectional earthquake records that were used in FEMA P695 (ATC-63) [116].

Table 8-4. Characteristics of 22 far-field earthquake records.

No.	Earthquake*	Year	Station	Mw	Dist. (km)	Mechanism	PGA (g)	PGV (cm/s)	PGD (cm)	PGV/PGA (s)
1	Northridge	1994	Beverly Hills - Mulhol	6.7	13.3	Blind thrust	0.52	0.46	60.9	0.0009
2	Northridge	1994	Canyon Country-WLC	6.7	26.5	Blind thrust	0.48	0.44	44.2	0.0009
3	Duzce, Turkey	1999	Bolu	7.1	41.3	Strike-slip	0.82	0.77	59.3	0.0010
4	Hector Mine	1999	Hector	7.1	26.5	Strike-slip	0.34	0.30	34.6	0.0009
5	Imperial Valley	1979	Delta	6.5	33.7	Strike-slip	0.35	0.29	29.3	0.0008
6	Imperial Valley	1979	El Centro Array #11	6.5	29.4	Strike-slip	0.38	0.37	38.1	0.0010
7	Kobe, Japan	1995	Nishi-Akashi	6.9	8.7	Strike-slip	0.51	0.51	37.0	0.0010
8	Kobe, Japan	1995	Shin-Osaka	6.9	46	Strike-slip	0.24	0.23	32.5	0.0010
9	Kocaeli, Turkey	1999	Duzce	7.5	98.2	Strike-slip	0.36	0.33	52.3	0.0009
10	Kocaeli, Turkey	1999	Arcelik	7.5	53.7	Strike-slip	0.22	0.18	26.5	0.0008
11	Landers	1992	Yermo Fire Station	7.3	86	Strike-slip	0.24	0.19	39.1	0.0008
12	Landers	1992	Coolwater	7.3	82.1	Strike-slip	0.42	0.34	33.0	0.0008
13	Loma Prieta	1989	Capitola	6.9	9.8	Strike-slip	0.53	0.48	32.0	0.0009
14	Loma Prieta	1989	Gilroy Array #3	6.9	31.4	Strike-slip	0.56	0.45	40.0	0.0008
15	Manjil, Iran	1990	Abbar	7.4	40.4	Strike-slip	0.51	0.51	48.4	0.0010
16	Superstition Hills	1987	El Centro Imp. Co.	6.5	35.8	Strike-slip	0.36	0.30	43.6	0.0008
17	Superstition Hills	1987	Poe Road (temp)	6.5	11.2	Strike-slip	0.45	0.37	34.3	0.0008
18	Cape Mendocino	1992	Rio Dell Overpass	7.0	22.7	Thrust	0.55	0.46	43.0	0.0009
19	Chi-Chi, Taiwan	1999	CHY101	7.6	32	Thrust	0.44	0.39	90.2	0.0009
20	Chi-Chi, Taiwan	1999	TCU045	7.6	77.5	Thrust	0.51	0.49	37.9	0.0010
21	San Fernando	1971	LA - Hollywood Stor	6.6	39.5	Thrust	0.21	0.19	16.8	0.0009
22	Friuli, Italy	1976	Tolmezzo	6.5	20.2	Thrust	0.35	0.33	26.1	0.0010

Source: http://ngawest2.berkeley.edu/

Table 8-5. Characteristics of 30 near-field earthquake records.

No.	Earthquake*	Year	Station	Mw	Dist. (km)	Mechanism	PGA (g)	PGV (cm/s)	PGD (cm)	PGV/PGA (s)
1	San fernando	1971	Pacoima Dam-Left Abutment	6.61	1.81	Reverse	1.22	114.47	39.02	0.10
2	Gazli	1976	Karakyr	6.8	5.46	Reverse	0.86	67.65	20.72	0.08
3	Coyote lake	1979	Gilroy Array #6	5.74	3.11	Strike-slip	0.42	44.35	12.44	0.11
4	Coalinga	1983	Pleasant Valley P.P. - bldg	6.36	8.41	Reverse	0.30	39.40	6.38	0.13
5	Morgan hill	1984	Anderson dam(Downstream)	6.19	3.26	Strike-slip	0.42	25.41	4.44	0.06
6	Nahanni, Canada	1985	Site1	6.76	9.6	Reverse	1.20	40.63	10.20	0.03
7	N. Palm Springs	1986	North Palm Springs	6.06	4.04	Reverse Oblique	0.69	65.99	16.17	0.10
8	Whittier Narrows-01	1987	Santa Fe Springs - E.Joslin	5.99	18.49	Reverse Oblique	0.47	34.39	6.50	0.07
9	Superstition Hills-02	1987	Parachute Test Site	6.54	0.95	Strike-slip	0.43	134.29	46.18	0.32
10	Loma Prieta	1989	Gilroy Array #2	6.93	11.07	Reverse Oblique	0.37	34.76	9.51	0.10
11	Sierra Madre	1991	Cogswell Dam-Right Abutment	5.61	22	Reverse	0.30	14.92	2.08	0.05
12	Erzican, Turkey	1992	Erzican	6.69	4.38	Strike-slip	0.50	78.16	28.04	0.16
13	Northridge-01	1994	LA dam	6.69	5.92	Reverse	0.43	74.84	19.06	0.18
14	Kobe	1995	KJMA	6.9	0.96	Strike-slip	0.83	91.11	21.11	0.11
15	"Kocaeli_ Turkey"	1999	Izmit	7.51	7.21	Strike-slip	0.17	22.33	11.84	0.13
16	"Kocaeli_ Turkey"	1999	Yarimca	7.51	4.83	Strike-slip	0.32	71.89	47.33	0.23
17	Chi-Chi	1999	TCU049	7.62	3.76	Reverse Oblique	0.28	53.55	74.26	0.20
18	Chi-Chi	1999	TCU065	7.62	0.57	Reverse Oblique	0.79	125.35	108.73	0.16
19	Chi-Chi	1999	TCU067	7.62	0.62	Reverse Oblique	0.50	92.06	101.37	0.19
20	Chi-Chi	1999	TCU072	7.62	7.08	Reverse Oblique	0.48	71.93	50.36	0.15
21	Chi-Chi	1999	TCU074	7.62	13.46	Reverse Oblique	0.60	70.37	21.32	0.12
22	Chi-Chi	1999	TCU075	7.62	0.89	Reverse Oblique	0.33	109.56	96.61	0.34
23	Chi-Chi	1999	TCU076	7.62	2.74	Reverse Oblique	0.43	59.76	43.29	0.14
24	Chi-Chi	1999	TCU078	7.62	8.2	Reverse Oblique	0.45	40.24	30.29	0.09
25	Chi-Chi	1999	TCU079	7.62	10.97	Reverse Oblique	0.59	70.54	7.55	0.12
26	Chi-Chi	1999	TCU082	7.62	5.16	Reverse Oblique	0.23	54.92	95.08	0.24
27	Chi-Chi	1999	TCU084	7.62	11.48	Reverse Oblique	1.01	128.82	34.78	0.13
28	Chi-Chi	1999	TCU089	7.62	9	Reverse Oblique	0.35	34.99	18.68	0.10
29	Chi-Chi	1999	TCU102	7.62	1.49	Reverse Oblique	0.30	91.72	104.54	0.31
30	Chi-Chi	1999	TCU128	7.62	13.13	Reverse Oblique	0.17	62.65	52.29	0.38

Source: http://ngawest2.berkeley.edu/

8.5. Results and discussion

8.5.1. Maximum responses

The maximum responses of the building under the six bidirectional earthquakes are discussed in this section. For each earthquake, the maximum roof displacement and acceleration in both directions, as well as the maximum rotation, are given in Table 8-6 and Table 8-7 for each control method for the building on rock base and on soft soil. The LQR algorithm is used to obtain the optimal control force for the active control, and the input voltage for the passive-off and passive-on controls is 0 and 5 volts, respectively. From Table 8-6, using the MR dampers in passive-off mode, offers 43%, 23%, 29%, 16%, 5%, and 33% reduction of the roof displacement for the six earthquakes, respectively, when the building is on soft soil, while for the building on the rock base, the reduction percentages are slightly smaller. Similarly, the peak acceleration is reduced by 44%, 28%, 35%, 13%, 22%, and 29%, respectively, for the six earthquakes and for the building on the soft soil base. These results shows that in the case of power loss, the system still offers a considerable response reduction, however, using the FLC control, the maximum roof displacements are reduced by 80%, 71%, 68%, 64%, 36%, and 55% for the building on the soft soil base and under the six earthquakes, respectively. By comparing the passive-on and FLC controllers, the passive-on method offers slightly more reduction in the maximum roof displacements, however, the acceleration responses reduction is larger using the FLC control. In general, for the building on the soft soil base, the maximum responses are smaller than those for the building built on the rock base.

Table 8-6. Maximum responses using different control techniques (on soft soil base).

Earthquake	Response	Uncontrolled	Active	Passive-off	Passive-on (5 volt)	FLC
	$U_{x,\max}$ (m)	0.26	0.04	0.15	0.06	0.05
	$U_{y,\max}$ (m)	0.23	0.03	0.17	0.05	0.05
El Centro	$\theta_{\max}$ (rad)	0.009	0.001	0.007	0.001	0.002
	$\ddot{U}_{x,\max}$ (m/s^2)	5.07	1.26	2.81	2.01	1.93
	$\ddot{U}_{y,\max}$ (m/s^2)	4.57	1.81	3.64	2.83	2.49
	$U_{x,\max}$ (m)	0.57	0.12	0.52	0.28	0.33
	$U_{y,\max}$ (m)	0.56	0.07	0.43	0.10	0.16
Northridge	$\theta_{\max}$ (rad)	0.039	0.005	0.034	0.012	0.016
	$\ddot{U}_{x,\max}$ (m/s^2)	10.94	4.38	7.78	6.64	6.24
	$\ddot{U}_{y,\max}$ (m/s^2)	8.56	2.73	6.04	4.88	4.79
	$U_{x,\max}$ (m)	0.31	0.07	0.22	0.09	0.10
	$U_{y,\max}$ (m)	0.41	0.07	0.35	0.16	0.21
Kobe	$\theta_{\max}$ (rad)	0.008	0.001	0.007	0.004	0.004
	$\ddot{U}_{x,\max}$ (m/s^2)	13.67	3.28	9.05	5.85	5.70
	$\ddot{U}_{y,\max}$ (m/s^2)	14.90	3.75	9.57	7.59	7.02
	$U_{x,\max}$ (m)	0.78	0.35	0.65	0.27	0.28
	$U_{y,\max}$ (m)	0.44	0.41	0.42	0.24	0.26
Chi-Chi	$\theta_{\max}$ (rad)	0.034	0.007	0.028	0.017	0.019
	$\ddot{U}_{x,\max}$ (m/s^2)	6.71	2.63	5.82	4.12	3.96
	$\ddot{U}_{y,\max}$ (m/s^2)	7.16	2.53	6.34	3.44	3.68
	$U_{x,\max}$ (m)	0.44	0.11	0.42	0.26	0.28
	$U_{y,\max}$ (m)	0.19	0.05	0.18	0.13	0.14
San Fernando	$\theta_{\max}$ (rad)	0.027	0.005	0.024	0.012	0.016
	$\ddot{U}_{x,\max}$ (m/s^2)	8.90	6.57	7.98	7.37	7.27
	$\ddot{U}_{y,\max}$ (m/s^2)	9.31	5.98	7.24	8.86	7.87
	$U_{x,\max}$ (m)	0.33	0.08	0.28	0.14	0.15
	$U_{y,\max}$ (m)	0.15	0.04	0.10	0.06	0.08
Loma Prieta	$\theta_{\max}$ (rad)	0.029	0.003	0.025	0.006	0.013
	$\ddot{U}_{x,\max}$ (m/s^2)	7.54	2.24	5.29	3.43	3.40
	$\ddot{U}_{y,\max}$ (m/s^2)	3.69	1.04	2.58	2.48	2.49

Table 8-7. Maximum responses using different control techniques (on rock base).

Earthquake	Response	Uncontrolled	Active	Passive-off	Passive-on (5 volt)	FLC
	$U_{x,\max}$ (m)	0.41	0.04	0.24	0.07	0.09
	$U_{y,\max}$ (m)	0.34	0.04	0.28	0.07	0.10
El Centro	$\theta_{\max}$ (rad)	0.014	0.001	0.011	0.001	0.003
	$\ddot{U}_{x,\max}$ (m/s^2)	6.73	2.11	4.58	2.79	2.83
	$\ddot{U}_{y,\max}$ (m/s^2)	5.32	3.30	5.06	3.88	3.49
	$U_{x,\max}$ (m)	0.88	0.17	0.79	0.47	0.53
	$U_{y,\max}$ (m)	0.83	0.10	0.67	0.19	0.28
Northridge	$\theta_{\max}$ (rad)	0.058	0.008	0.051	0.024	0.027
	$\ddot{U}_{x,\max}$ (m/s^2)	14.60	7.86	11.96	10.21	9.87
	$\ddot{U}_{y,\max}$ (m/s^2)	10.25	5.22	7.70	6.76	7.47
	$U_{x,\max}$ (m)	0.46	0.09	0.33	0.14	0.15
	$U_{y,\max}$ (m)	0.54	0.11	0.48	0.28	0.33
Kobe	$\theta_{\max}$ (rad)	0.012	0.002	0.012	0.006	0.006
	$\ddot{U}_{x,\max}$ (m/s^2)	13.77	5.52	10.30	8.33	8.28
	$\ddot{U}_{y,\max}$ (m/s^2)	15.45	6.14	13.62	11.40	10.85
	$U_{x,\max}$ (m)	1.22	0.23	1.06	0.42	0.50
	$U_{y,\max}$ (m)	0.64	0.19	0.63	0.40	0.44
Chi-Chi	$\theta_{\max}$ (rad)	0.050	0.007	0.043	0.026	0.028
	$\ddot{U}_{x,\max}$ (m/s^2)	9.18	5.19	8.40	6.25	6.02
	$\ddot{U}_{y,\max}$ (m/s^2)	9.00	5.02	8.39	5.84	5.68
	$U_{x,\max}$ (m)	0.63	0.16	0.61	0.40	0.44
	$U_{y,\max}$ (m)	0.27	0.08	0.26	0.20	0.21
San Fernando	$\theta_{\max}$ (rad)	0.040	0.006	0.036	0.019	0.025
	$\ddot{U}_{x,\max}$ (m/s^2)	13.09	12.66	12.00	11.03	11.50
	$\ddot{U}_{y,\max}$ (m/s^2)	12.57	11.35	10.63	14.04	13.78
	$U_{x,\max}$ (m)	0.50	0.11	0.44	0.24	0.26
	$U_{y,\max}$ (m)	0.19	0.04	0.17	0.11	0.15
Loma Prieta	$\theta_{\max}$ (rad)	0.039	0.004	0.034	0.012	0.030
	$\ddot{U}_{x,\max}$ (m/s^2)	8.74	3.61	6.84	5.22	5.47
	$\ddot{U}_{y,\max}$ (m/s^2)	3.80	1.84	2.69	3.60	5.44

8.5.2. Time-history responses

The time-history responses provide a tool to study the performance of any control techniques during earthquakes. Figure 8-5 to Figure 8-8 show the roof displacement time history response in x-, y-, and θ- direction for the building on soft soil base and rock under the El Centro and Northridge earthquakes. The Figures are in accordance with the aforementioned statements.

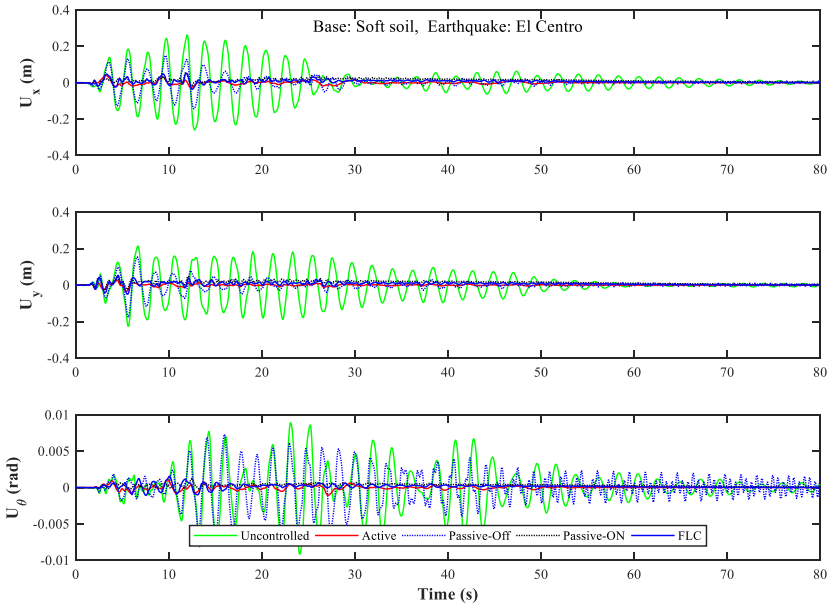

Figure 8-5. Time-history response of the building considering SSI effects under the El Centro earthquake.

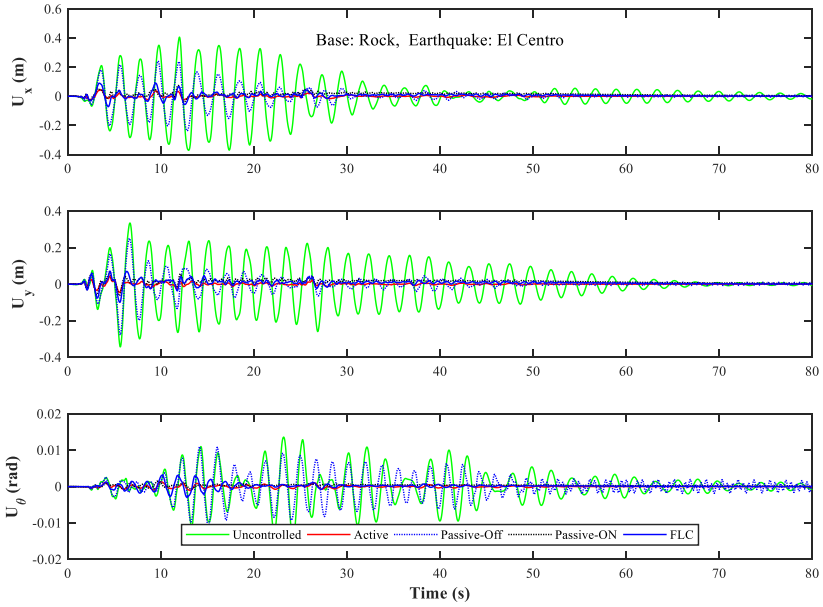

Figure 8-6. Time-history response of the building without considering SSI effects under the El Centro earthquake.

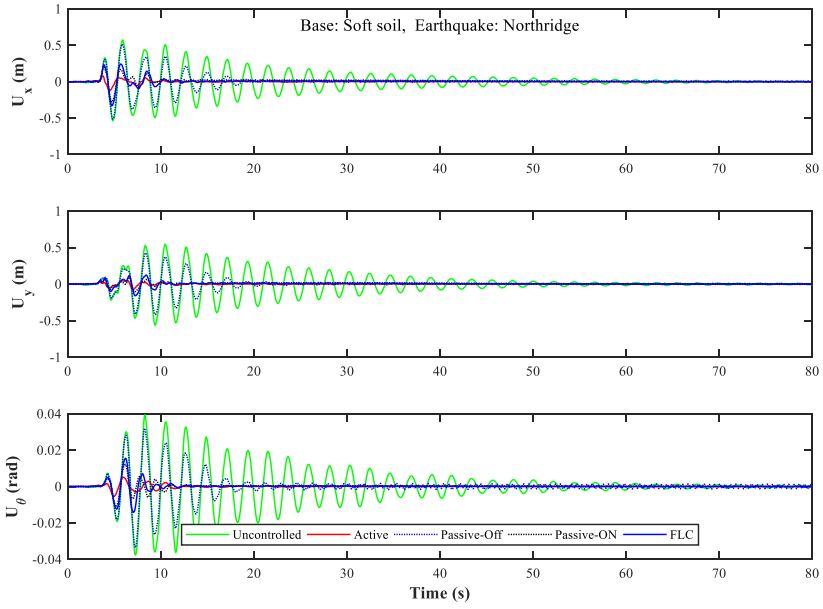

Figure 8-7. Time-history response of the building considering SSI effects under the Northridge earthquake.

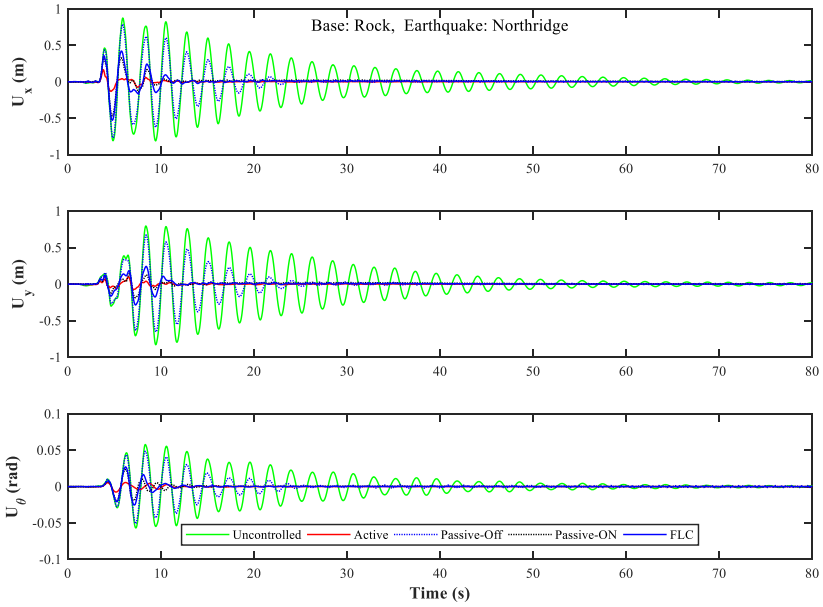

Figure 8-8. Time -history response of the building without considering SSI effects under the Northridge earthquake.

8.5.3. Inter-story drift and lateral displacement profiles

Inter-story drift can be used as a factor to measure the inter-story shear force, to estimate the seismic fragility of building, or for optimal placement of MR dampers. In addition, by decreasing the inter-story drifts, P-Δ effects are also reduced, and consequently, the corner columns would express linear behavior. Thus, as linear controller can be satisfactory. It is also worth to mention that the generated force in a MR damper is highly dependent on the relative displacement and velocity of the damper shaft, in addition to the input voltage. Therefore, using such devices on story levels with lower drift ratios may not guarantee the best performance.

Figure 8-9 and Figure 8-10 show the maximum inter-story drift profiles for the building in both directions under different bidirectional earthquake loads. As it is expected, the inter-story drifts are higher for the lower stories, and hence, installing semi-active control devices on those floor are more effective, and it is essential to control the excessive deformations of the corner

columns of the first stories. From the figure, for most of the cases, the active control using LQR algorithm has a superior performance compared to the other methods, followed by the fuzzy logic control. In addition, passive-off system shows minimum response reduction in case of power loss, which is considerably large for earthquakes like El Centro or Kobe. The fuzzy logic control and passive-on control offer similar performance in terms of response reduction with respect to the uncontrolled building, however, the FLC system is preferable considering the energy of control [94]. It is also very important to study the absolute lateral displacements of a building, particularly for such buildings with adjacent structures, or to investigate the P-Δ effects for large displacements. For this purpose, the absolute displacements in both directions as well as absolute maximum rotation profiles are shown in Figure 8-9.

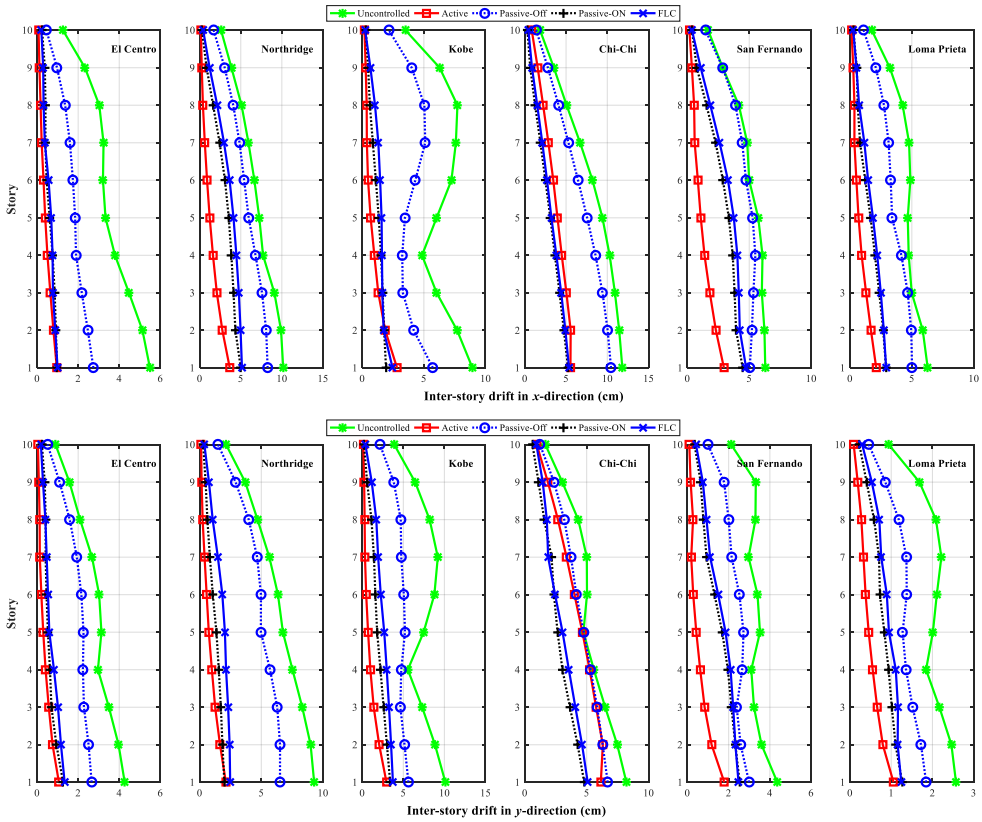

Figure 8-9. Inter-story drift profiles in X and Y direction.

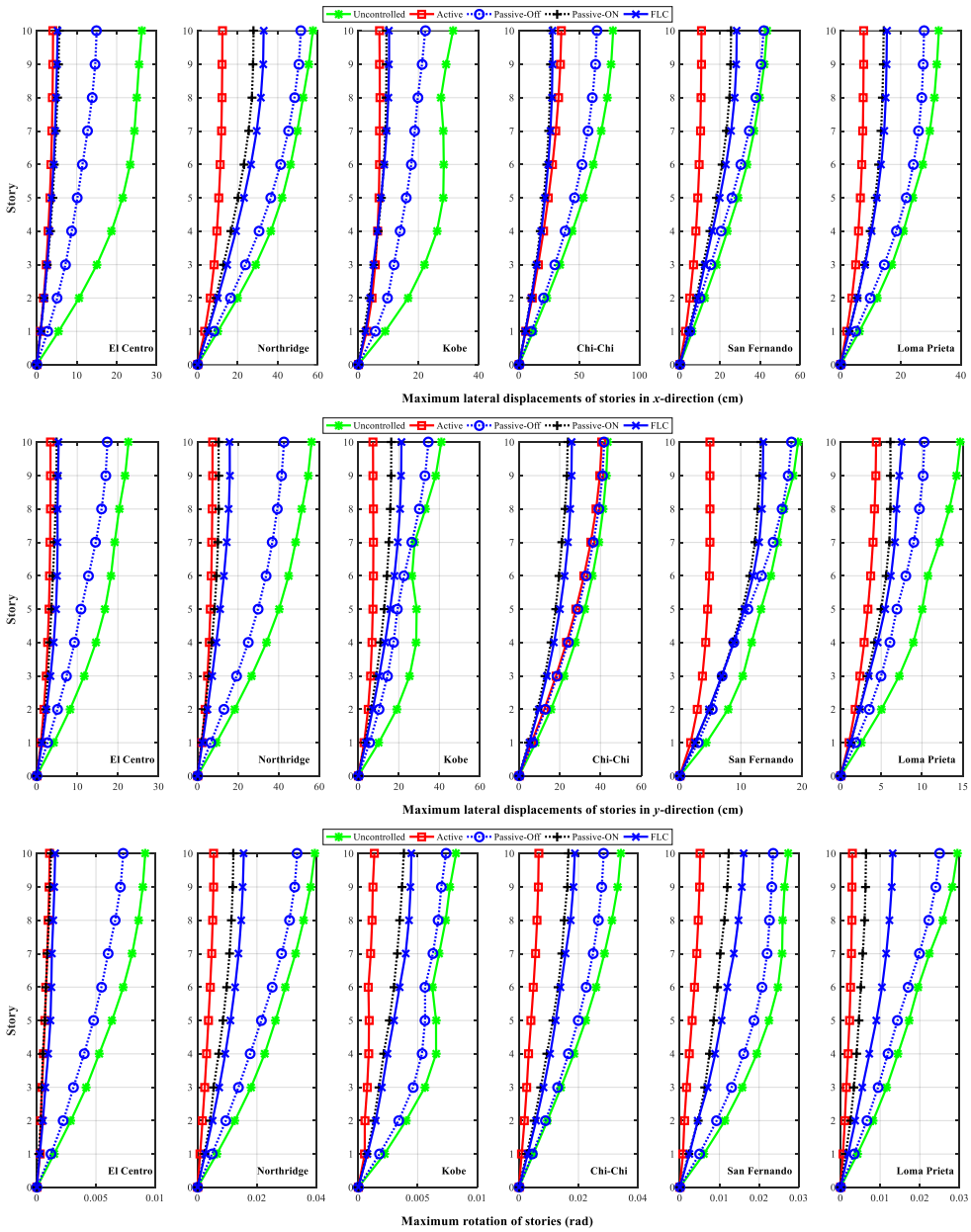

Figure 8-10. Absolute displacement profiles in X, Y, and θ-direction.

8.5.4. Effect of the number of MR dampers

During an earthquake, it is possible that either a number of devices would not work or the command signal line fails. In this section, four cases of active MR dampers are investigated. For the case I, only four MR dampers on the 1st floor are working, and the others are not considered. The second case, case II, the first two stories control the vibration with eight MR dampers. For

the other two cases, case III and case IV, MR dampers installed on the 1st-5th floors and all the floor are active and receive accurate command signals, respectively. Figure 8-11 shows the displacement responses of the building at the top floor in x-, y-, and θ-direction. It is obvious from the responses that the first two stories are very essential, however, case I offers a fast damping during an earthquake. Duration of cyclic loading can be critical when the structure is vulnerable for fatigue failures. From the figure, the vibration is controlled in about 40 seconds using by the case I, while, the case II, and the two other case, controls the displacement in less than 20 seconds. In terms of maximum response reduction, case II results in 17%, 38%, and 26% more reduction in roof displacement in x-, y-, and θ-direction, respectively. Similarly, case III with more devices, reduces the same responses by 44%, 72%, 55%, respectively. While adding more dampers benefits the structure by reducing the response, however, the results proves that using semi-active control devices such as MR dampers in uppers story levels does not contribute significantly in the response reduction compared to the devices installed on the first lower stories. For an optimal design, using additional MR dampers on lower levels, instead of top floors, may obtain a better performance and cost efficient.

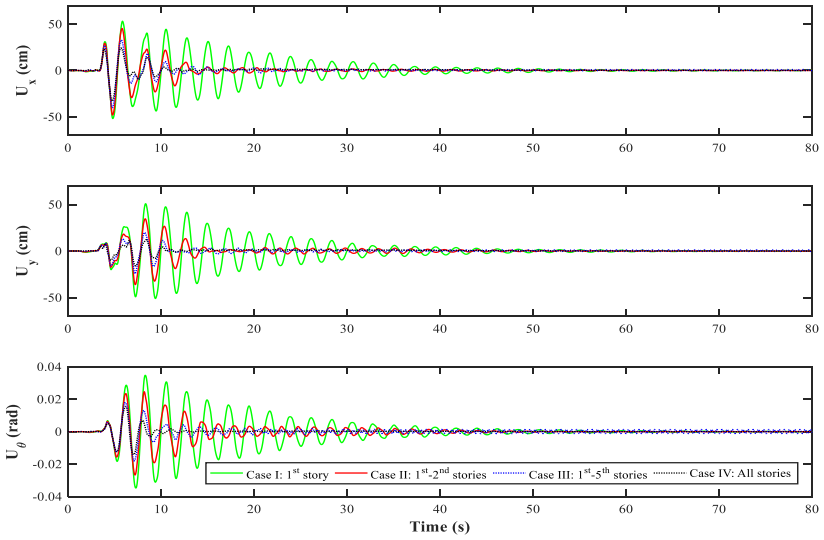

Figure 8-11. Effect of MR damper placement on the maximum response of building under Northridge earthquake.

8.5.5. Soil-structure interaction effects

Figure 8-12 and Figure 8-13 show the maximum roof displacement for both buildings on rock base and soft soil using the four control techniques under near- and far-field earthquakes. It can be seen that except for the few cases using the active control, regardless of near- or far-field ground motion, the response of the building on a soft soil is smaller. Thus, considering other requirements, it would be possible to implement simple and linear control systems for those structures that are built on soft soils. Accordingly, the computation time can be decreased.

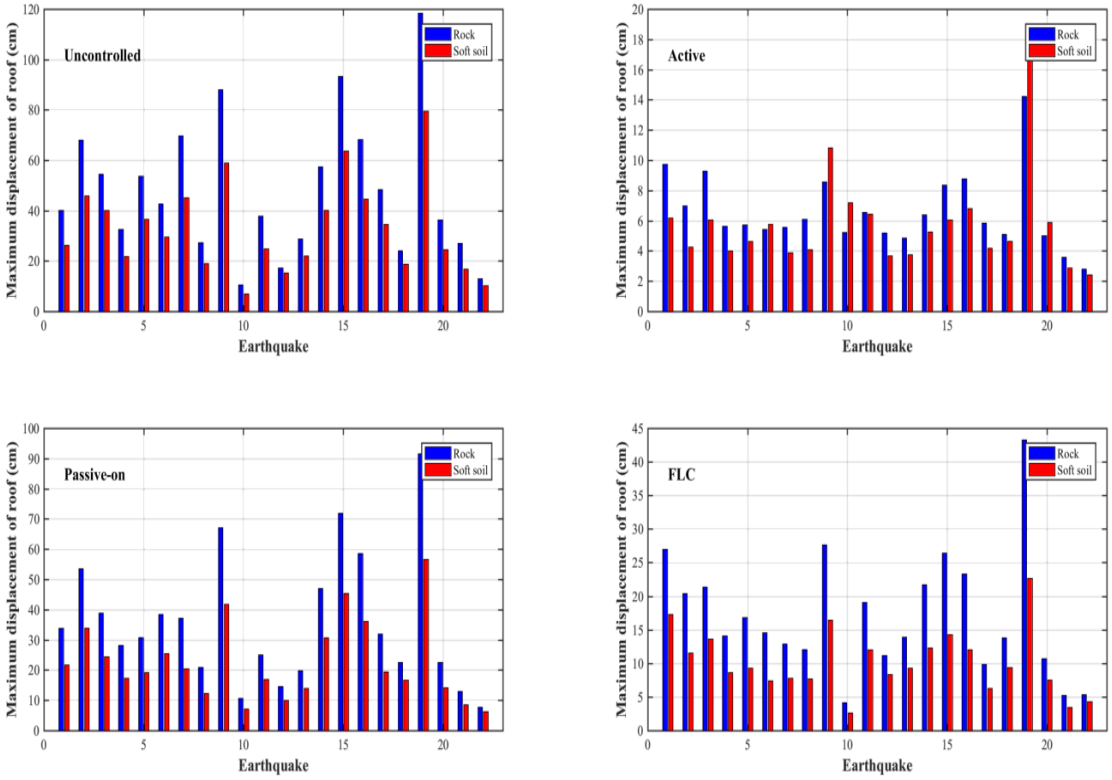

Figure 8-12. Soil-structure effects on the maximum roof displacements under far-field earthquakes.

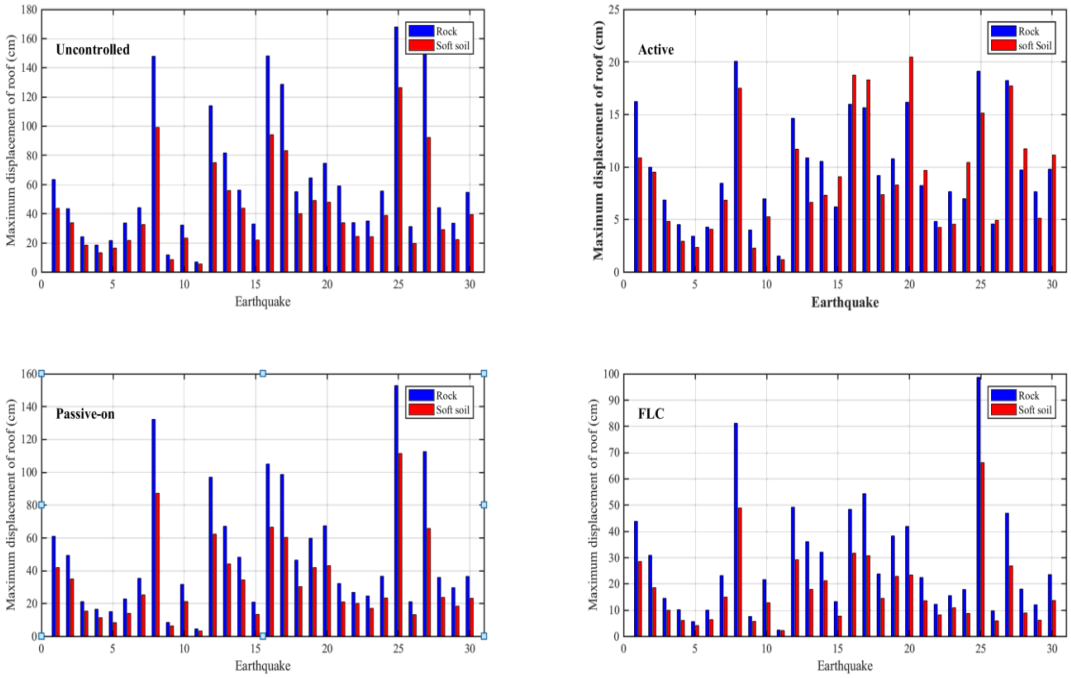

Figure 8-13. Soil-structure effects on the maximum roof displacements under near-field earthquakes.

8.6. Summary

In this section of the thesis, response of irregular building under bi-directional excitations is evaluated. The soil-structure interaction is also considered in the numerical simulations. The results show that the fuzzy logic control can be used to manage the input voltage of the installed MR dampers, effectively. The number of the MR dampers is also investigated. The results support the opinion that increasing the number of MR dampers in lower stories are more effective than the upper ones.

9. SUMMARY, CONCLUSIONS AND FUTURE WORK

9.1. Summary

Practicing engineers have long recognized that structural response of buildings to strong ground motions due to earthquakes frequently results in inelastic behavior. Major earthquakes in recent years have highlighted the big concern of modern seismic design concept for resilience of buildings. Clearly, proven detailing seismic design for conventional buildings, that is, use of damping of conventional building materials and structural components alone, could not effectively allow dissipating such considerable dynamic energy and consequently lead to severe structural damage. Research on innovative designs and materials for new and existing buildings has demonstrated their enhanced seismic performance. For instance, control of seismic vibrations of structures using semi-active devices gained enormous attentions, particularly in the fields of control algorithms and new dampers. Thus, the overall goals of this thesis aim to design structural vibration control using smart materials and devices, and to elucidate the factors determining their robustness, feasibility and adaptability for earthquake-resistant and resilient buildings.

To accommodate different performance levels under small, moderate, and strong earthquakes in performance-based engineering, the study mainly includes a) integrated wavelet-based vibration control with damage detection for base-isolated buildings; b) shape memory alloy (SMA) cables used to eliminate the residual deformations of lead rubber bearing isolator system; dc) a twin tuned mass damper for highly irregular tall buildings; and d) soil-structure interaction (SSI) effects on the buildings with control systems. The robustness, feasibility and adaptability of these proposed studies for earthquake-resistant and resilient buildings are

evaluated using peak response (Maximum drift and maximum acceleration of stories of the buildings), performance index under various ground motions, and energy of control.

9.2. Conclusions

The findings of the study reveal that the proposed structural vibration control strategies could advance the current-of-art knowledge: Firstly, the integrated method enables seismic analysis and mitigation of damaged base-isolated structures, and effectively accounts for the impacts of damage levels to the efficiency of control systems. Secondly, the benefits of SMA in the control systems are also demonstrated by reduction in permanent deformation on the bases, which further enhance the effectiveness of the control systems for seismic mitigation. Thirdly, the severe torsion of highly irregular tall buildings under strong ground motions could be effectively mitigated by using the proposed damper systems. Finally, the study exhibits that the controlled buildings could yield a further reduction in dynamic response when considering the SSI effects.

Specifically, the study has been conducted on the performance of base-isolated buildings. During the life span of any building, structural and non-structural damages are expected. Even for the controllable buildings, damage level parameter is missing from the computations. Therefore, in this research, an integrated control algorithm is proposed to consider the damage level that is occurred prior to an earthquake. For this purpose, the damage level is identified using the NExt and ARE methods. The results are used as the inputs variables for the designed FLC. To avoid the resonance phenomenon, wavelet packet transform is used to estimate the dominant frequency of an earthquake and matching with the frequency of the primary natural frequency of the structure.

The residual deformations of base-isolators is also investigated, and an new control system is proposed using superelastic materials along with the typical LRB isolators, which can

be controlled using MR damper and by means of a fuzzy logic controller. The results demonstrate that, regardless of using a controller, SMA cables significantly eliminate the residual relative displacements of base-isolators, particularly under near-field earthquakes.

Two key elements of designing an optimal control systems for highly-irregular buildings are the SSI effects and the coupled torsional-translational vibration. In this research, a twin tuned mass damper system is explored to suppress the couple translational-torsional vibrations with an optimal design. Introducing an active or semi-active controller to the system enhanced the performance of the system even more. Finally, the SSI effects are considered in the numerical simulations for the irregular tall building that is controlled using a network of MR dampers. Time-history analyses indicate that the buildings that are built on soft soil have smaller responses compared to those on rock base.

9.3. Future work

The field of smart structures is evolving by introducing the new interdisciplinary tools and by means of the artificial intelligence, in the future, buildings will be smarter and controllable. Application of new materials as well as new computational methods will pave the path for practical engineers to confidently use the advanced technology to design a resilient community.

REFERENCES

[1] G. P. Warn and K. L. Ryan, "A review of seismic isolation for buildings: historical development and research needs," *Buildings*, vol. 2, pp. 300-325, 2012.

[2] A. Kaveh, T. Bakhshpoori, and M. Azimi, "Seismic optimal design of 3D steel frames using cuckoo search algorithm," *The Structural Design of Tall and Special Buildings*, vol. 24, pp. 210-227, 2015.

[3] O. Lavan, "A methodology for the integrated seismic design of nonlinear buildings with supplemental damping," *Structural Control and Health Monitoring*, vol. 22, pp. 484-499, 2015.

[4] G. G. Amiri, M. Azimi, and E. Darvishan, "Retrofitting I-beam to double-I built-up column connections using through plates and T-stiffeners," *Scientia Iranica. Transaction A, Civil Engineering*, vol. 20, p. 1695, 2013.

[5] A. Mosleh, M. S. Razzaghi, J. Jara, and H. Varum, "Seismic fragility analysis of typical pre-1990 bridges due to near-and far-field ground motions," *International Journal of Advanced Structural Engineering (IJASE)*, vol. 8, pp. 1-9, 2016.

[6] A. Mosleh, H. Rodrigues, H. Varum, A. Costa, and A. Arêde, "Seismic behavior of RC building structures designed according to current codes," in *Structures*, 2016, pp. 1-13.

[7] A. Nicknam, A. Mosleh, and H. H. Jamnani, "Seismic performance evaluation of urban Bridge using static nonlinear procedure, case study: Hafez Bridge," *Procedia Engineering*, vol. 14, pp. 2350-2357, 2011.

[8] M. Rashidi and S. M. Haeri, "Evaluation of the behavior of earth and rockfill dams during construction and first impounding using instrumentation data and numerical modeling (Case Study: Gavoshan dam)," Sharif University of Technology, 2012.

[9] M. Rashidi, M. Heidari, and G. Azizyan, "Numerical Analysis and Monitoring of an Embankment Dam During Construction and First Impounding (Case Study: Siah Sang Dam)," *Scientia Iranica Journal*, 2017.

[10] M. Rashidi and H. Takhtfiroozeh, "Determination of Bond Capacity in Reinforced Concrete Beam and Its Influence on the Flexural Strength," *Mechanics, Materials Science & Engineering*, vol. 6, 2016.

[11] A. V. Srinivasan and D. M. McFarland, "Smart structures, analysis and design," ed: AAPT, 2001.

[12] F. Y. Cheng, H. Jiang, and K. Lou, *Smart structures: innovative systems for seismic response control*: CRC Press, 2008.

[13] C.-S. Teodorescu, S. Diop, I. Politopoulos, and M. Benidir, "A robust nonlinear semi-active control for base seismically-isolated structures," in *Control & Automation (MED), 2013 21st Mediterranean Conference on*, 2013, pp. 545-550.

[14] F. Oliveira, P. G. de Morais, and A. Suleman, "Semi-active Control of Base-isolated Structures," *Procedia Engineering*, vol. 114, pp. 401-409, 2015.

[15] O. E. Ozbulut and S. Hurlebaus, "Evaluation of the performance of a sliding-type base isolation system with a NiTi shape memory alloy device considering temperature effects," *Engineering Structures*, vol. 32, pp. 238-249, 1// 2010.

[16] Y. Zhang and S. Zhu, "A shape memory alloy-based reusable hysteretic damper for seismic hazard mitigation," *Smart Materials and Structures*, vol. 16, p. 1603, 2007.

[17] C. W. Xu, K. C. Huo, Z. G. Ren, R. Xiong, and T. Yang, "Application of Stress Box in Self-Stressing Test of Expansion Concrete Filled Steel Tube," in *Advanced Materials Research*, 2013, pp. 530-534.
[18] N. Krishnamra, E. Limuwan, and J. Dawe, "Spiral Post-Tensioning System for Concrete Members," in *IABSE Symposium Report*, 2009, pp. 72-79.
[19] E. Choi, Y.-S. Chung, J. Park, and B.-S. Cho, "Behavior of reinforced concrete columns confined by new steel-jacketing method," *ACI Structural Journal*, vol. 107, p. 654, 2010.
[20] S. C. Goel, W. C. Liao, M. Reza Bayat, and S. H. Chao, "Performance-based plastic design (PBPD) method for earthquake-resistant structures: an overview," *The structural design of tall and special buildings*, vol. 19, pp. 115-137, 2010.
[21] O. E. Ozbulut, M. Bitaraf, and S. Hurlebaus, "Adaptive control of base-isolated structures against near-field earthquakes using variable friction dampers," *Engineering Structures*, vol. 33, pp. 3143-3154, 12// 2011.
[22] M. Bitaraf and S. Hurlebaus, "Semi-active adaptive control of seismically excited 20-story nonlinear building," *Engineering Structures*, vol. 56, pp. 2107-2118, 2013.
[23] N. Fisco and H. Adeli, "Smart structures: part I—active and semi-active control," *Scientia Iranica*, vol. 18, pp. 275-284, 2011.
[24] G. Housner, L. A. Bergman, T. K. Caughey, A. G. Chassiakos, R. O. Claus, S. F. Masri, *et al.*, "Structural control: past, present, and future," *Journal of engineering mechanics*, vol. 123, pp. 897-971, 1997.
[25] M. Bhardwaj and T. Datta, "Semiactive fuzzy control of the seismic response of building frames," *Journal of Structural Engineering*, vol. 132, pp. 791-799, 2006.
[26] F. Amini, S. A. Mohajeri, and M. Javanbakht, "Semi-active control of isolated and damaged structures using online damage detection," *Smart Materials and Structures*, vol. 24, p. 105002, 2015.
[27] A. Y. Fallah and T. Taghikhany, "Sliding mode fault detection and fault-tolerant control of smart dampers in semi-active control of building structures," *Smart Materials and Structures*, vol. 24, p. 125030, 2015.
[28] N. Kurata, "Actual seismic response control building with semi-active damper system," in *Structures 2001: A Structural Engineering Odyssey*, ed, 2001, pp. 1-8.
[29] A. Nishitani, Y. Nitta, and Y. Ikeda, "Semiactive structural-control based on variable slip-force level dampers," *Journal of Structural Engineering*, vol. 129, pp. 933-940, 2003.
[30] T. Soong and B. Spencer, "Supplemental energy dissipation: state-of-the-art and state-of-the-practice," *Engineering structures*, vol. 24, pp. 243-259, 2002.
[31] H. Kurino, J. Tagami, K. Shimizu, and T. Kobori, "Switching oil damper with built-in controller for structural control," *Journal of Structural Engineering*, vol. 129, pp. 895-904, 2003.
[32] Y. Ikeda, "Active and semi-active vibration control of buildings in Japan—Practical applications and verification," *Structural Control and Health Monitoring*, vol. 16, pp. 703-723, 2009.
[33] O. Cundumi and L. Suárez, "A new variable damping semiactive device for seismic response reduction of civil structures," *Journal of Mechanics of Materials and Structures*, vol. 2, pp. 1639-1656, 2007.

[34] K. Kazemi Bidokhti, H. Moharrami, and A. Fayezi, "Semi-active fuzzy control for seismic response reduction of building frames using SHD dampers," *Structural Control and Health Monitoring,* vol. 19, pp. 417-435, 2012.
[35] M.-H. Shih and W.-P. Sung, "Development of semi-active hydraulic damper as active interaction control device to withstand external excitation," *Sadhana,* vol. 39, pp. 123-138, 2014.
[36] N. Kurata, T. Kobori, M. Takahashi, T. Ishibashi, N. Niwa, J. Tagami, *et al.*, "Forced vibration test of a building with semi-active damper system," *Earthquake engineering & structural dynamics,* vol. 29, pp. 629-645, 2000.
[37] C.-G. Go, C.-H. Sui, M.-H. Shih, and W.-P. Sung, "A linearization model for the displacement dependent semi-active hydraulic damper," *Journal of Vibration and Control,* vol. 16, pp. 2195-2214, 2010.
[38] H. Kurino, S. Orui, and K. Shimizu, "Structural control by innovative oil damper with automatic on/off valve operation," *J. Disaster Res,* vol. 4, pp. 253-260, 2009.
[39] A. Kaveh and A. Dadras, "A novel meta-heuristic optimization algorithm: Thermal exchange optimization," *Advances in Engineering Software,* 2017.
[40] A. Kaveh and A. Dadras, "A guided tabu search for profile optimization of finite element models," *International Journal of Optimization in Civil Engineering,* vol. 7, pp. 527-537, 2017.
[41] A. Kaveh and A. Dadras, "Structural damage identification using an enhanced thermal exchange optimization algorithm," *Engineering Optimization,* pp. 1-22, 2017.
[42] J. Zhang, K. Zeng, and J. Jiang, "An optimal design of bi-directional TMD for three dimensional structure," *Computational Structural Engineering,* pp. 935-941, 2009.
[43] A. A. Farghaly and M. Salem Ahmed, "Optimum design of TMD system for tall buildings," *ISRN Civil Engineering,* vol. 2012, 2012.
[44] J. P. Den Hartog, *Mechanical vibrations*: Courier Corporation, 1985.
[45] C. Li and Y. Liu, "Further characteristics for multiple tuned mass dampers," *Journal of Structural Engineering,* vol. 128, pp. 1362-1365, 2002.
[46] S. Pourzeynali, H. Lavasani, and A. Modarayi, "Active control of high rise building structures using fuzzy logic and genetic algorithms," *Engineering Structures,* vol. 29, pp. 346-357, 2007.
[47] P. Lin, L. Chung, and C. Loh, "Semiactive control of building structures with semiactive tuned mass damper," *Computer-Aided Civil and Infrastructure Engineering,* vol. 20, pp. 35-51, 2005.
[48] C. Cai, W. Wu, and M. Araujo, "Cable vibration control with a TMD-MR damper system: Experimental exploration," *Journal of structural engineering,* vol. 133, pp. 629-637, 2007.
[49] F. Weber, C. Boston, and M. Maślanka, "An adaptive tuned mass damper based on the emulation of positive and negative stiffness with an MR damper," *Smart Materials and Structures,* vol. 20, p. 015012, 2010.
[50] J. Kang, H. S. Kim, and D. G. Lee, "Mitigation of wind response of a tall building using semi-active tuned mass dampers," *The Structural Design of Tall and Special Buildings,* vol. 20, pp. 552-565, 2011.
[51] F. Weber and M. Maślanka, "Frequency and damping adaptation of a TMD with controlled MR damper," *Smart Materials and Structures,* vol. 21, p. 055011, 2012.

[52] A. Kaveh, S. Pirgholizadeh, and O. K. Hosseini, "Semi-active tuned mass damper performance with optimized fuzzy controller using CSS algorithm," *Asian J. Civil Eng.(BHRC),* vol. 16, pp. 587-606, 2015.
[53] R. Jangid and J. Kelly, "Base isolation for near-fault motions," *Earthquake engineering & structural dynamics,* vol. 30, pp. 691-707, 2001.
[54] E. A. Johnson, J. C. Ramallo, B. F. Spencer Jr, and M. K. Sain, "Intelligent base isolation systems," in *Proceedings of the Second World Conference on Structural Control*, 1998, pp. 367-76.
[55] G. Fraraccio, A. Brügger, and R. Betti, "Identification and damage detection in structures subjected to base excitation," *Experimental Mechanics,* vol. 48, pp. 521-528, 2008.
[56] D. M. Siringoringo and Y. Fujino, "Experimental study of laser Doppler vibrometer and ambient vibration for vibration-based damage detection," *Engineering Structures,* vol. 28, pp. 1803-1815, 2006.
[57] J. M. Caicedo, S. J. Dyke, and E. A. Johnson, "Natural excitation technique and eigensystem realization algorithm for phase I of the IASC-ASCE benchmark problem: Simulated data," *Journal of Engineering Mechanics,* vol. 130, pp. 49-60, 2004.
[58] S. Nagarajaiah and S. Narasimhan, "Seismic control of smart base isolated buildings with new semiactive variable damper," *Earthquake Engineering & Structural Dynamics,* vol. 36, pp. 729-749, 2007.
[59] M. Bitaraf, S. Hurlebaus, and L. R. Barroso, "Active and Semi-active Adaptive Control for Undamaged and Damaged Building Structures Under Seismic Load," *Computer-Aided Civil and Infrastructure Engineering,* vol. 27, pp. 48-64, 2012.
[60] H. Kim and H. Adeli, "Hybrid control of irregular steel highrise building structures under seismic excitations," *International Journal for Numerical Methods in Engineering,* vol. 63, pp. 1757-1774, 2005.
[61] H. Kim and H. Adeli, "Hybrid Control of Smart Structures Using a Novel Wavelet-Based Algorithm," *Computer-Aided Civil and Infrastructure Engineering,* vol. 20, pp. 7-22, 2005.
[62] P. Bhasker Rao and R. S. Jangid, "Performance of sliding systems under near-fault motions," *Nuclear Engineering and Design,* vol. 203, pp. 259-272, 1/2/ 2001.
[63] W.-I. Liao, C.-H. Loh, and B.-H. Lee, "Comparison of dynamic response of isolated and non-isolated continuous girder bridges subjected to near-fault ground motions," *Engineering Structures,* vol. 26, pp. 2173-2183, 12// 2004.
[64] J. Shen, M.-H. Tsai, K.-C. Chang, and G. C. Lee, "Performance of a Seismically Isolated Bridge under Near-Fault Earthquake Ground Motions," *Journal of Structural Engineering,* vol. 130, pp. 861-868, 2004.
[65] M. H. Jónsson, B. Bessason, and E. Haflidason, "Earthquake response of a base-isolated bridge subjected to strong near-fault ground motion," *Soil Dynamics and Earthquake Engineering,* vol. 30, pp. 447-455, 6// 2010.
[66] L.-Y. Lu, S.-Y. Chu, S.-W. Yeh, and C.-H. Peng, "Modeling and experimental verification of a variable-stiffness isolation system using a leverage mechanism," *Journal of Vibration and Control,* vol. 17, pp. 1869-1885, 2011.
[67] R. DesRoches and B. Smith, "Shape memory alloys in seismic resistant design and retrofit: a critical review of their potential and limitations," *Journal of Earthquake Engineering,* vol. 8, pp. 415-429, 2004.

[68] K. Otsuka and C. Wayman, "Mechanism of shape memory effect and superelasticity," *Shape memory materials,* pp. 27-48, 1998.
[69] M. Dolce and D. Cardone, "Mechanical behaviour of shape memory alloys for seismic applications 2. Austenite NiTi wires subjected to tension," *International Journal of Mechanical Sciences,* vol. 43, pp. 2657-2677, 11// 2001.
[70] O. Ozbulut and S. Hurlebaus, "Neuro-fuzzy modeling of temperature-and strain-rate-dependent behavior of NiTi shape memory alloys for seismic applications," *Journal of Intelligent Material Systems and Structures,* vol. 21, pp. 837-849, 2010.
[71] O. E. Ozbulut and S. Hurlebaus, "Seismic assessment of bridge structures isolated by a shape memory alloy/rubber-based isolation system," *Smart Materials and Structures,* vol. 20, p. 015003, 2010.
[72] A. R. Shahin, P. H. Meckl, and J. D. Jones, "Modeling of SMA Tendons for Active Control of Structures," *Journal of Intelligent Material Systems and Structures,* vol. 8, pp. 51-70, 1997.
[73] M. Dolce, D. Cardone, and G. Palermo, "Seismic isolation of bridges using isolation systems based on flat sliding bearings," *Bulletin of Earthquake Engineering,* vol. 5, pp. 491-509, 2007.
[74] E. Matta, "Effectiveness of tuned mass dampers against ground motion pulses," *Journal of Structural Engineering,* vol. 139, pp. 188-198, 2012.
[75] J. L. Lin and K. C. Tsai, "Seismic analysis of two-way asymmetric building systems under bi-directional seismic ground motions," *Earthquake Engineering & Structural Dynamics,* vol. 37, pp. 305-328, 2008.
[76] J. S. Heo, S. K. Lee, E. Park, S. H. Lee, K. W. Min, H. Kim, *et al.*, "Performance test of a tuned liquid mass damper for reducing bidirectional responses of building structures," *The Structural Design of Tall and Special Buildings,* vol. 18, pp. 789-805, 2009.
[77] W. H. Wu, J. F. Wang, and C. C. Lin, "Systematic assessment of irregular building–soil interaction using efficient modal analysis," *Earthquake engineering & structural dynamics,* vol. 30, pp. 573-594, 2001.
[78] J. M. Angeles and L. Alvarez-Icaza, "3D identification of buildings seismically excited," *IFAC Proceedings Volumes,* vol. 38, pp. 327-332, 2005.
[79] V. Gattulli, M. Lepidi, and F. Potenza, "Seismic protection of frame structures via semi-active control: modeling and implementation issues," *Earthquake Engineering and Engineering Vibration,* vol. 8, pp. 627-645, 2009.
[80] F. Amini, N. K. Hazaveh, and A. A. Rad, "Wavelet PSO-Based LQR Algorithm for Optimal Structural Control Using Active Tuned Mass Dampers," *Computer-Aided Civil and Infrastructure Engineering,* vol. 28, pp. 542-557, 2013.
[81] F. Casciati, L. Faravelli, and T. Yao, "Fuzzy logic in active structural control," in *Fuzzy Information Processing Society Biannual Conference, 1994. Industrial Fuzzy Control and Intelligent Systems Conference, and the NASA Joint Technology Workshop on Neural Networks and Fuzzy Logic*, 1994, pp. 268-272.
[82] S. Nagarajaiah, "Fuzzy controller for structures with hybrid isolation system," in *Proc., First World Conf. Struct. Control, TA2*, 1994, pp. 67-76.
[83] H.-S. Kim and P. N. Roschke, "Fuzzy Control of Base-Isolation System Using Multi-Objective Genetic Algorithm," *Computer-Aided Civil and Infrastructure Engineering,* vol. 21, pp. 436-449, 2006.

[84] R. Guclu, "Sliding mode and PID control of a structural system against earthquake," *Mathematical and Computer Modelling,* vol. 44, pp. 210-217, 2006.
[85] Z. Li and S. Wang, "Robust optimal H∞ control for irregular buildings with AMD via LMI approach," *Nonlinear Analysis: Modelling and Control,* vol. 19, pp. 256-271, 2014.
[86] O. Yoshida, S. J. Dyke, L. M. Giacosa, and K. Z. Truman, "Experimental verification of torsional response control of asymmetric buildings using MR dampers," *Earthquake engineering & structural dynamics,* vol. 32, pp. 2085-2105, 2003.
[87] L. Hong-nan and H. Lin-sheng, "Optimal design of liquid dampers for torsionally coupled vibration of structures," in *Intelligent Control and Automation, 2004. WCICA 2004. Fifth World Congress on*, 2004, pp. 4534-4538.
[88] N. K. Chandiramani and G. B. Motra, "Lateral-torsional response control of MR damper connected buildings," in *ASME 2013 International Mechanical Engineering Congress and Exposition*, 2013, pp. V04BT04A056-V04BT04A056.
[89] R. Bouc, "Forced vibration of mechanical systems with hysteresis," in *Proceedings of the fourth conference on non-linear oscillation, Prague, Czechoslovakia*, 1967.
[90] Y.-K. Wen, "Method for random vibration of hysteretic systems," *Journal of the engineering mechanics division,* vol. 102, pp. 249-263, 1976.
[91] B. Spencer Jr, S. Dyke, M. Sain, and J. Carlson, "Phenomenological model for magnetorheological dampers," *Journal of engineering mechanics,* vol. 123, pp. 230-238, 1997.
[92] M. Zapateiro, H. R. Karimi, N. Luo, B. M. Phillips, and B. F. Spencer Jr, "Semiactive backstepping control for vibration reduction in a structure with magnetorheological damper subject to seismic motions," *Journal of Intelligent Material Systems and Structures,* vol. 20, pp. 2037-2053, 2009.
[93] A. K-Karamodin and H. H-Kazemi, "Semi-active control of structures using neuro-predictive algorithm for MR dampers," *Structural control & health monitoring,* vol. 17, p. 237, 2010.
[94] M. Azimi, A. Rasoulnia, Z. Lin, and H. Pan, "Improved semi-active control algorithm for hydraulic damper-based braced buildings," *Structural Control and Health Monitoring,* 2016.
[95] B. Basu and S. Nagarajaiah, "A wavelet-based time-varying adaptive LQR algorithm for structural control," *Engineering structures,* vol. 30, pp. 2470-2477, 2008.
[96] M. D. Symans and S. W. Kelly, "Fuzzy logic control of bridge structures using intelligent semi-active seismic isolation systems," *Earthquake Engineering & Structural Dynamics,* vol. 28, pp. 37-60, 1999.
[97] M. Ahmadizadeh, "On equivalent passive structural control systems for semi-active control using viscous fluid dampers," *Structural Control and Health Monitoring,* vol. 14, pp. 858-875, 2007.
[98] T. T. Soong, "Active structural control," *Longman Scientific and Technical,* 1990.
[99] A. K. Chopra, *Dynamics of Structures: Theory and Applications to Earthquake Engineering*: Prentice Hall, 2011.
[100] A. Moussad, A. Zosso, and R. Resta, "Tall buildings under multidirectional winds: response prediction and reduction," *Wind tunnels and experimental fluid dynamics research journal,* pp. 301-324, 2011.
[101] Karami K and Amini F, "Decreasing the damage in smart structures using integrated online DDA/ISMP and semi-active control" *Smart Mater. Struct.* 21 105017, 2012.

[102] K. Kazemi Bidokhti, H. Moharrami, and A. Fayezi, "Semi-active fuzzy control for seismic response reduction of building frames using SHD dampers," *Structural Control and Health Monitoring,* vol. 19, pp. 417-435, 2012.
[103] H. Temimi, M. Ben-Romdhane, S. El-Borgi, and Y.-J. Cha, "Time-Delay Effects on Controlled Seismically Excited Linear and Nonlinear Structures," *International Journal of Structural Stability and Dynamics,* vol. 16, p. 1550031, 2016.
[104] G.-P. Cai, J.-Z. Huang, and S. X. Yang, "An optimal control method for linear systems with time delay," *Computers & structures,* vol. 81, pp. 1539-1546, 2003.
[105] R. E. Kalman, "A new approach to linear filtering and prediction problems," *Journal of basic Engineering,* vol. 82, pp. 35-45, 1960.
[106] F. Naeim and J. M. Kelly, *Design of seismic isolated structures: from theory to practice*: John Wiley & Sons, 1999.
[107] T. Liu, T. Zordan, B. Briseghella, and Q. Zhang, "An improved equivalent linear model of seismic isolation system with bilinear behavior," *Engineering Structures,* vol. 61, pp. 113-126, 2014.
[108] F. Yi, S. J. Dyke, J. M. Caicedo, and J. D. Carlson, "Seismic response control using smart dampers," in *American Control Conference, 1999. Proceedings of the 1999*, 1999, pp. 1022-1026.
[109] S. Bharti, S. Dumne, and M. Shrimali, "Seismic response analysis of adjacent buildings connected with MR dampers," *Engineering Structures,* vol. 32, pp. 2122-2133, 2010.
[110] M. E. Uz and M. N. Hadi, "Optimal design of semi active control for adjacent buildings connected by MR damper based on integrated fuzzy logic and multi-objective genetic algorithm," *Engineering Structures,* vol. 69, pp. 135-148, 2014.
[111] M. Abe, J. Yoshida, and Y. Fujino, "Multiaxial behaviors of laminated rubber bearings and their modeling. I: experimental study," *Journal of Structural Engineering,* vol. 130, pp. 1119-1132, 2004.
[112] E. Choi, T.-h. Nam, and B.-S. Cho, "A new concept of isolation bearings for highway steel bridges using shape memory alloys," *Canadian Journal of Civil Engineering,* vol. 32, pp. 957-967, 2005.
[113] D. G. Reigles and M. D. Symans, "Supervisory fuzzy control of a base-isolated benchmark building utilizing a neuro-fuzzy model of controllable fluid viscous dampers," *Structural Control and Health Monitoring,* vol. 13, pp. 724-747, 2006.
[114] J. Kennedy, "Particle swarm optimization," in *Proc. IEEE Conf. Neural Networks IV, Piscataway, NJ*, 1995.
[115] E. Nazarimofrad and S. M. Zahrai, "Seismic control of irregular multistory buildings using active tendons considering soil–structure interaction effect," *Soil Dynamics and Earthquake Engineering,* vol. 89, pp. 100-115, 2016.
[116] C. B. Haselton, "Assessing seismic collapse safety of modern reinforced concrete moment frame buildings," Stanford University, 2006.
[117] Xu Y and Chen B, "Integrated vibration control and health monitoring of building structures using semi-active friction dampers: I. Methodology" *Eng. Struct.* 30 1789–801, 2008.
[118] He J, Huang Q and Xu Y-L., "Synthesis of vibration control and health monitoring of building structures under unknown excitation" *Smart Mater. Struct.* 23 105025, 2014.
[119] Daubechies, I. "The wavelet transform, time-frequency localization and signal analysis." *IEEE transactions on information theory,* 36(5), 961-1005, 1990.

[120] Kim, H., and Melhem, H. "Damage detection of structures by wavelet analysis." *Engineering Structures*, 26(3), 347–362, 2004.
[121] Simonovski, I. & Bolte, M., "Damping identification using a continuous wavelet transform: application to real data," *Journal of Sound and Vibration*, 262(2), 291-307, 2003.
[122] Sun, Z., and Chang, C. "Structural damage assessment based on wavelet packet transform." *Journal of structural engineering*, 128(10), 1354-1361, 2002.
[123] Lin, J., and Qu, L. "Feature extraction based on Morlet wavelet and its application for mechanical fault diagnosis." *Journal of Sound and Vibration*, 234(1), 135–148, 2000.
[124] J.-N. Juang and R. S. Pappa, "An eigensystem realization algorithm for modal parameter identification and model reduction," Journal of Guidance, vol. 8, pp. 620-627, 1985.
[125] B. Peeters, "System identification and damage detection in civil engeneering," PhD thesis, Department of Civil Engineering, Katholieke Universiteit Leuven, Belgium, 2000.
[126] J. M. Caicedo, "Practical guidelines for the natural excitation technique (NExT) and the eigensystem realization algorithm (ERA) for modal identification using ambient vibration," Experimental Techniques, vol. 35, pp. 52-58, 2011.
[127] J. M. Caicedo, S. J. Dyke, and E. A. Johnson, "Natural excitation technique and eigensystem realization algorithm for phase I of the IASC-ASCE benchmark problem: Simulated data," Journal of Engineering Mechanics, vol. 130, pp. 49-60, 2004.
[128] K. Xu and T. Igusa, "Dynamic characteristics of multiple substructures with closely spaced frequencies," Earthquake Engineering & Structural Dynamics, vol. 21, no. 12, pp. 1059–1070, 1992.
[129] R. S. Jangid and T. K. Datta, "Performance of multiple tuned mass dampers for torsionally coupled system," Earthquake Engineering and Structural Dynamics, vol. 26, no. 3, pp. 307–317, 1997.
[130] J.-L. Lin, K.-C. Tsai, and Y.-J. Yu, "Bi-directional coupled tuned mass dampers for the seismic response control of twoway asymmetric-plan buildings," Earthquake Engineering and Structural Dynamics, vol. 40, no. 6, pp. 675–690, 2011.
[131] H. X. He, E. Z. Han, and Y. W. Lv, "Coupled vibration control of tuned mass damper in both horizontal and torsional direction," Applied Mechanics and Materials, vol. 578-579, no. 2, pp. 1000– 1006, 2014.
[132] C.-C. Lin, C.-C. Chang, and J.-F. Wang, "Active control of irregular buildings considering soil–structure interaction effects," *Soil Dynamics and Earthquake Engineering*, vol. 30, pp. 98-109, 2010/03/01/ 2010.
[133] A. Farshidianfar and S. Soheili, "Ant colony optimization of tuned mass dampers for earthquake oscillations of high-rise structures including soil–structure interaction," *Soil Dynamics and Earthquake Engineering*, vol. 51, pp. 14-22, 2013/08/01/ 2013.